UNIVERSITY OF CALIFORNIA SAN DIEGO

Controllable Epitaxial Growth of Metal Halide Perovskites for Single-crystal Devices

A dissertation submitted in partial satisfaction of the
requirements for the degree Doctor of Philosophy

in

Chemical Engineering

by

Yimu Chen

Committee in charge:

Professor Sheng Xu, Chair
Professor Shadi A. Dayeh
Professor David P. Fenning
Professor Yu-Hwa Lo
Professor Jian Luo

2020

The dissertation of Yimu Chen is approved, and it is acceptable in quality and form for publication on microfilm and electronically:

_____

_____

_____

_____

_____
Chair

University of California San Diego

2020

TABLE OF CONTENTS

LIST OF FIGURES

LIST OF TABLES

ACKNOWLEDGMENTS

I would like to firstly express a deep sense of gratitude to my advisor Professor Sheng Xu for his suggestions and guidance, both academically and personally, throughout my five-year Ph. D. career. His passions in solving world-class scientific problems and his endeavor in pursuing high-standard research works always encourage me. The experiences and suggestions he selflessly shared also have a profound impact on me and shape me into who I am today. It is my great honor to work with Professor Xu.

I also appreciate Professor Yu-Hwa Lo, Professor David P. Fenning, Professor Jian Luo, Professor Shadi A. Dayeh, Professor Kesong Yang, Prof. Wei Xiong, Professor Kenji Nomura. Professor Michael Sailor, and Professor Lain-Jong Li for their selfless suggestions and kind help.

I would like to acknowledge my colleagues and collaborators: Miss. Jiawei Song, Mr. Ruiqi Zhang, Mr. Yuheng Li, Mr. Woojin Choi, Mr. Liying Chen, Miss. Xueying Li, Miss. Yanqi Luo, Mr. Qizhang Yan, Dr. Ming-Hui Chiu, Mr. Chonghe Wang, Dr. Zhenlong Huang, Dr. Lin Zhang, Mr. Muyang Lin, Miss. Baiyan Qi, Mr. Zhuorui Zhang, Dr. Yangzhi Zhu, Dr. Xiaoxiang Gao, and Dr. Hong Ding.

I would also like to sincerely acknowledge my dear friends: Mr. Yusheng Lei, Mr. Yue Gu, Mr. Hongjie Hu, Mr. Yang Li, Dr. Chunfeng Wang, Dr. Yugang Yu, Dr. Mengji Chen, Dr. Yihuai Hu, and Mr. Yang Lin, Dr. Xupeng Yan, Mr. Siyu Zhu, Dr. Yige Zhou, and Miss. Xiaojing Liu. I will also remember the time we had together and I wish all of you a bright future.

I would like to say thank you to my parents M. C. and T. H. for the endless support and care. I would also like to say thank you to my wife W. D., and my parent in law W. D. and X. L. for the unconditional trust and encouragement. No word can express my love and gratitude.

Chapter Two, in full, is a reprint of the material ‘Lei, Y., Chen, Y., Gu, Y., Wang, C., Huang, Z., Qian, H., Nie, J., Hollett, G., Choi, W., Yu, Y., Kim, N., Wang, C., Zhang, T., Hu, H., Zhang, Y., Li, X., Li, Y., Shi, W., Liu, Z., Sailor, M., Dong, L., Lo, Y., Luo, J., Xu, S. Controllable homoepitaxial growth of hydrid perovskites. *Advanced Materials* **30**, 1705992, (2018)’. The dissertation author was the primary investigator and co-first author of this paper.

Chapter Three, in part, is a reprint of the material ‘Chen, Y., Lei, Y., Li, Y., Yu, Y., Cai, J., Chiu, M., Rao, R., Gu, Y., Wang, C., Choi, W., Hu, H., Wang, C., Li, Y., Song, J., Zhang, J., Qi, B., Lin, M., Zhang, Z., Islam, A., Maruyama, B., Dayeh, S., Li, L., Yang, K., Lo, Y., Xu, S. Strain engineering and epitaxial stabilization of halide perovskites. *Nature* **577**, 209-215, (2020)’. The dissertation author was the primary investigator and first author of this paper.

Chapter Four, in part, is a reprint of the material ‘Chen, Y., Lei, Y., Li, Y., Yu, Y., Cai, J., Chiu, M., Rao, R., Gu, Y., Wang, C., Choi, W., Hu, H., Wang, C., Li, Y., Song, J., Zhang, J., Qi, B., Lin, M., Zhang, Z., Islam, A., Maruyama, B., Dayeh, S., Li, L., Yang, K., Lo, Y., Xu, S. Strain engineering and epitaxial stabilization of halide perovskites. *Nature* **577**, 209-215, (2020)’. The dissertation author was the primary investigator and first author of this paper.

VITA

2015 Bachelor of Science in Chemistry

Shandong University

2020 Doctor of Philosophy in Chemical Engineering

University of California San Diego

PUBLICATIONS

(* authors contributed equally to the work)

Chen, Y.*, Lei, Y.*, Li, Y., Yu, Y., Cai, J., Chiu, M., Rao, R., Gu, Y., Wang, C., Choi, W., Hu, H., Wang, C., Li, Y., Song, J., Zhang, J., Qi, B., Lin, M., Zhang, Z., Islam, A., Maruyama, B., Dayeh, S., Li, L., Yang, K., Lo, Y., Xu, S. Strain engineering and epitaxial stabilization of halide perovskites. *Nature* **577**, 209-215, (2020).

Lei, Y.*, Chen, Y.*, Zhang, R., Li, Y., Yan, Q., Lee, S., Yu, Y., Tsai, H., Choi, W., Wang, K., Luo, Y., Gu, Y., Zheng, X., Wang, C., Wang, C., Hu, H., Li, Y., Qi, B., Lin, M., Zhang, Z., Dayeh. S., Pharr, M., Fenning, D., Lo, Y., Luo, J., Yang, K., Yoo, J., Nie, W., Xu, S. A fabrication process for flexible single-crystal perovskite devices. *Nature* **583**, 790-795, (2020).

Lei, Y.*, Chen, Y.*, Gu, Y., Wang, C., Huang, Z., Qian, H., Nie, J., Hollett, G., Choi, W., Yu, Y., Kim, N., Wang, C., Zhang, T., Hu, H., Zhang, Y., Li, X., Li, Y., Shi, W., Liu, Z., Sailor, M. J., Dong, L., Lo, Y.-H., Luo, J., Xu, S. Controlled homoepitaxial growth of hybrid perovskites. *Advanced Materials* **30**, 1705992, (2018).

Huang, A., Chen, Y., Zhou, Y., Guo, W., Wu, X., & Ma, C. An Efficient One-Pot Synthesis of Benzo[4,5]imidazo[1,2-a]quinoxalines via Copper-Catalyzed Process. *Organic Letters* **15**(21), 5480, (2013).

Xu, Z., Yu, Y., Arya, S., Niaz, I. A., Chen, Y., Lei, Y., Miah, M., Zhou, J., Zhang, A., Yan, L., Xu, S., Nomura, K., Lo, Y. Frequency-and power-dependent photoresponse of a perovskite photodetector down to the single-photon level. *Nano Letters* **3**, 2144, (2020).

Hu, H., Zhu, X., Wang, C., Zhang, L., Li, X., Lee, S., Huang, Z., Chen, R., Chen, Z., Wang, C., Gu, Y., Chen, Y., Lei, Y., Zhang, T., Kim, N., Guo, Y., Teng, Y., Zhou, W., Li, Y., Nomoto, A., Sternini, S., Zhou, Q., Pharr, M., Scalea, F,. Xu, S. Stretchable ultrasonic transducer arrays for three-dimensional imaging on complex surfaces. *Science Advances* **4**(3), eaar3979, (2018).

Huang, Z., Hao, Y., Li, Y., Hu, H., Wang, C., Nomoto, A., Pan, T., Gu, Y., Chen, Y., Zhang, T., Li, W., Lei, Y., Kim, N., Wang, C., Zhang, L., Ward, J., Maralani, A., Li, X., Durstock, M., Pisano, A., Lin, Y., Xu, S. Three-dimensional integrated stretchable electronics. *Nature Electronics* **1**(8), 473, (2018).

Wang, C., Li, X., Hu, H., Zhang, L., Huang, Z., Lin, M., Zhang, Z., Yin, Z., Huang, B., Gong, H., Bhaskaran, S., Gu, Y., Makihata, M., Guo, Y., Lei, Y., Chen, Y., Wang, C., Li, Y., Zhang, T., Chen, Z., Pisano, A., Zhang, L., Zhou, Q., Xu, S. Monitoring of the central blood pressure waveform via a conformal ultrasonic device. *Nature Biomedical Engineering* **2**(9), 687, (2018).

ABSTRACT OF THE DISSERTATION

Controllable Epitaxial Growth of Metal Halide Perovskites for Single-crystal Devices

by

Yimu Chen

Doctor of Philosophy in Chemical Engineering

University of California San Diego, 2020

Professor Sheng Xu, Chair

As an emerging class of semiconductors, metal halide perovskites have demonstrated tremendous potential in various applications, including photovoltaic solar cells, light-emitting diodes, photodetection, and many other electronic devices. While most of these perovskite electronic devices have adopted polycrystalline perovskite thin films, problems of polycrystalline thin films like the high density of grain boundaries and defects, low stability can hinder the further

performance enhancement of perovskite electronic devices. Comparing with their polycrystalline counterpart, single-crystal perovskites provide opportunities in solving such problems. Not only can they provide enhanced crystalline quality and excellent material stability, but also the possibility to alter the electronic properties of perovskites by lattice-mismatch-induced strain. Yet the development of single-crystal perovskite electronic devices is still in its infancy due to the low controllability over the growth of single-crystal perovskite nano/micro-structures and the incompatibility with the conventional semiconductor fabrication protocol.

This research aims to develop a platform for growing high-quality single-crystal metal halide perovskite nano/micro-structures using controllable chemical homo/heteroepitaxial growth and fabricating high-performance single-crystal-perovskite-based electronic devices with the conventional semiconductor fabrication protocols. In Chapter One, the basic properties of metal halide perovskites and the current problems presented in the polycrystalline perovskite thin films will be introduced and discussed. In Chapter Two, controllable homoepitaxial growth of metal halide perovskite micro-arrays will be introduced. Our work presents the first controllable growth of large-area single-crystal perovskite microarrays with different sizes, morphologies, crystalline orientations, and patterned structures. In Chapter Three, controllable strain engineering of single-crystal metal halide perovskite thin films by heteroepitaxial-growth-induced lattice mismatch will be introduced. Our work presents the first controllable strain engineering in metal halide perovskite family. In Chapter Four, epitaxial stabilization induced by the chemically epitaxial strain growth will be introduced. Our strategy provides insights into structurally stabilizing the metastable metal halide perovskite family. Our understanding of the controllable epitaxial growth of metal halide perovskites paves the way for next-generation single-crystal metal halide perovskites electronic devices.

Chapter 1. General Information of Metal Halide Perovskites

1.1 Structural Properties of Metal Halide Perovskites

Metal halide perovskites have a general ABX_3 formula where A is a cation, B is a metal ion, and X is a halide ion[1]. Commonly used A-site cations are methylammonium (MA^+), formamidinium (FA^+), and cesium ion (Cs^+). Lead ions (Pb^{2+}) and tin ions (Sn^{2+}) are commonly used as B-site metal ions while chloride (Cl^-), bromide (Br^-), and iodide (I^-) are used as X-site halide ions. Depending on the effect radii of the A-site cations, B-site ions, and X-site ions, the crystal structure of metal halide perovskites can range from a highly symmetric cubic structure to a less-symmetric tetragonal or orthorhombic structure. In general, these pseudocubic structure halide perovskites consist of the corner-sharing [BX_6] octahedra and an A-site cation which occupies the 12-fold coordination site formed in the middle of eight [BX_6] octahedra[2], as shown in Figure 1. Tolerance factor is usually used to evaluate whether the pseudocubic perovskite structure can be maintained[3]:

$$t = \frac{r_A + r_X}{\sqrt{2}(r_B + r_X)} \quad (1)$$

where t is the tolerance factor, r_A is the effective radius of the A-site cation, r_B is the effective radius of the B site metal ion, and r_X is the effective radius of the X site halide ion. t should fall in the range of 0.75-1 to hold a stable pseudocubic perovskite structure.

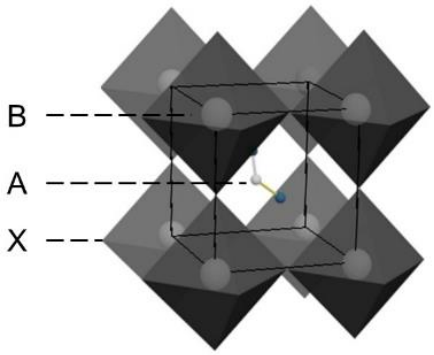

Figure 1. Schematic structure of metal halide perovskites.
Metal halide perovskites have a pseudocubic lattice structure and an ABX_3 formula.

1.2 Metal Halide Perovskites as a Class of Semiconductors

Metal halide perovskites exhibit excellent semiconducting properties. With different compositions, metal halide perovskites show a tunable direct bandgap between 1.2 eV to 3.1 eV, which covers the entire visible light spectrum. It has been reported that the valance band maximum (VBM) of metal halide perovskites mainly consists of heavy metal ion (e.g., Pb) *s* orbitals and halide ions (e.g., I) *p* orbitals[4]. Therefore, the substitution of chemical composition can effectively alter the coupling of the orbitals and, consequently, the electronic band structures and bandgap of perovskites, which enables a broad range of applications.

Meanwhile, metal halide perovskites show a high absorption coefficient up to 10^5 cm^{-1} over the spectra they cover[5], which is over one order of magnitude higher than that of conventional semiconductor Si[6]. This high absorption coefficient not only benefits the light-harvesting of the perovskites but also reduces the required thickness of the devices. Consequently, this can potentially reduce the charged carrier recombination and contribute to a higher open-circuit voltage in photovoltaics, according to the Shockley-Queisser model.

As a class of semiconductors, metal halide perovskites are also demonstrated to have tunable exciton binding energy (E_b) based on the compositions and dimensionalities. For the widely studied $MAPbI_3$, E_b is reported to be ~10 meV[7]. This value is much smaller than the thermal energy at room temperature (~26 meV), indicating that the excitons (bounded electron-hole pairs) can easily overcome the Coulomb interaction by the thermal fluctuation and become free charged carriers[8]. Free charged carriers can be separately collected upon excitation, and this unique property is suitable for photovoltaic and photodetection applications. In contrast, changing the composition by substituting the halide ions and reducing the dimensions of metal halide perovskites can effectively increase the E_b to several hundreds of micron electric volt, which enables the enhanced radiative recombination of the charged carriers. In this case, halide perovskites are also exhibiting potential for light-emitting applications. In addition, metal halide perovskites are also demonstrated to have superior charge carrier dynamics. High charged carrier mobility and long charged carrier life are reported[9], which contribute to the long charged carrier diffusion length[2] and their success in next-generation electronic devices.

Besides, metal halide perovskites also show solution processability[10]. High-quality perovskite single crystals can be easily obtained by several crystallization methods from perovskite solutions, and polycrystalline thin films can be deposited by a variety of methods including spin coating, blade coating, stamping, spray coating, and vacuum deposition[11]. This feasibility of solution processability exhibits potential for large-area low-cost deposition.

1.3 Current Applications of Metal Halide Perovskites

Due to the superior optical and electrical properties, as mentioned above, metal halide perovskites have demonstrated potentials for photovoltaic and optoelectronic applications, including solar cells[12-14], light-emitting diodes (LEDs)[15-17], photodetectors[18-20], field-effect transistors (FET)[21-23], radiation detection/imaging[24-26], and many others[27]. Among these broad applications range, solar cells are most widely studied due to the high power conversion efficiency, which is comparable to those highly crystalline silicon solar cells. In the past decade, the power conversion efficiency of the state-of-art small-area (<1 cm^2) perovskite solar cells has rapidly increased from 3.8% to a certificated 25.2%[11]. In general, perovskite solar cells adopt a formal 'n-i-p' structure where the intrinsic perovskite absorber layer is sandwiched by an n-type electron transporting layer (usually TiO_2 and SnO_2) and a p-type hole transporting layer[28]. Besides, an inverted 'p-i-n' structure with a p-type hole transporting layer (usually organics) and an n-type electron transporting layer is also reported to reduce hysteresis[28]. A large-area (>100 cm^2) solar module is required for commercialization[11]. The module, however, has a much lower power conversion efficiency compared with the small-area solar cell due to the decrease of short-circuit current[11]. As for the deposition method, spin coating is widely used in fabricating small-area devices. When scaling up the area, deposition methods with a better large-area uniformity such as blade coating, spraying, slot-die coating, stamping, and vacuum deposition are preferred[11]. For large-area perovskite modules, currently, a certified 17.25% power conversion efficiency has been achieved with a 17.28 cm^2 illumination area[29], and a 16.1% efficiency is also achieved by an 802 cm^2 device[29], showing great potential for highly efficient photovoltaic applications.

Due to the extraordinary optoelectronic properties, tunable emission wavelength, and narrow emission linewidth, metal halide perovskites have also been successfully applied in light-

emitting applications. Photoluminescent quantum yields of perovskites have been reported to be reaching 100%, demonstrating the minimized non-radiative recombination and energy losses in designed perovskites materials[30,31]. Perovskites also show an extremely wide color gamut (~140%) due to the narrow emission bandwidth[32], showing the potential for next-generation display technology[33]. Similar to that of perovskite solar cells, the device structure of perovskite LEDs can be classified into formal and inverted structures with the perovskite emitter sandwiched by two different carrier transporting layers[33]. Besides the conventional three-dimensional (3D) perovskites, two-dimensional (2D) perovskites and perovskite quantum dots/nanocrystals are also widely studied due to the high E_b induced by the dimensionality reduction quantum effect[34]. Recently, both green and red light perovskite LEDs have shown external quantum efficiency over 20%[16,35-37], while the performance of the blue light perovskite LEDs (external quantum efficiency <11%[17]) still lags behind due to the absence of suitable hole transporting layer to match the deep VBM[38].

Metal halide perovskites have also been widely used as photodetectors. There are two main types of device structure for perovskite photodetectors, which are photodiode type and photoconductor type[5]. Photodiode-type perovskite photodetector has a structure similar to that of solar cells and LEDs and is usually reversely biased to reduce the dark current density[5]. As a result, this type of photodetector exhibits a high detectivity and a high response speed[5]. Photoconductor-type perovskite photodetector has a much simpler structure and a larger photoresponse due to the amplification effect. Recently, a phototransistor-type perovskite photodetector is demonstrated to have both a large photoresponse and a high response speed[39]. Unlike perovskite solar cells and LEDs where the efficiency is a most critical standard, perovskite photodetectors can be assessed by multiple parameters depending on the applications. High detectivity and large linear dynamic

range are favorable for weak intensity detection. Fast response speed can be utilized in high-speed optical communications. Narrowband detection is favorable in spectrally selective detection, and high responsivity is also essential to all photodetectors.

The above applications represent most of the electronic devices based on metal halide perovskites. In recent years, several reports also prove the potential of perovskites for other applications. Recently, metal halide perovskites have shown potential in ionizing radiation detection/imaging due to their strong stopping power, large mu-tau product, large bulk resistivity, radiation hardness, and defect tolerance[40-45]. Besides, perovskite-based ionizing radiation detectors have shown comparable performance to those commercial detectors based on Si, HgI_2, and $Cd_{1-x}Zn_xTe$, α-Se, and many others, showing the possibility to replace current ionizing radiation detectors. Besides, perovskites have also been demonstrated as field-effect transistors due to the excellent carrier dynamics[21,23,46].

1.4 Limitation in Current Metal Halide Perovskite Devices

Although metal halide perovskites have been successfully applied to multiple fields and have been seen as a class of promising next-generation semiconductors, current metal halide perovskite electronic devices are heavily relying on the polycrystalline thin films due to the simplicity of deposition[47]. By using spin coating, blade coating, vacuum deposition, and other deposition methods, polycrystalline perovskite thin films can be easily deposited onto arbitrary substrates[11]. Despite the deposition simplicity and the successful application in electronic devices, polycrystalline perovskite thin films face many challenges, which impede the further development and commercialization of perovskite-based electronic devices.

From the structural aspect, a high density of structural defects such as point defects (e.g., vacancies), 2D defects (e.g., grain boundaries), and 3D defects (e.g., residue clusters) are presented in the polycrystalline thin films[48]. Figure 2 shows a typical Scanning Electron Microscope (SEM) image of the polycrystalline perovskite thin film, where the grain boundaries and residue clusters can be evident. These defects lead to the formation of sub-bandgap electronic traps in perovskites and can serve as the non-radiative recombination center for charged carriers[48]. Trap density characterizations show that the trap density is on the scale between 10^{15}-10^{17} cm^{-3} for polycrystalline perovskite thin films[6]. For devices like solar cells, LEDs, photodetectors, and radiation detectors whose performances are highly related to the carrier diffusion length, such high trap density can lead to a severe charged carrier non-radiative recombination and device performance deterioration. Besides, grain boundaries also scatter the charged carriers and incident photons to harm the carrier mobility and absorption coefficient, respectively[49,50]. This also potentially leads to the impairment of further boosting the perovskite electronic device performance.

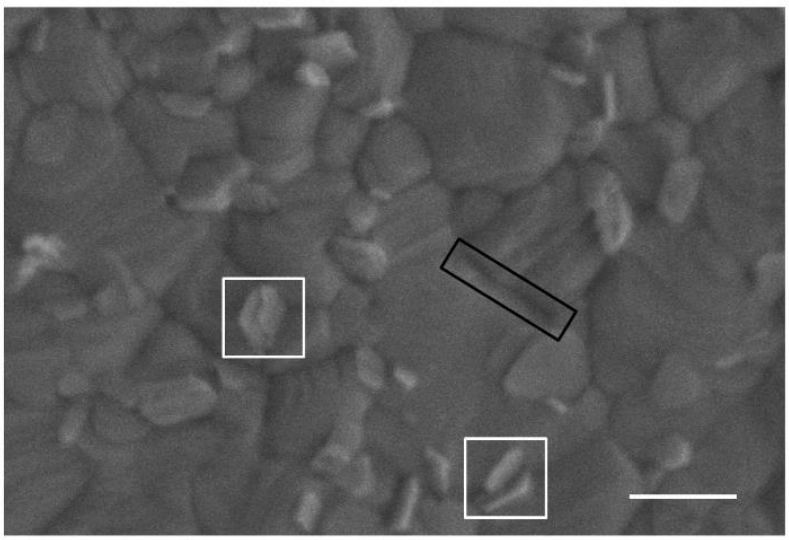

Figure 2. A typical SEM image of the polycrystalline perovskite thin film.
A high density of grain boundaries (black box) and residue clusters (white box, PbI_2) are represented in the polycrystalline perovskite thin film. Scale bar: 500 nm.

From the stability aspect, the grain boundaries also serve as the channel for oxygen and moisture penetrating into the perovskite grains and lead to the accelerated degradation of polycrystalline thin films under ambient conditions[51]. It is also found that a high level of local heterogeneity exists in polycrystalline perovskites thin films[52], especially at the grain boundaries, and results in the accelerated decomposition of perovskites under high temperature by organic cation volatilization[53]. Therefore, polycrystalline perovskites also suffer from material stability and thermal stability issues.

Another challenge presents in the polycrystalline perovskite thin films is the low activation energy for ion migration. Under biased operation conditions, ion migration takes place through the point defects and grain boundaries in polycrystalline perovskite thin films[54]. The accumulation of ions at the perovskite/electrode interfaces affects the performance by screening effect and the reliability of the devices by current-voltage (*I*-*V*) hysteresis[55].

Chapter 2. Single-crystal Metal Halide Perovskite Devices by Controllable Homoepitaxial Growth

2.1 Motivation for Studying Single-crystal Metal Halide Perovskite Devices

Compared with the polycrystalline metal halide perovskites, single-crystal perovskites mainly exhibit advantages in three different general categories: outstanding crystalline quality, enhanced material stability, and the possibility to achieve controllable strain engineering for performance enhancement.

Different from polycrystalline perovskites that consist of multiple grains and grain boundaries, single-crystal perovskites are sequentially formed by the network of oriented lattices, which largely reduce the formation of defects and annihilate the existence of grain boundaries. Published researches show that the trap density of single-crystal perovskite is around five to seven orders of magnitude lower than that of polycrystalline perovskite[56]. The reduction of structural defects and electronic traps minimizes the non-radiative recombination of the charged carriers. This is proven by the much-elongated carrier lifetime and higher photoluminescence quantum yield in single-crystal perovskites[57]. Besides, the grain boundary annihilation in single-crystal perovskites eradicates the scattering of the charged carriers when passing through the grain boundaries, contributing to the excellent carrier dynamics in single-crystal perovskites[49,50]. Reports show that single-crystal perovskites have enhanced carrier mobilities and diffusion lengths compared with polycrystalline perovskites[49]. In terms of the optical property enhancement, the annihilation of grain boundaries also reduces the scattering of photons for more efficient photon

absorption and reabsorption in single-crystal perovskites, contributing to efficient photon collection[58].

Due to the ordered arrangement of lattices, single-crystal perovskites eliminate the grain boundary and local heterogeneity[59]. Without the channel for moisture and oxygen penetration, single-crystal perovskites exhibit long-term stability under the ambient condition without severely degradation[51]. Also, it has been shown that the single-crystal perovskite exhibits enhanced thermal stability than that of polycrystalline perovskite by Thermogravimetric analysis[60,61]. Besides the enhanced stability, single-crystal perovskites also show reduced ion migration due to the point defect reduction and grain boundary annihilation due to the enhanced crystalline quality[62].

It is also worth to mention that single-crystal perovskites exhibit the potential to achieve controllable strain engineering by inducing lattice mismatch during epitaxial growth[63,64]. This is due to the fact that the epitaxial lattices will adopt a conformal lattice parameter with that of the substrate lattices to form a coherent structure at the growth interface. The lattice mismatch between the epitaxial layer and substrate can, therefore, be used as an effective tool to deform and create strain to the epitaxial lattices. With the strain, the electronic band structure of the epitaxial layer can be modified to enhance the properties or even create new functionalities. In polycrystalline perovskites, however, it is impossible to generate controllable strain due to the physical attachment to the substrate.

In summary, single-crystal perovskites provide insight into perovskite electronic devices with high quality, long-term operation stability, and enhanced performance.

2.2 Current Studies of Single-crystal Metal Halide Perovskite Devices

Owing to the superior properties and long-term stability shown by the single-crystal metal halide perovskites, researchers have been trying to build electronic devices based on the single-crystal metal halide perovskites. Fabricating planar devices directly on the bulk crystals and single-crystal perovskite wafers have been widely adopted and studied due to the simplicity of this method. Planar solar cell with the electrodes directly deposited on the bulk metal halide perovskite crystal surface shows a power conversion efficiency of 1.88%, which is 44 times higher than that of a polycrystalline thin film with the sample structure[65]. By proper surface defect passivation and the addition of planar carrier transporting layers, planar perovskite solar cells based on perovskite bulk single crystals and perovskite single crystal wafer can achieve power conversion efficiency exceeding 11% and 5.9%, respectively. Other than solar cells, perovskite bulk crystals with a simple planar structure are also widely used in photodetection applications. Due to the enhanced crystalline quality and superior carrier dynamics, photodetectors with enhanced responsivity and low detection limits are reported[66-68]. In addition to the photovoltaic and optoelectronic devices, perovskite bulk crystals can also be used as radiation detector[24-26,43,44]. These electronic devices based on perovskite bulk crystals and wafers, however, are not suitable for the small volume integration because of the bulky size. Meanwhile, the planar device layout is not suitable for the integration of carrier transporting/blocking layers.

Besides the planar electronic devices based on bulk metal halide perovskites crystals and wafers, devices fabricated based on the perovskite thin film are also frequently attempted. To be compatible with the advanced perovskite optoelectronic techniques, obtaining a high-quality single-crystal metal halide perovskite thin film with controllable thickness and pattern is critical.

Chemical vapor deposition (CVD) is commonly used in growing single-crystal perovskites. Researchers achieved the epitaxial growth of metal halide perovskites within a limited range of substrates. In most of these epitaxial halide perovskites, however, the interaction between the perovskites and the substrates are relatively weak (van der Waals epitaxy)[64,69,70]. Therefore, the epitaxial halide perovskites crystallize into flakes instead of a uniform thin film. Several reported works demonstrated the ion epitaxy of halide perovskites with uniform thin films[71,72]. However, the limited selection of the substrates constrains the diversity of the epitaxial perovskite films.

Besides CVD growth, space confinement growth of single-crystal metal halide perovskite thin film is another emerging technique. By confining the growth geometry with two clamping spacers, the single-crystal thin film can crystallize from the solution trapped in between the spacers[58,73,74]. The selection of the single-crystal halide perovskite can be controlled by choosing solutions with different compositions[75,76]. However, the crystallization of the single-crystal thin films becomes uncontrollable without preferential growth site, and the thickness of the single-crystal thin films is also uncontrollable.

Although single-crystal perovskites have shown enhanced resistance to moisture in the air (ambient condition) due to the annihilation of grain boundaries as introduced previously, the direct contact with aqueous solutions is still fatal to perovskites since the organic cation can be dissolved into the water. Therefore, the direct fabrication of perovskite single crystals with conventional nano/micro-fabrication techniques like photolithography is impossible.

Other single-crystal halide perovskites thin film growth techniques are also reported. A solution-based printing method for single-crystal halide perovskite thin film on a Si wafer is

reported[77]. However, this method shows a limited selection of the substrates due to the high selectivity. Single-crystal halide perovskite thin film growth methods based on the surface tension at the solution/air interface are also reported[78,79]. However, the growth of these thin films is less controllable because of the growth condition. Therefore, a single-crystal metal halide perovskite growth technique with controllability of the growth site, morphology, and thickness is needed.

2.3 Homoepitaxial Growth of Single-crystal $MAPbBr_3$ and Morphology Control

Compared with the weak van der Waals epitaxy using conventional single-crystal substrates, homoepitaxy provides insight into forming stable chemical bonds at the interface for controllable and uniform epitaxial growth[80]. In this case, a perovskite single crystal will be used as the substrate, and the same perovskite will be epitaxially grown on the substrate. Meanwhile, a patterned mask on the substrate fabricated by the conventional photolithography is required to grow patterned structure. In this study, $MAPbBr_3$ is used as an illustration. Single-crystal $MAPbBr_3$ substrates are grown by evaporating the solvent of the $MAPbBr_3$ solution. To prepare the $MAPbBr_3$ solution, CH_3NH_3Br (MABr, 0.748 g) is dissolved in anhydrous DMF (4 mL, 99.8%, Aldrich) in a 20 ml glass vial. Then, $PbBr_2$ (2.452 g, 98%, Acros) is added into the glass vial with stirring to get nearly saturated clear $MAPbBr_3$ solution. The solution is filtered, and the single-crystal $MAPbBr_3$ substrates can be obtained by evaporating the solvent under ambient conditions. MABr is synthesized by a previously reported method[81]. Methylammonium bromine (MABr) was synthesized as the precursor for the substrate growth. First, 20 ml methylamine (40% in methanol, Tokyo Chemical Industry Co.) and 21.2 mL hydrobromic acid (48 wt% in water, Sigma Aldrich) are mixed in an ice bath, and the temperature is maintained for the reaction to continue for 2 hours. The mixture was heated up to 80℃ to evaporate the solvent. The precipitate was dissolved in

anhydrous ethanol (Sigma Aldrich) at 80℃ and cooled down for recrystallization. The crystals were then centrifuged with diethyl ether and dried at 80℃ for overnight.

To ensure that our $MAPbBr_3$ substrate can survive the aqueous solutions used in the photolithography process, we deposit a dense and water-resisting polymer layer (Parylene-C, 50-500 nm) onto the surface of perovskite substrate so that the perovskite substrate can be isolated from the aqueous environment during the photolithography process. Meanwhile, we also sequentially deposit a layer of Cr and Au as the adhesion layer and electrode, respectively. In this case, the mask consists of Parylene-C/Cr/Au also serve as moisture protection and electrode. With the help of photolithography and etching, we can pattern the mask and expose the underlying $MAPbBr_3$ substrate surface for epitaxial growth sites. Figure 3a shows the schematic illustration of this fabrication process, and Figure 3b shows the optical images of each process. Parylene-C, Cr, and Au are sequentially deposited onto the $MAPbBr_3$ substrate. Photoresist AZ-1512 is deposited, and a photolithography patterning process is done. Sequential etching removes the Au/Cr/Parylenen layer in the exposed pattern. After the patterning and etching process, the $MAPbBr_3$ substrate with a patterned mask can be obtained. The patterns partially expose the $MAPbBr_3$ substrate surface so that the exposed surface can serve as the preferential growth site for epitaxial growth. We note that, for the first time, the direction fabrication on perovskite can be achieved with our method[56].

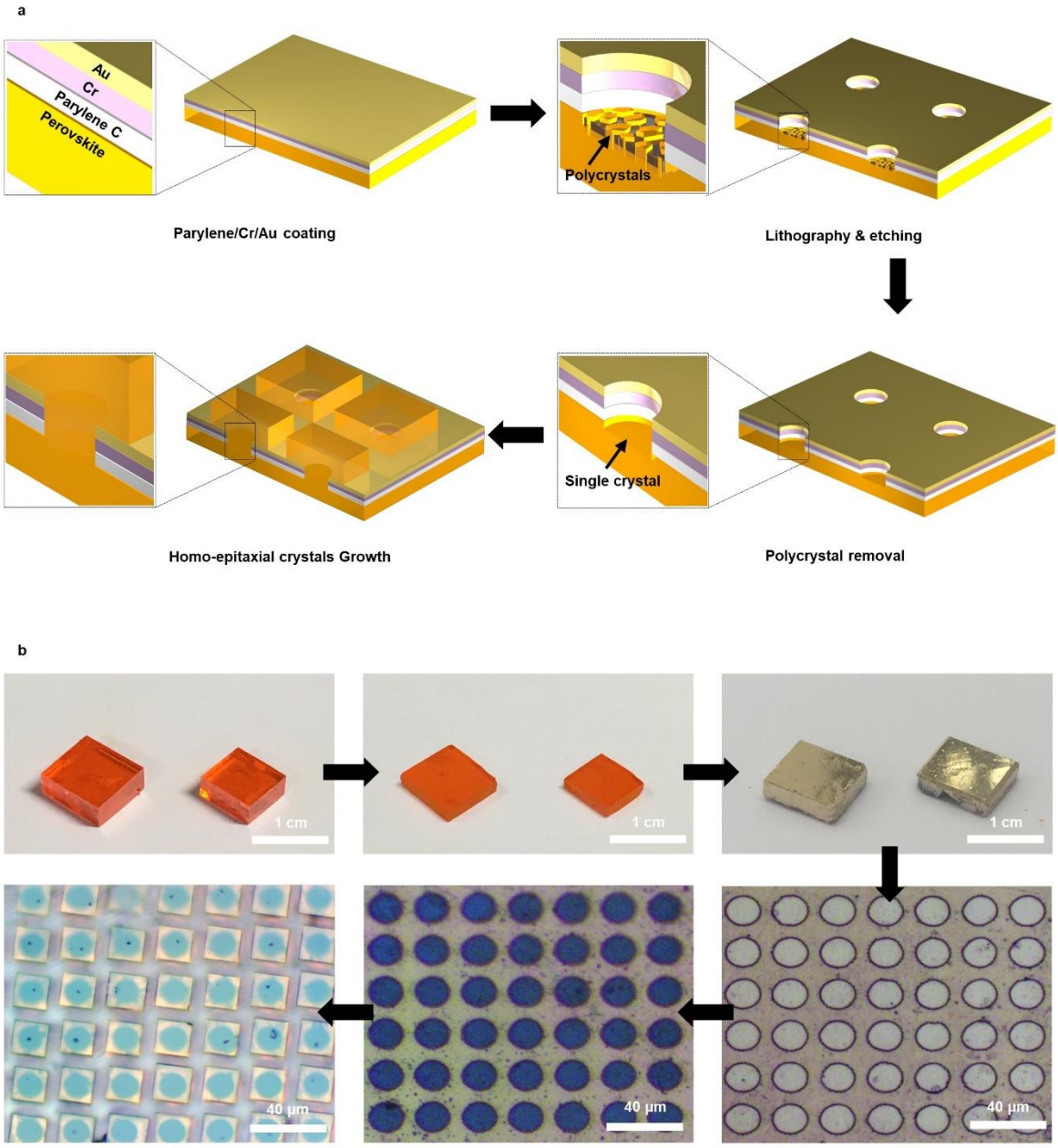

Figure 3. Illustration of the fabrication process.
a, Schematic fabrication process. Parylene-C/Cr/Au are sequentially deposited on $MAPbBr_3$ substrate. After the etching process, the substrate surface is exposed in the pattern for sequential epitaxial growth. **b,** Optical images of the fabrication and growth process. The zoom-in images of the substrate after photolithography, etching, and epitaxial growth are shown in the lower right, middle, and left image, respectively

The patterned $MAPbBr_3$ substrate is then placed into a room-temperature $MAPbBr_3$ solution, and the solution is heated to different temperatures for epitaxial growth with inverse temperature crystallization method. Starting from the exposed substrate surface, the epitaxial

$MAPbBr_3$ gradually fills the patterns and grows out to form micro-arrays (Figure 4). The as-grown micro-arrays are in direct contact with the mask, which also serves as the bottom electrode for electronic device applications.

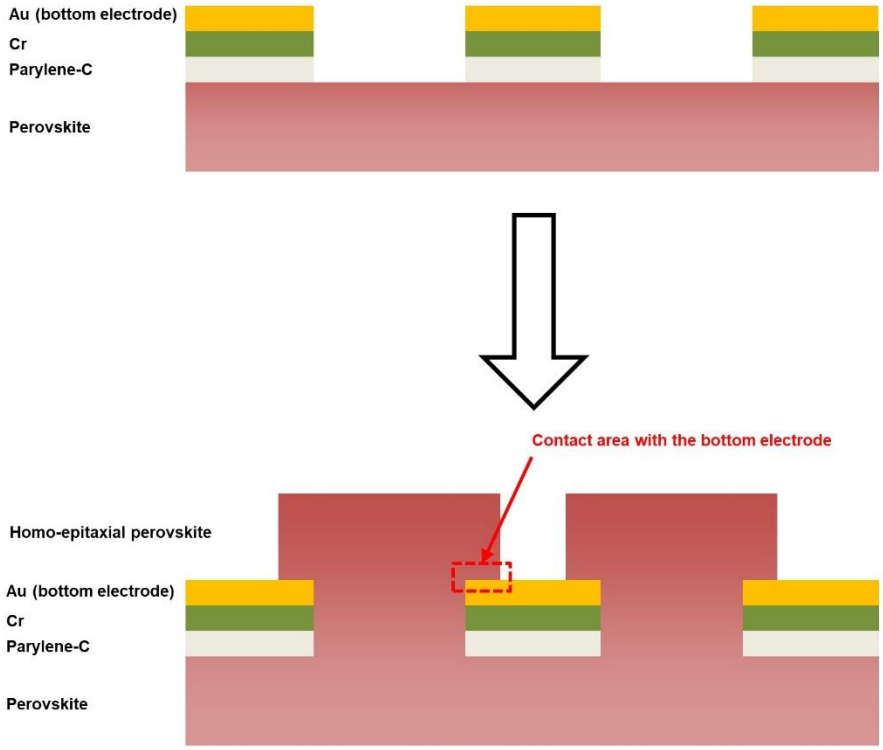

Figure 4. Schematic cross-section for the growth process of the epitaxial $MAPbBr_3$ microarrays.
The epitaxial $MAPbBr_3$ grows from the substrate surface in the exposed pattern, fills the entire pattern, and grows out of the pattern. Afterward, the epitaxial $MAPbBr_3$ will grow both horizontally and vertically, forming contact with the surface of the bottom electrode.

Figure 5a shows the large-area top-view SEM image of the as-grown single-crystal $MAPbBr_3$ microcubes arrays. Due to the epitaxial relationship, the $MAPbBr_3$ microcubes are highly ordered with perfect alignment. Meanwhile, strong chemical bonds are formed at the homoepitaxial interface between the substrate and the epitaxy, contributing to the large-area growth with excellent uniformity and coverage. Figure 5b, 5c, and 5d show the close view of the $MAPbBr_3$ microcubes, microrods, and microplates, respectively. We note that the morphology of the $MAPbBr_3$ microarrays is controlled by the circle-shape pattern size and growth temperature:

high temperature (>80 °C) with small pattern (<5 μm) will result in the rod-like structure; low temperature (<60 °C) with large pattern (>10 μm) will lead to plate-like structure; low temperature (<60°C) and medium-sized pattern (5–10 μm) could generate the cubic-like structure. These crystals are uniform in size, indicating a high degree of controllability. Besides, we also achieve the growth orientation control by exposing different crystal planes of the substrate. Figure 5e and 5f show the SEM images of the <101>- and <111>-oriented $MAPbBr_3$ microarray, respectively. These orientation control of the $MAPbBr_3$ microarray provides the platform for investigating the merit of different crystal planes in carrier dynamics studies[82].

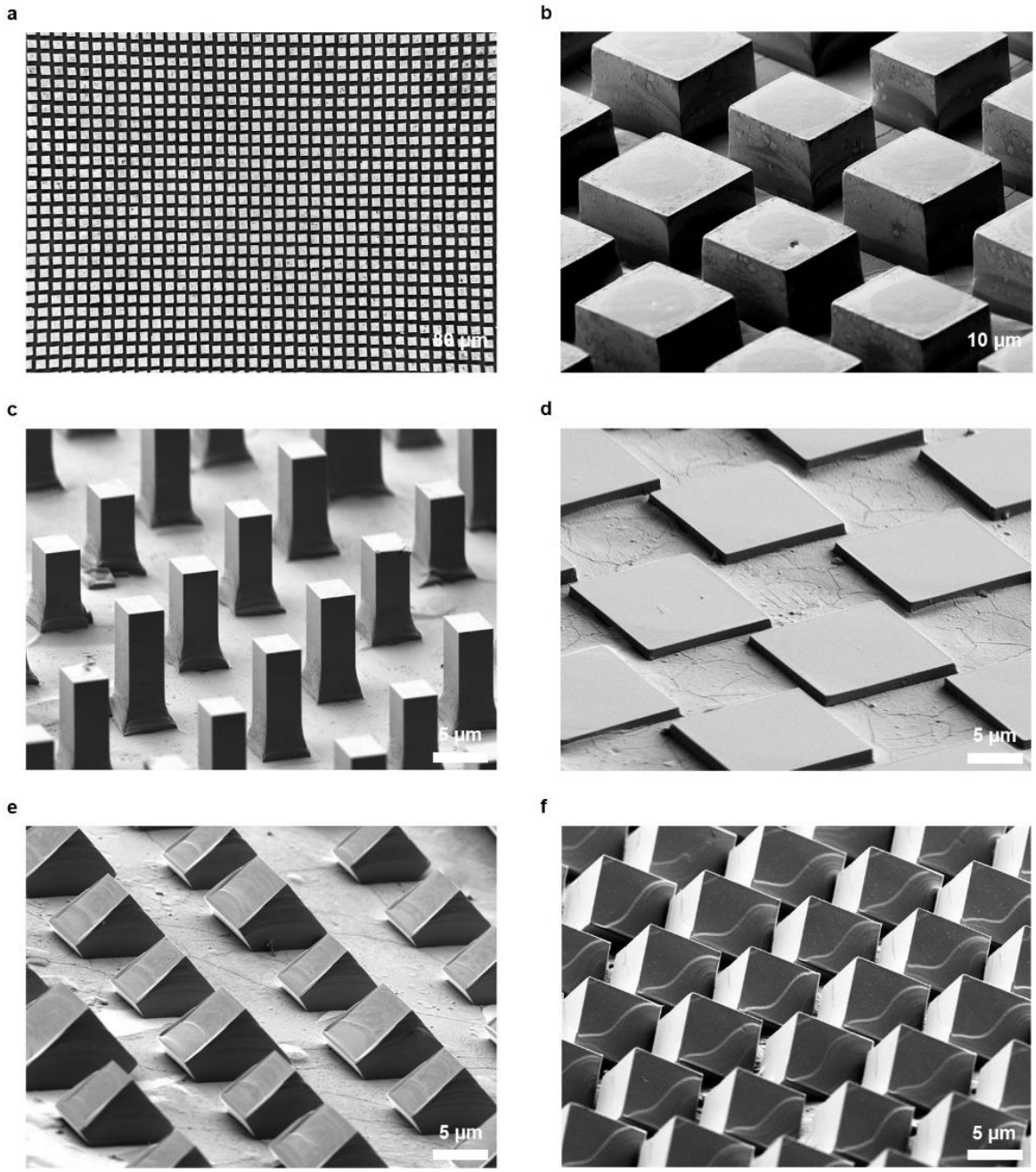

Figure 5. Controllable homoepitaxial growth of the $MAPbBr_3$ microarrays.
a, Large-area SEM image of the <100>-oriented $MAPbBr_3$ microcubes arrays. **b,** SEM image of the <100>-oriented $MAPbBr_3$ microcube arrays. **c,** SEM image of the <100>-oriented $MAPbBr_3$ microrod arrays. **d,** SEM image of the <100>-oriented $MAPbBr_3$ microplate arrays. **e,** SEM image of the <101>-oriented $MAPbBr_3$ microarrays. **f,** SEM image of the <101>-oriented $MAPbBr_3$ microarrays. Our results show that the uniformity of the epitaxial $MAPbBr_3$ microarrays, indicating the controllability over morphologies and orientations.

Energy Dispersive X-ray (EDX) spectroscopy is also carried on the SEM to confirm the composition of the epitaxial $MAPbBr_3$ microarrays. Figure 6a shows the EDX element mapping and Figure 6b shows the EDX spectrum of a microcube. Both results confirm the element composition of the epitaxial $MAPbBr_3$ microarrays.

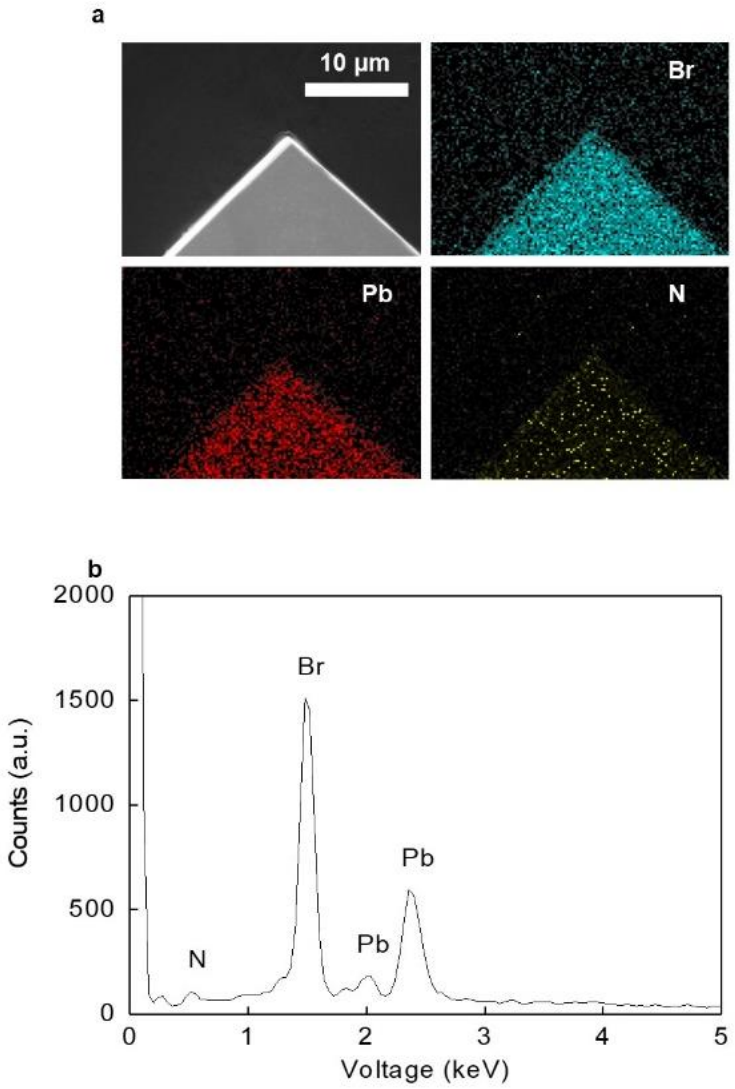

Figure 6. EDX study of the epitaxial $MAPbBr_3$ microcube.
a, EDX element mapping of an epitaxial $MAPbBr_3$ microcube. **b,** EDX spectrum shows that Pb, Br, and N are presented.

2.4 Structural and Optical Characterizations of Homoepitaxial $MAPbBr_3$

To study the crystallographic relationship between the epitaxial $MAPbBr_3$ microarrays and $MAPbBr_3$ substrate, XRD is carried out. Figure 7a shows the XRD θ-2θ scan of the $MAPbBr_3$ powder and the ω-2θ scan of the (001) epitaxial $MAPbBr_3$ microarrays. Results show that the epitaxial $MAPbBr_3$ microarrays gain a preferential out-of-plane crystallographic orientation due to the homoepitaxial relationship with the substrate. Diffraction peak from any other crystal plane is absent, indicating the uniformity of the as-grown $MAPbBr_3$ microarrays. 2D-XRD results of the virgin substrate and the as-grown epitaxial $MAPbBr_3$ microarrays are shown in Figure 7b. The 2D-XRD patterns of both the substrate and the epitaxy $MAPbBr_3$ microarray exhibit only three dominant diffraction peaks, attributed to the (100), (200), and (300) reflections of the cubic structure $MAPbBr_3$, demonstrating their high degree of crystallinity. The two sets of peaks from the substrate and epitaxial crystals show perfect alignment, indicating the epitaxially crystallographic relationship between the substrate and $MAPbBr_3$ microarrays. We note that the epitaxial crystals show brighter diffraction rings because the intensity is the sum of the diffraction from each individual microcrystal.

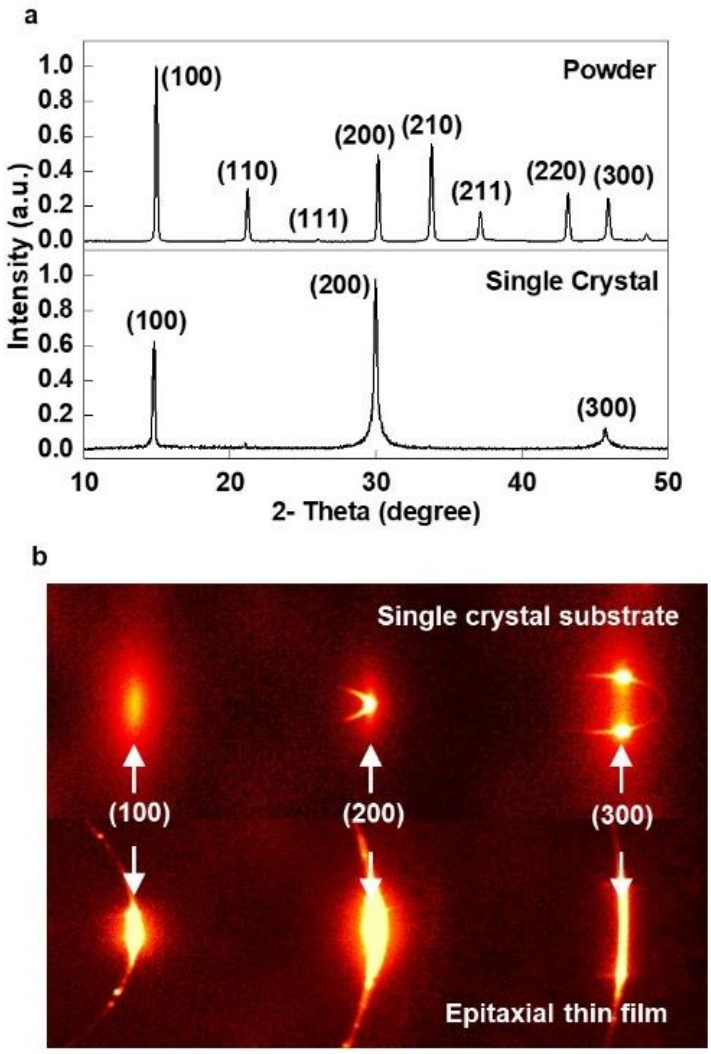

Figure 7. Crystallographic study of the epitaxial $MAPbBr_3$ microarrays.
a, XRD Comparison between the $MAPbBr_3$ powder and epitaxial $MAPbBr_3$ microarrays. Results show that the epitaxial $MAPbBr_3$ microarrays have gained a preferential out-of-plane orientation. b, 2D-XRD of the $MAPbBr_3$ substrate and the as-grown epitaxial $MAPbBr_3$ microarrays. Results indicate the epitaxially crystallographic relationship between the substrate and $MAPbBr_3$ microarrays.

2.5 Crystalline Quality and Carrier Dynamics Characterizations of the Homoepitaxial $MAPbBr_3$

The successful growth of the homoepitaxial $MAPbBr_3$ microarrays with controllable morphology and orientations provide a platform for the single-crystal perovskite devices[56]. To

demonstrate that the epitaxial $MAPbBr_3$ microarrays also exhibit enhance quality and property for high-performance devices, the studies of the crystalline quality and the carrier dynamics are carried out. Since the structural defects are directly related to the sub-bandgap electronic traps, we performed trap density characterization to study the crystalline quality of the epitaxial $MAPbBr_3$ microarrays with the space-charge-limit-current (SCLC) measurement. By filling the electronic traps with the injected charged carriers, SCLC measurement can reveal sub-bandgap trap density through the study of the *I-V* characteristic curves. A thin layer of Au is deposited onto the epitaxial $MAPbBr_3$ microarray as the top electrode. We note that the SCLC measurements are carried out by a Keithley 2400 source meter and a customized probe station in a dark environment.

In SCLC measurement, the log-log *I-V* characteristic curves show different regions of behavior. At low voltages, the *I-V* curves exhibit a typical ohmic conduction behavior, where the current is linearly related to the applied voltage. In this region, the quantity of the thermally generated free carriers exceeds that of the externally injected carriers[83]. With increasing the applied voltage, the externally injected carriers gradually increase and start to fill the traps. Therefore, a trap-filling process is identified by the end of the linear ohmic region. V_{TFL} is extracted by finding the voltage where the ohmic region ends. The extracted V_{TFL} in samples with different strains are used to evaluate the trap density. Trap density of the epitaxial film can be calculated by:

$$V_{TFL} = {en_t d^2}\Big/{2\varepsilon\varepsilon_0} \tag{2}$$

where d is the layer thickness, ε is the relative dielectric constant of $MAPbBr_3$ and ε_0 is the vacuum permittivity. Figure 8a shows the *I-V* characteristic curve of the epitaxial $MAPbBr_3$ microarray, and a 0.12 V trap-filling voltage can be extracted from the *I-V* curve. Based on the

0.12 V trap-filling voltage, the trap density of the epitaxial $MAPbBr_3$ microarray is calculated to be 5.29×10^{10} cm^{-3}, which is on par with that of the bulk $MAPbBr_3$ single crystals. The calculated trap density is also much lower compared with that of the polycrystalline $MAPbBr_3$ ($\sim10^{15}$ cm^{-3}), showing that the epitaxial $MAPbBr_3$ microarrays have high crystalline quality with minimum defect density. Low trap density also contributes to the reduced carrier non-radiative recombination and the enhanced carrier dynamics. Figure 8b shows the carrier lifetime characterizations in the epitaxial $MAPbBr_3$ microarrays and polycrystalline $MAPbBr_3$ by using time-resolved photoluminescence (TRPL) spectroscopy. TRPL measures the radiative decay of the charged carriers upon excitation by the incident photons. We note that the carrier lifetime can be extracted by fitting the TRPL radiative decay by the component exponential decay equation. Results show that the extracted carrier lifetime in the epitaxial $MAPbBr_3$ microarrays is much longer than that of the polycrystalline $MAPbBr_3$, indicating the severe non-radiative carrier recombination in the polycrystalline $MAPbBr_3$. Due to the enhanced crystalline quality and reduced trap density, the epitaxial $MAPbBr_3$ microarrays have minimum trap-assist non-radiative carrier recombination and exhibits a longer carrier lifetime. We note that the carrier lifetime is calculated by fitting the TRPL decay intensity with the exponential decay equation.

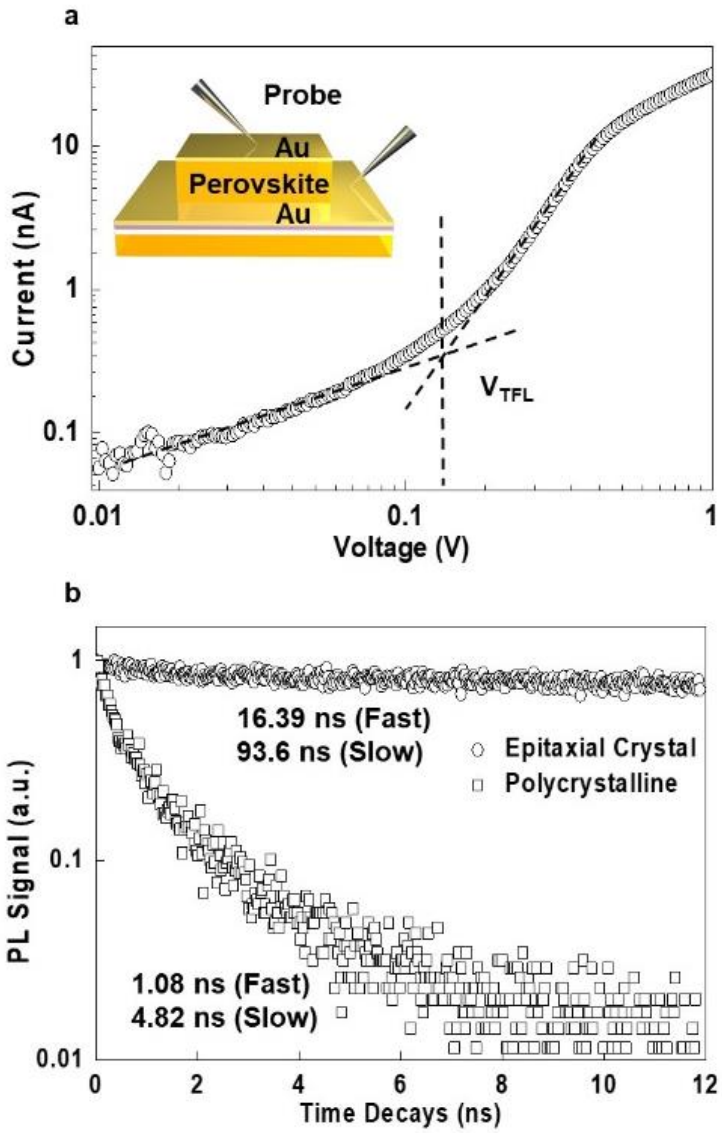

Figure 8. Crystalline quality and carrier dynamics study of the epitaxial $MAPbBr_3$ microarrays.
a, *I-V* characteristic curve of an epitaxial $MAPbBr_3$ microcube. Inset, schematic measurement setup. **b,** TRPL decay of an epitaxial $MAPbBr_3$ microcube and a polycrystalline $MAPbBr_3$ thin film. Results indicate a much longer carrier lifetime in the epitaxial $MAPbBr_3$.

To further study the carrier dynamics of the epitaxial $MAPbBr_3$ microarrays, carrier mobility is characterized by the Hall effect measurement (Lake Shore Hall measurement system HM 3000) with the four contacts van der Pauw method[60]. We note that the insulating Parylene-C serves as the only mask layer to avoid introducing the bottom electrode. This measurement is carried out on the epitaxial $MAPbBr_3$ thin films by merging the microarrays with elongated growth

time. Four Au contacts are deposited on the surface of epitaxial thin film by e-beam evaporation. At a growth temperature of 40 °C, the carrier mobility of the epitaxial $MAPbBr_3$ thin film is measured to be 82 $cm^2 V^{-1} s^{-1}$, which is much higher than the reported value for polycrystalline $MAPbBr_3$. We conclude that the grain boundaries annihilation and the reduction of the structural defect decrease the scattering of the charged carriers, leading to the enhanced carrier mobility in the single-crystal epitaxial $MAPbBr_3$.

2.6 Single-crystal $MAPbBr_3$ for Micro-LED Applications

Previous studies show that the first controllable epitaxial growth of $MAPbBr_3$ microarrays demonstrate a superior crystalline quality and carrier dynamics, which is comparable to those of the bulk perovskite single crystals. We then focus on transferring our advanced single-crystal growth platform to the fabrication of high-performance single-crystal perovskite electronic devices with vertical device structure and reduced dimensions. Compared with those perovskite devices with simple planar structure, perovskite LEDs require a sophisticated vertical device structure with appropriate emitter thickness to achieve balanced and efficient charged carrier injection. Due to the complicated transporting layer/electrode integration and unsuccessful perovskite epitaxial growth with uniformity, the study of the vertical single-crystal perovskite electronic devices with scalability is still in its infancy. The platform we demonstrated overcome these difficulties. The insertion of the water-resist Parylene-C layer enables the direct fabrication of the single-crystal perovskite substrates for sequentially patterned epitaxial growth. The strong chemical bonds formed at the interface ensure the coverage of the epitaxial perovskites and the controllability of the morphology as well as orientation. Meanwhile, the underlying mask can also serve as the

bottom electrode for a high-performance vertical device structure. In recent years, the concept of micro-LEDs has been seen as the next-generation display technique. The individual control of the self-emitting pixel with a dimension less than 100 μm provides ultrahigh resolution and contrast. Our epitaxial perovskite microarray perfectly matches this concept with controllable morphology and large-area uniformity. Besides, the annihilation of the grain boundaries and the decreased structural defects in single-crystal perovskite also inhibit the non-radiative carrier recombination. Therefore, single-crystal micro-LEDs based on the epitaxial $MAPbBr_3$ microarray are demonstrated.

To achieve balanced and efficient carrier injection to the epitaxial microarray, a layer of poly(3,4-ethylenedioxythiophene):poly(styrensulfonate) (PEDOT:PSS) is deposited as the hole transporting layer between Au and $MAPbBr_3$. To deposit PEDOT:PSS layer, 0.5 mL PEDOT:PSS (Aldrich) is mixed with 10 mL anhydrous IPA, and the mixture is treated under ultrasound for 30 min to ensure homogeneous dissolution. After this, a layer of PEDOT:PSS (~200 nm in thickness) is deposited onto the Au layer using a spray gun, with the substrate on a hot plate at 80 °C to instantaneously evaporate the solvent. Then, sequential deposition of layers of Parylene-C, poly(methyl methacrylate) (PMMA), and SiO_2 on top of the PEDOT:PSS is made to assist patterning of PEDOT:PSS. We note that the thickness of each layer would not affect the fabrication process as they are sacrificial materials to be removed. Specifically, the Parylene-C layer on the PEDOT:PSS helps to fix the PEDOT:PSS layer during the Au wet etching process to avoid the loss of PEDOT:PSS. We note that the spin-coated PMMA helps increase the adhesion between Parylene-C and SiO_2. The SiO_2 layer serves as a top patterning and etch-stop layer. After this, a photoresist is spin-coated onto the SiO_2 layer for photolithography. In the etching process, SiO_2, Parylene-C, PMMA, PEDOT:PSS, and Cr are removed by dry etching, and Au is removed by wet

etching. Then the patterned perovskite/Parylene-C/Cr/Au/PEDOT:PSS structure is obtained. Based on this structure, epitaxial $MAPbBr_3$ microarrays are grown from solution. After growing the epitaxial crystal arrays (≈5 μm in thickness), a photoresist is spin-coated on the epitaxial single crystal arrays to form an insulation layer. Slight etching of the insulation layer would expose the top portion of the epitaxial crystal array, while the bottom portion and the bottom substrate were still insulated by the photoresist layer. A layer of indium tin oxide (≈200 nm in thickness) was deposited by sputtering to form the top electrode of the final LEDs. The schematic fabrication process is illustrated in Figure 9.

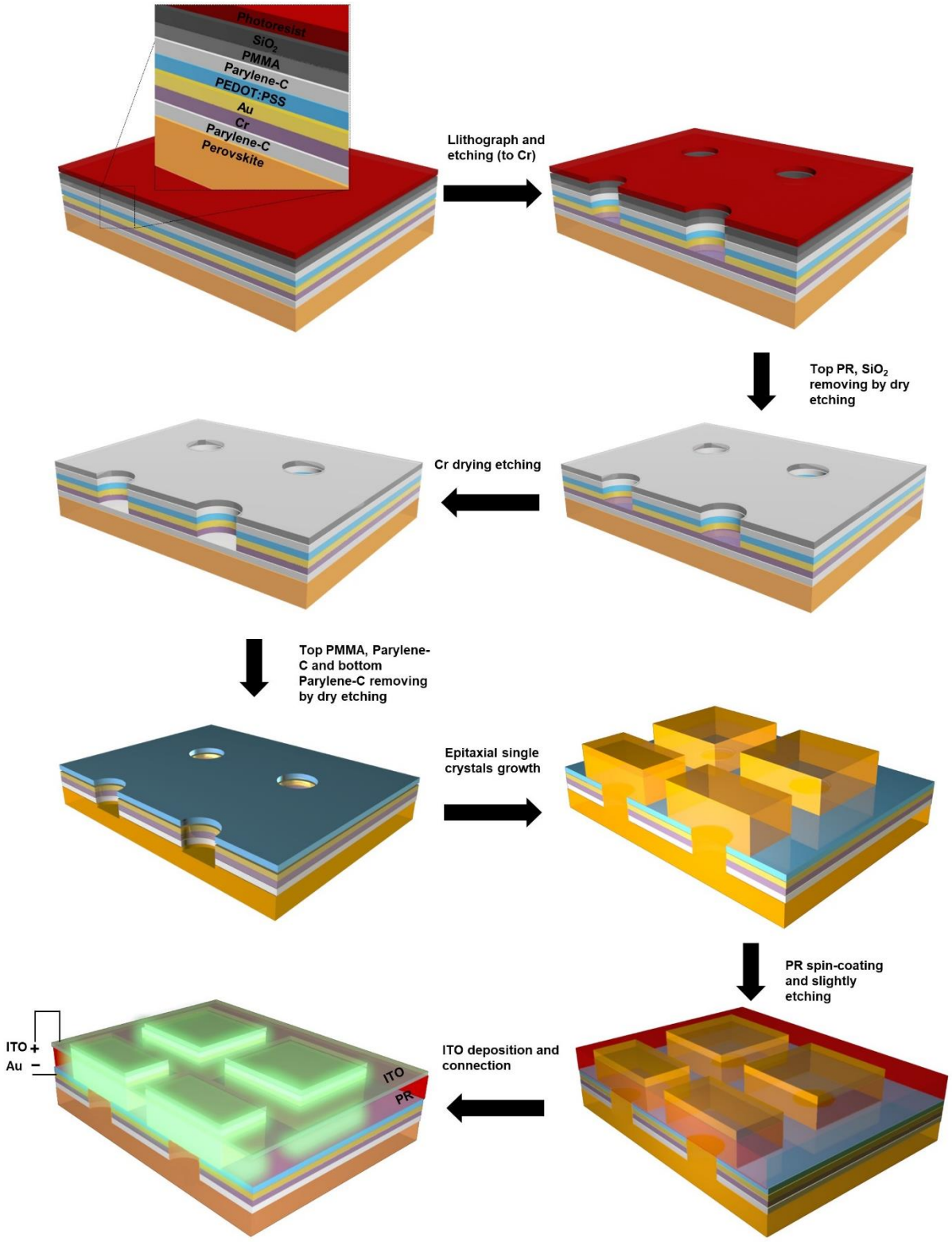

Figure 9. Schematic fabrication process of the single-crystal $MAPbBr_3$ micro-LEDs.

Figure 10a shows the flat band energy-level diagram of the LED. In this structure, the $MAPbBr_3$ serves as the light-emitting layer while the PEDOT:PSS layer serves as the hole-transporting and electron-blocking layer simultaneously by virtue of its high ionization energy and low electron affinity. By controlling the growth rate, we obtained epitaxial $MAPbBr_3$ single crystals, with ≈5 μm in height and ≈20 μm by 20 μm in footprint, which allows forming a robust contact with the bottom electrode. A working green LED array is shown in Figure 10b. The light intensity in each crystal is uniform, which is attributed to the high crystal quality observed in our material characterizations. The color of the individual pixel is almost white dues to the high emission intensity. The electroluminescence (EL) at different voltages at room temperature is shown in Figure 10c. The intensity increases with increasing the drive voltage without any emission peak shifting, which indicates the absence of radiative decay[84]. The dominant emission peak is at around 540 nm with a full width at half maximum of about 30 nm. The integrated EL intensity under different driving voltages demonstrated a saturating tendency from 8 V with the intensity slightly decreasing at 9 and 10 V, which may be due to the inevitable heating effect at high current density levels[85]. The rapid saturation in current density in Figure 10d also demonstrated an efficient carrier injection and transport in the epitaxial $MAPbBr_3$ microarray, further indicating that the leakage current, usually found in polycrystalline thin film-based devices[86], is low. The turn-on voltage for different devices displays some variability, with most devices having a low turn-on voltage from 2 to 3 V (Figure 2.8e). Figure 10f shows that the maximum external quantum efficiency (EQE) of 6.1% was achieved at 9.0 V, which is an order of magnitude higher than similar devices but with polycrystalline materials[87,88]. This maximum EQE yields an internal quantum efficiency (IQE) of 28.2%, considering the 21.6% transmission of the top electrode[89]. The increase in EQE with increasing applied voltage and current density suggests

that a high density of charges is required for efficient radiative recombination. Future studies will focus on improvements such as optimization of the hole and electron transport layer design[90] and layer interface engineering[91]. In conclusion, we demonstrated the first single-crystal metal halide perovskite LEDs based on our controllable homoepitaxial $MAPbBr_3$ microarray growth and fabrication platform.

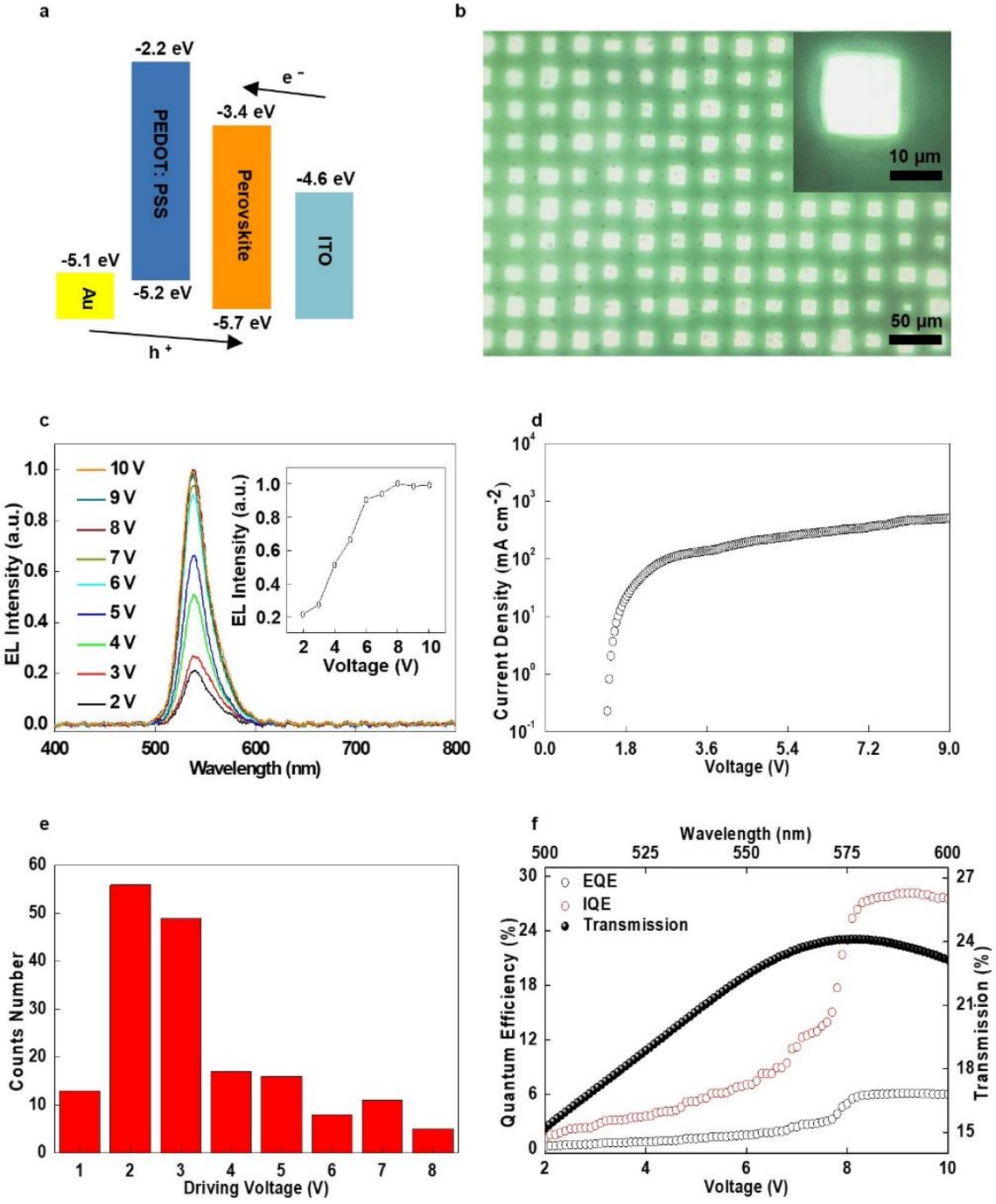

Figure 10. Characterization of the single-crystal $MAPbBr_3$ micro-LEDs.
a, Schematic energy diagram of the $MAPbBr_3$ micro-LEDs. **b,** Optical image of the $MAPbBr_3$ micro-LEDs under illumination. **c,** EL spectra of the $MAPbBr_3$ micro-LEDs. **d,** Current density of a working LED array under different driving voltages. **e,** Summary of turn-on voltages needed to light up the epitaxial single crystal LEDs. **f,** EQE, transmission, and IQE of the epitaxial single-crystal LED array. An EQE of 6.1% is achieved at 9.0 V.

2.7 Conclusion

In this chapter, we demonstrate, for the first time, the homoepitaxial growth of high-quality metal halide perovskite microarray with controllable morphologies and orientations. Due to the strong chemical bonds between the epitaxial layer and the substrates, the epitaxial thin film achieved an extremely high uniformity and coverage. The compositional diversity of the epitaxial layer can be realized by selecting the corresponding growth solutions and substrates.

The novel direct fabrication of the metal halide perovskite single-crystal substrate also enables a platform to integrate vertical device structure with the bottom electrode and transporting layer in single-crystal perovskite electronic devices, which provides insight into high-performance perovskite devices. This overcomes the current limit in single-crystal perovskite device design, where the vertical device structure with the bottom electrode integrated is still challenging. Based on our novel platform, we demonstrated the first single-crystal metal halide perovskite micro-LEDs.

Chapter Two, in full, is a reprint of the material ‘Controllable Homoepitaxial Growth of Hydrid Perovskites’, Lei, Y., Chen, Y., Gu, Y., Wang, C., Huang, Z., Qian, H., Nie, J., Hollett, G., Choi, W., Yu, Y., Kim, N., Wang, C., Zhang, T., Hu, H., Zhang, Y., Li, X., Li, Y., Shi, W., Liu, Z., Sailor, M., Dong, L., Lo, Y., Luo, J., Xu, S., Advanced Materials, 2018, 30, 1705992. The dissertation author was the primary investigator and co-first author of this paper.

Chapter 3. Strain Engineering of Metal Halide Perovskites by Heteroepitaxial Growth

3.1 Motivation for Metal Halide Perovskite Strain Engineering

Strain engineering has demonstrated to be a powerful and versatile tool to tune and improve material properties, such as semiconductors (such as Si[92] and GaN[93]), transition metal oxides (such as $BiFeO_3$[94] and $LaAlO_3$[95]), and emerging two-dimensional materials (such as graphene[96] and MoS_2[97]). By interplay between spin, lattice, charge, and orbital degrees of freedom, strain (either biaxial or uniaxial) allows precise controlling and engineering of the electronic band structure[98], carrier dynamics[99], metal-insulator transitions[100], multiferrocity[101], and high-temperature superconductivity[102]. Besides, strain creates novel functionalities like two-dimensional electron gas[103], topological Hall effect[104], multiferroic[105], and colossal ionic conductivity[106] at heterostructural interfaces, which are absent in their bulk freestanding form.

Besides providing alternatives for engineering material properties and functionalities, the static elastic deformation can also effectively tune the device performance. The slow-down in metal oxide semiconductor FET (MOSFET) scaling due to the physical limits requires alternative techniques to further enhance the device performance. Strained Si, Ge, and SiGe have been successfully applied in fabricating high mobility MOSFET for fast switching[107]. Similarly, strained-engineered III-V material GaN also shows potential for high electron mobility transistor. It has also been shown that the strained III-V multi-quantum well structure with different dimensions can effectively tune the optical emission range, providing insight into display technology[108]. Besides, the strain is also reported to increase the optical efficiency in GaN-based LED[109]. For 2D materials like MoS_2, strain engineering opens applications in the field of

photovoltaics by inducing exciton funneling property.

To further improve the performance of metal halide perovskite electronic devices, the concept of strain engineering has been brought out. Currently, halide perovskite strain engineering is now receiving increasing attention in the field. Different from the conventional semiconductors and perovskite oxides, the controllable strain engineering by heteroepitaxial growth of halide perovskites has not been properly achieved yet, which is due to inappropriate growth methods and the absence of suitable lattice-mismatched substrates, therefore the lack of strong chemical bonds formed with the substrates. In this case, a controllable and scalable method for strain engineering single-crystal halide perovskites is still critically needed.

3.2 Current Studies of Metal Halide Perovskite Strain Engineering

Epitaxial growth of halide perovskites has been reported by many groups, but most of the works have been van der Waals epitaxy that is absent from strong interfacial chemical bonds[69,110,111]. Despite the weak nature of van der Waals bonds, nontrivial effects from van der Waals interaction to the epitaxial halide perovskites have been demonstrated due to the soft nature of halide perovskites[64]. Besides van der Waals epitaxy, chemical epitaxy by forming interfacial ionic bonds has also been reported[71,72]. However, due to the extremely high growth temperature (~500 °C), the interface was destroyed by the high diffusion rate of ions at such a high temperature and therefore, no interfacial strain could be detected. Other than epitaxial strain, thermally strained halide perovskites have also been studied. The thermal expansion coefficient difference between a patterned substrate and the halide perovskite was utilized to induce thermal strain to a perovskite microcrystal[112]. A thermally strained halide perovskite by introducing a phase transition of the

substrate via increasing the temperature has also been demonstrated[63]. In this case, the thermal strain is highly dependent on the temperature and the magnitude of the strain cannot be well controlled.

Besides manipulating single-crystal halide perovskites, researchers are also creating strain in polycrystalline thin films by a variety of methods. One of the most popular methods is the ion substitution of a larger/smaller ion that can induce local tensile/compressive strain in the perovskite lattice[113,114]. Local compressive strain by small ion substitution was found to improve the stability of halide perovskites[114]. It was demonstrated that the local compressive strain by ion substitution could suppress the vacancy formation in halide perovskites[113]. Additionally, the crystalline quality of halide perovskites could be controlled by local strain via ion substitution[115]. Besides ion substitution, it was also reported the control of the local strain by light-induced lattice expansion[116]. The local strain was found to affect the optoelectronic properties of halide perovskites by creating defect distribution heterogeneity[117]. Recently, residual strain in polycrystalline halide perovskite films induced by the thermal annealing process has been reported. The residual strain in the polycrystalline methylammonium lead iodide film was found to have an impact on the perovskite stability[118]. Also, residual strain in the polycrystalline mixed halide perovskite film was reported to affect the carrier dynamics[119] and phase transition[120]. Hydrostatic pressurization was another commonly used method to apply strain to the halide perovskites. The crystal structure[121] and electronic band structure, including bandgap[122] and carrier dynamics[123,124] were found to be highly subjective to the applied pressure. Metallic properties of halide perovskites were also reported under applied pressure[125]. Although the strain engineering of metal halide perovskites has been frequently attempted, a controllable method to strain the perovskites is critically needed.

3.3 Strain Engineering of Heteroepitaxial α-$FAPbI_3$

With the successful demonstration of metal halide perovskite homoepitaxial growth, heteroepitaxial growth provides insight into the strain engineering of perovskites by introducing a lattice mismatch at the epitaxial interface. Besides, the miscibility of metal halide perovskites can effectively tune the lattice constant, which in turn creates a tunable lattice mismatch at the epitaxial interface.

α-$FAPbI_3$ was epitaxially grown on a series of $MAPbCl_xBr_{3-x}$ single-crystal substrates by the reverse temperature growth method[126], as illustrated in Figure 11.

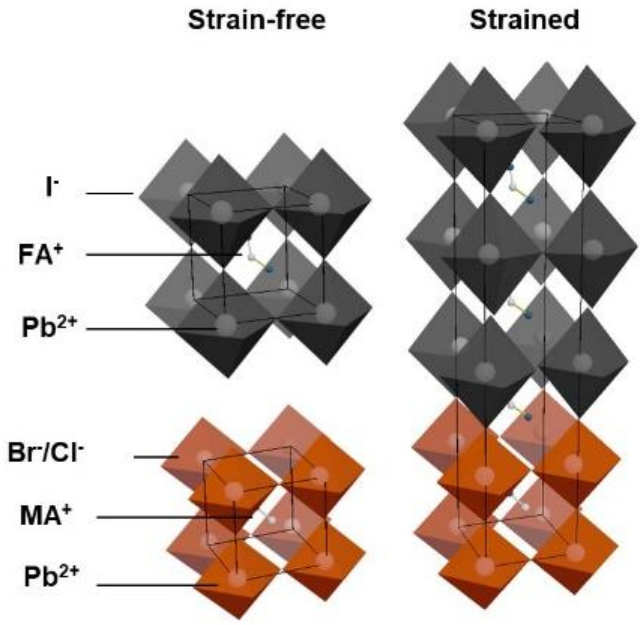

Figure 11. Schematic crystal structures of epitaxial α-$FAPbI_3$ on $MAPbCl_xBr_{3-x}$ substrate. Schematic crystal structures of α-$FAPbI_3$, $MAPbCl_xBr_{3-x}$, and the epitaxial heterostructure showing the crystallographic orientation of the epitaxial α-$FAPbI_3$ and the $MAPbCl_xBr_{3-x}$ substrate, with distorted PbI_6 octahedron inorganic framework in the epitaxial layer under compressive interfacial strain.

Specifically, the substrates were heated to different temperatures, and the preheated $FAPbI_3$ solutions (at 100 °C) are then deposited onto the substrates for epitaxial growth. $FAPbI_3$ solutions

were prepared by mixing formamidinium iodide (FAI, 99.9%, Greatcell Solar) and lead iodide (PbI_2, 99.99%, Tokyo Chemical Industry) at a molar ratio of 1:1 in gamma-butyrolactone (GBL, anhydrous, Sigma Aldrich) with different concentrations. The $MAPbCl_xBr_{3-x}$ substrates with different compositional ratios are grown by solutions with different Cl/Br precursor molar ratios. Specifically, $MAPbCl_3$ solution is prepared by mixing 0.6752 g of methylammonium chloride (MACl, 98%, Tokyo Chemical Industry) and 2.781 g lead chloride ($PbCl_2$, 99%, Alfa Aesar) in a mixed solution of 5 ml anhydrous dimethylformamide (99.8%, Aldrich) and 5 ml anhydrous dimethyl sulfoxide (DMSO, 99.8%, Aldrich). $MAPbBr_3$ solution is prepared by mixing 1.120 g MABr and 3.670 g lead bromide ($PbBr_2$, 98%, Acros) in 10 ml dimethylformamide. The $MAPbCl_3$ and $MAPbBr_3$ solutions are mixed with different ratios. The mixed solutions are kept at room temperature to slowly evaporate the solvent, and single crystals are collected to use as substrates. Besides, strain-free α-$FAPbI_3$ single crystals are obtained by heating the $FAPbI_3$ solutions to 120 °C. By controlling the substrate composition, we can tune its lattice parameter and, therefore, the lattice mismatch/interfacial strain between the substrate and the epilayer[127]. The Cl/Br molar ratios in the crystalline substrates are carefully characterized by the powder XRD θ-2θ scan. Figure 12a shows a collection of the (001) peak locations from $MAPbCl_xBr_{3-x}$ substrates, which, regardless of the Cl/Br ratio, are reported to have a cubic structure[128].

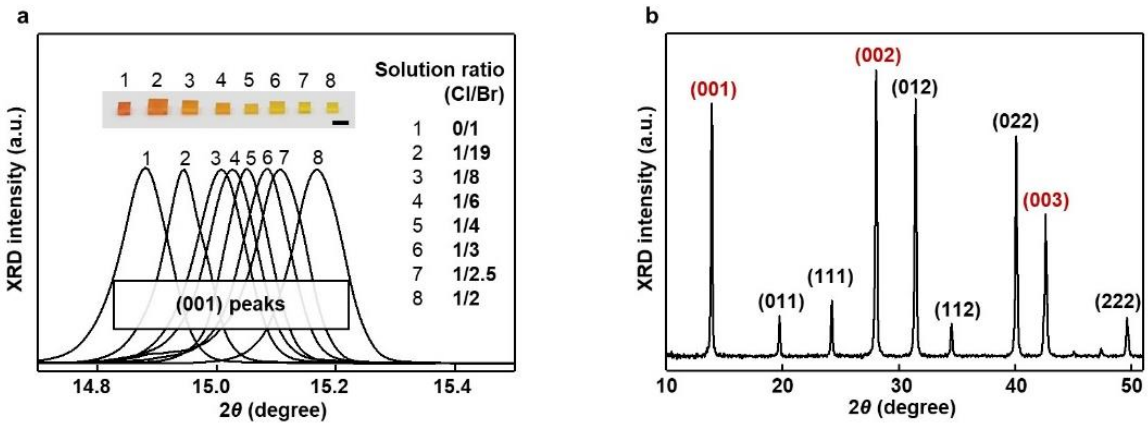

Figure 12. Characterization of the lattice parameters.
a, Powder XRD patterns of substrates with different ratios of the composition. By tuning the Cl/Br molar ratio in the growth solution, we can change the Cl/Br ratio as well as the lattice parameter of the substrate crystal. We note that $MAPbCl_{3.00}Br_{0.00}$, $MAPbCl_{0.00}Br_{3.00}$, and their alloys all have cubic structures. Lattice parameters can be directly calculated by the 2θ peak positions. The inset is an optical image of the corresponding substrates with different Cl/Br ratios. All powders are made by grinding the bulk single crystals. Scale bar: 5 mm. **b**, Powder XRD pattern of α-$FAPbI_3$, which is used as a reference of strain-free α-$FAPbI_3$. The lattice parameter of cubic α-$FAPbI_3$ is calculated to be 6.35 Å using the (001) diffraction peak at 13.92°. Peaks from <001> directions are labeled in red.

The peak position shifts to a higher 2θ angle with increasing Cl ratio, indicating a decrease in the lattice parameter. The lattice parameters of the $MAPbCl_xBr_{3-x}$ substrates were calculated by the Bragg's Law:

$$\lambda = 2d_{hkl}\sin\theta \quad (3)$$

where λ is the incident beam wavelength, θ is the angle of incidence, and d_{hkl} is the lattice d-spacing. We note that the XRD measurements are taken by a Rigaku Smartlab diffractometer equipped with a Cu Kα1 radiation source (λ = 0.15406 nm). With the lattice parameters derived from XRD measurements, the actual compositions of the substrates can be calculated by Vegard's Law[127]:

$$a_{MAPbCl_{1-x}Br_x} = (1-x)a_{MAPbCl_3} + xa_{MAPbBr_3} \quad (4)$$

where $a_{MAPbCl_{1-x}Br_x}$ is the lattice parameter of the mixed crystal, and a_{MAPbCl_3} and a_{MAPbBr_3} are the lattice parameters of $MAPbCl_{3.00}Br_{0.00}$ and $MAPbCl_{0.00}Br_{3.00}$ single crystals, respectively. The Cl/Br molar ratios of the precursors, the composition of the $MAPbCl_xBr_{3-x}$ crystal, and the calculated lattice parameters are summarized in Table 3.1. Besides, Figure 12b shows the XRD θ-2θ scan pattern of strain-free α-$FAPbI_3$ powder[126]. For strain-free α-$FAPbI_3$, the (001) peak position is at 13.92°, and the corresponding lattice parameter is calculated to be 6.35 Å.

Table 1. Summary of the substrate growth precursor ratios, the resulting substrate compositional Br ratios, and lattice parameters.

Cl/Br Solution Ratio	Compositional Br Ratio (%)	Formula	Lattice Parameter (Å)
Cl Only	0	$MAPbCl_{3.00}Br_{0.00}$	5.70
1/2	50.0	$MAPbCl_{1.50}Br_{1.50}$	5.83
1/2.5	58.0	$MAPbCl_{1.25}Br_{1.75}$	5.86
1/3	62.1	$MAPbCl_{1.15}Br_{1.85}$	5.87
1/4	64.3	$MAPbCl_{1.05}Br_{1.95}$	5.88
1/6	76.8	$MAPbCl_{0.70}Br_{2.30}$	5.89
1/8	80.6	$MAPbCl_{0.60}Br_{2.40}$	5.90
1/19	85.2	$MAPbCl_{0.45}Br_{2.55}$	5.92
Br Only	100	$MAPbCl_{0.00}Br_{3.00}$	5.95

Heteroepitaxial growth leads to controllable film thickness, preferential growth sites/orientations, compatible fabrication protocols with existing infrastructures, and scalable large-area device applications. Figure 13a shows optical images of a series of $MAPbCl_xBr_{3-x}$ substrates with a layer of epitaxial α-$FAPbI_3$ film on the top. The epilayer has a uniform thickness with a well-defined film-substrate interface from Figure 13b cross-sectional SEM image taken with a Zeiss Sigma 500 SEM operated at 3 kV. The film topography can reveal the growth mechanism and sometimes defects for strain relaxation.

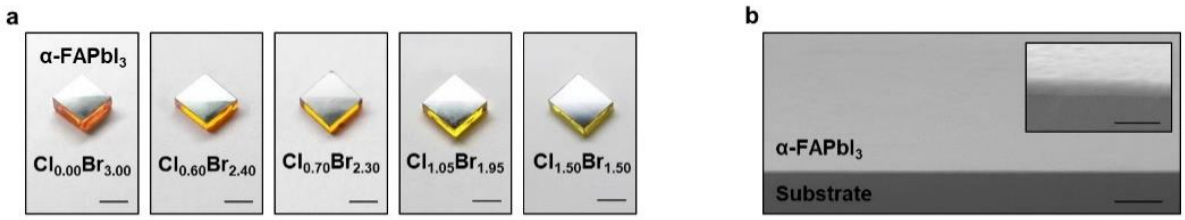

Figure 13. Epitaxial α-$FAPbI_3$ thin films.
a, Optical images of the as-grown epitaxial α-$FAPbI_3$ thin films. The high transparency of the substrates, as well as smooth surfaces of the thin films, demonstrate their high quality. Scale bars: 4 mm. **b**, A SEM image of the epitaxial thin film with controlled uniform thickness. Scale bar: 2 μm. Inset is a zoomed-in SEM image of the heterostructure showing a well-defined interface. Scale bar: 200 nm.

A sub-100 nm α-$FAPbI_3$ thin film shows a clear interface (Figure. 13b), and a well-defined terrain morphology, with a step height close to one layer of the α-$FAPbI_3$ unit cell, indicating a layer-by-layer growth behavior of the epitaxial α-$FAPbI_3$ (Figure 14a and 14b). A 10 μm film, on the other hand, shows non-conformal growth, indicating a strain relaxation by dislocation formation (Figure 14c and 14d). We note that the Atomic Force Microscopy (AFM) measurements are done by a Veeco Scanning Probe Microscope under a tapping mode.

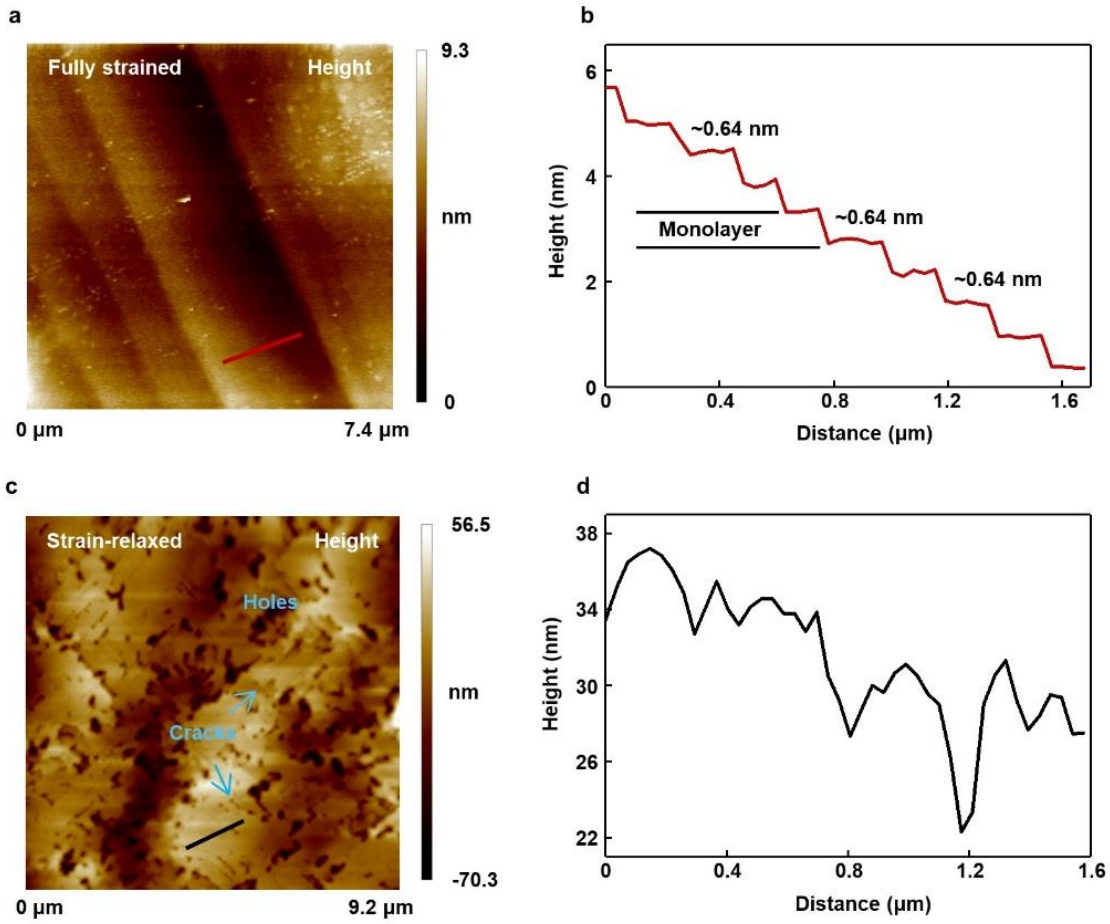

Figure 14. AFM morphology characterization of strained and strain-relaxed epitaxial α-$FAPbI_3$ films.
a, A topography image and **b**, the corresponding scanning curve of the red line in **a** of a strained epitaxial α-$FAPbI_3$ thin film. **c**, A topography image and **d**, the corresponding scanning curve of the black line in **c** of a strain-relaxed epitaxial α-$FAPbI_3$ thick film. Results show that the strained thin film adopts a layer-by-layer growth model. No cracks or holes can be detected. As the film thickness increases, the total strain energy builds up and generates dislocations that propagate throughout the film and relax the strain, leading to the formation of cracks and pits. These cracks and pits are typically regarded as a signature of strain relaxation.

The epitaxial growth conditions are systematically studied (Figure 15a and 15b). $FAPbI_3$ solutions with different concentrations are deposited on the substrates at different temperatures for epitaxial growth. Since $FAPbI_3$ has an inverse solubility in the GBL solvent, high concentration and high temperature will accelerate the crystallization of α-$FAPbI_3$. In Figure 15a, the (001) peak position of the epitaxial α-$FAPbI_3$ is studied as a function of the growth temperature. The vertical orange line labels the peak position (13.92°) of the strain-free α-$FAPbI_3$. The results show that

growth temperatures below 180 °C always generate diffraction peaks larger than 13.92°, while growth temperatures above 180 °C can generate peaks smaller than 13.92°. The diffraction peak position reveals the out-of-plane lattice parameter of the epitaxial thin film. When the growth temperature is too high, the crystallization of α-$FAPbI_3$ is fast, and many defects are incorporated, which would relax the strain in the α-$FAPbI_3$. When the growth temperature is too low, the crystallization is too slow, and Cl^-/Br^- ions may dissolve from the substrate and re-crystallize into the epitaxial α-$FAPbI_3$, forming mixed alloys at the interface, although $MAPbCl_xBr_{3-x}$ has an extremely low solubility in GBL. Diffraction peaks larger than 13.92° provide evidence for uniform lattice contraction caused by the incorporation of smaller Br^- and Cl^- ions. The epitaxial growths with different $FAPbI_3$ precursor concentrations are also investigated (Figure 15b). Similar to the effect of temperature, $FAPbI_3$ precursor concentrations that are too high will result in fast crystallization and a high defect concentration. Precursor concentrations that are too low will lead to slow α-$FAPbI_3$ crystallization, and thus the incorporation of Cl^-/Br^- ions that form alloys at the interface.

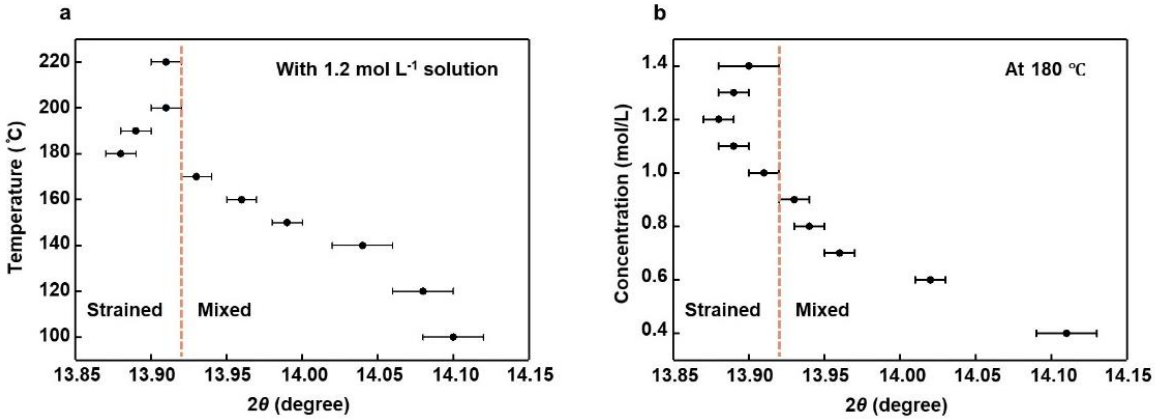

Figure 15. Study of the growth condition.

a, XRD (100) peak positions of α-$FAPbI_3$ at different growth temperatures. The temperature to grow α-$FAPbI_3$ with the highest strain is found to be ~180℃. Further increasing the growth temperature results in a high growth rate and a thick epitaxial layer of α-$FAPbI_3$ and, therefore, low crystal quality that relaxes the strain. Decreasing the growth temperature below 180℃ can lead to slow crystallization and, thus, a mixed epitaxial alloy layer at the interface, which shifts the XRD peak position to higher angles. **b**, XRD (100) peak positions of α-$FAPbI_3$ at different growth solution concentrations. Concentrations above 1.2 mol L^{-1} result in high defect concentration and, therefore, strain relaxation, due to the fast crystallization rate and the thick epitaxial layer. Concentrations below 1.0 mol L^{-1} will slow down the crystallization process and lead to a mixed epitaxial alloy layer at the interface. The vertical dash lines in **a** and **b** show the peak position of a strain-free powder sample.

We also note that the α-$FAPbI_3$ fails to epitaxially grow on substrates with a Cl ratio higher than 50% (i.e., higher Cl content than in $MAPbCl_{1.50}Br_{1.50}$), because higher levels of lattice mismatch will dramatically increase the strain energy and make the epitaxial growth less thermodynamically favorable. Figure 16 shows the optical image of growth results on a $MAPbCl_{2.00}Br_{1.00}$ substrate prepared using the same method as the other substrates. In this case, the α-$FAPbI_3$ randomly crystallizes on the substrate, without forming a uniform epilayer; most of the black α-$FAPbI_3$ crystals undergo a phase transition to yellow δ-$FAPbI_3$ due to the phase instability of α-$FAPbI_3$ at room temperature.

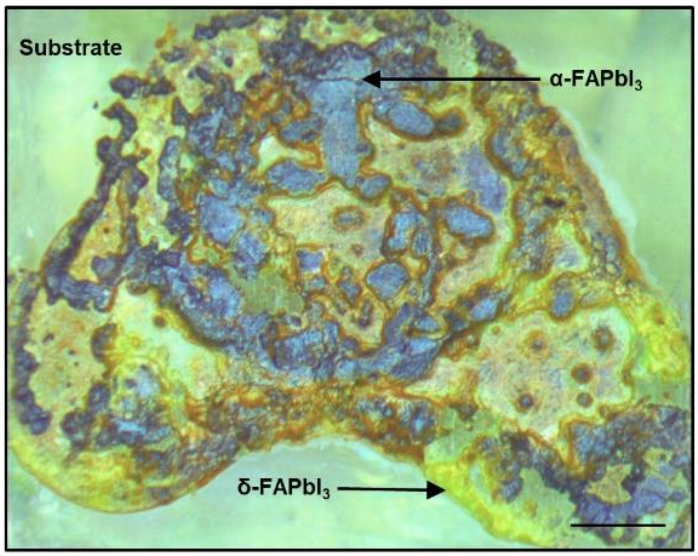

Figure 16. Optical image of α-$FAPbI_3$ on a Cl-rich substrate.
An optical image of $FAPbI_3$ grown on $MAPbCl_{2.00}Br_{1.00}$ substrate using the same growth method as the other substrates. Due to the large lattice mismatch between the substrate and α-$FAPbI_3$, the α-$FAPbI_3$ crystallizes randomly rather than epitaxially on the substrate surface. The lack of epitaxial stabilization leads to quick phase transformation from metastable α-$FAPbI_3$ to δ-$FAPbI_3$ at room temperature. Scale bar: 200 μm

3.4 Structural Characterizations of the Strained α-$FAPbI_3$

The crystallographic relationships between the $MAPbCl_xBr_{3-x}$ substrates and the epitaxial α-$FAPbI_3$ thin films are illustrated by High-resolution X-ray Diffraction (HRXRD) (Figure 17).

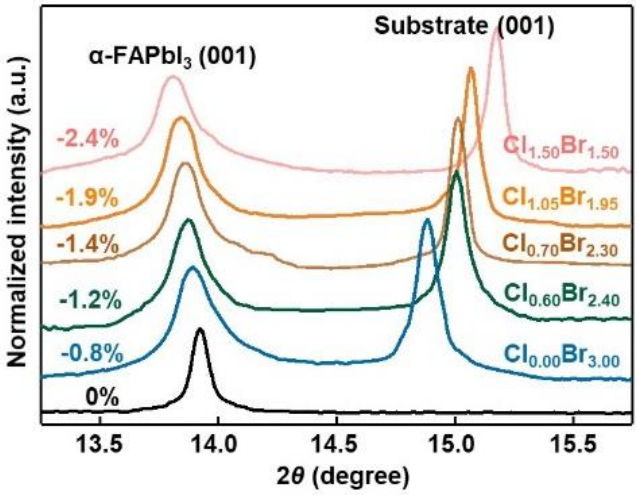

Figure 17. Structural characterization of the strained α-$FAPbI_3$ by HRXRD.
HRXRD ω-2θ scan of the (001) peaks of the epitaxial samples on different substrates showing the increase of tetragonality with increasing the lattice mismatch.

In their freestanding form, both α-$FAPbI_3$ and $MAPbCl_xBr_{3-x}$ have a cubic structure[129,130]. The lattice parameters of freestanding α-$FAPbI_3$ (Pm3m space group) and $MAPbCl_xBr_{3-x}$ substrates (Pm3m space group) are calculated to be 6.35 Å (Figure 12b) and 5.83 – 5.95 Å (Figure 12a and Table 1), respectively. The ratio x for each composition is then calculated to be 0 - 1.50, according to the Vegard's Law (Table 1). As x increases, the $MAPbCl_xBr_{3-x}$ (001) peaks shift to a higher 2θ angle, indicating a decrease of the substrates' lattice parameters and, therefore, an increase of the lattice mismatch (Figure 17 and Table 2). Meanwhile, the α-$FAPbI_3$ (001) peak shifts to a lower 2θ angle, indicating an increase of the out-of-plane lattice parameter as the in-plain compressive strain increases. We note the strain in the epilayer is not only determined by the

lattice mismatch, but also the relaxation mechanisms. Lattice distortion relaxes the strain, so the region near the heteroepitaxy interface has the highest strain, which gradually drops at regions distant from the interface. The total elastic strain energy increases as the film grows thicker, until it eventually crosses the threshold energy for structural defect generation, and dislocations will form to partially relieve the misfit[131]. A slow growth rate of the epilayer is chosen as it also impacts the defect concentration in the epilayer. For example, a high growth rate at high temperatures or with high precursor concentrations generates large defect concentration that significantly decreases the strain in the epilayer.

Table 2. Summary of epitaxial growth substrates and the corresponding strain measured in α-$FAPbI_3$.

Substrate Composition	α-$FAPbI_3$ (001) Peak (degree)	Strain (%)
$MAPbCl_{1.50}Br_{1.50}$	13.82	-2.4
$MAPbCl_{1.05}Br_{1.95}$	13.84	-1.9
$MAPbCl_{0.70}Br_{2.30}$	13.86	-1.4
$MAPbCl_{0.60}Br_{2.40}$	13.87	-1.2
$MAPbCl_{0.00}Br_{3.00}$	13.89	-0.8

The structures of α-$FAPbI_3$ at different strains (0% – -2.4%, on different substrates) are also studied by Raman spectroscopy. We note that the Raman spectroscopy measurements are carried out by a Renishaw inVia Raman spectrometer. Figure 18a shows the strain-dependent Raman spectra of the epitaxial α-$FAPbI_3$. We attribute the peak at around 136 cm^{-1} to the stretching of the Pb-I bond[132], increases in intensity and broadens in width as the strain increases. The cubic structure of strain-free α-$FAPbI_3$ is less Raman-active, and the detectable signal is usually broad and weak. When in-plane compressive strain increases, the inorganic framework gradually gains tetragonality and produces a stronger Raman signal with a well-distinguishable shape. What is more interesting is that at ~-1.4% strain, the peak at 136 cm^{-1} starts to split into two: a main peak at ~140 cm^{-1} and a shoulder at ~133 cm^{-1} (Figure 18b). When the strain is further increased to -

2.4%, these two peaks shift to 143 cm^{-1} and 130 cm^{-1}, respectively. We attribute the blueshift of the main peak to the compression of the in-plane Pb-I bond, and the redshift of the shoulder peak to the stretching of the out-of-plane Pb-I bond. This result is also supported by the simulated Raman spectra by first-principles calculations. To further confirm that the peak broadening in the Raman spectra originates from the strain-induced lattice deformation, we simulate the Raman spectra with first-principles calculations by the CASTEP in Materials Studios. The Raman spectra are simulated from 100 cm^{-1} to 400 cm^{-1} to compare with the experimental data. Figure 18c shows the comparison between the experimental and simulated Raman spectra of the strain-free α-$FAPbI_3$ lattice. Simulated results show a Raman peak at 124 cm^{-1}, which can be assigned to the stretching of the Pb-I bond. This is correlated with the Raman peak at ~136 cm^{-1} in the experimental result. Underestimations of the simulated Raman peak wavenumbers are commonly reported[133-135]. Possible explanations may be that the anharmonicity of the bonds and the van der Waals interactions (between the inorganic cages and organic cations) can affect the simulated results[134]. Besides, the assignment of the Pb-I stretching peak also agrees with the reported studies[136,137]. Meanwhile, we also identify a weak peak at 377 cm^{-1} from the simulated Raman spectrum, which can be assigned to the bending of the FA^+ cation. However, this peak vanishes in the experimental spectrum, probably because the organic cations in halide perovskites are highly dynamic in the inorganic framework[129,138,139]. The reorientation of the cation will lead to the weakening of the peak under room temperature[140]. This is also the reason why low-temperature Raman, which can freeze the orientation of the organic cation, can resolve the signal from the organic cations in halide perovskites[134,140]. Note that the weak Raman band at ~250 cm^{-1} from the experimental Raman spectrum is assigned to the Pb-O bond induced by the laser oxidation[136]. We then apply -2.4% strain to the α-$FAPbI_3$ lattice and comparison between the experimental and simulated Raman

spectra of the strained α-$FAPbI_3$ lattice is shown in Figure 18d. An obvious peak splitting due to the in-plane Pb-I bond compression and the out-of-plane Pb-I bond stretching can be observed from the simulated Raman spectrum. This agrees with the experimental Raman peak, which shows obvious broadening due to the peak splitting. In fact, the strain-induced Raman peak splitting is also reported in other materials[141-143]. We also notice the increase of the peak intensity, which is due to the breakage of the Raman-inactive cubic symmetry[144]. Therefore, we demonstrate that the Raman peak broadening originates from the strain-induced peak splitting. Strain leads to the in-plane compression and out-of-plane stretching of the Pb-I bonds in the α-$FAPbI_3$ lattice, splitting the Pb-I stretching peak, and broadening the peak FWHM. We note that the control experiments exclude any the Raman signals from the substrate (Figure 18e).

Besides, we also studied the Raman spectra of α-$FAPbI_3$ of various thicknesses on $MAPbCl_{1.50}Br_{1.50}$ (Figure 18f). The results are consistent: a strong and sharp peak is detected from a sub-100 nm film with -2.4% strain, while a weak and broad peak is detected from a ~2 μm film, where the misfit strain is relaxed near the film surface.

Figure 18. Structural characterization of the strained α-$FAPbI_3$ by Raman spectroscopy. **a**, Confocal Raman spectra of the epitaxial layer at different strains. The evolution of the shape and intensity of the peak with the strain is attributed to the increase in lattice tetragonality under higher strain. Note that the peak at ~250 cm^{-1} is attributed to the Pb-O bond induced by the laser oxidation. **b,** Fitting analysis of the Raman peaks. The peak at 136 cm^{-1} from the strain-free sample is attributed to the Pb-I bond. With increasing compressive strain, the peak gradually blueshifts as the bond becomes more rigid, and finally splits into a main peak that blueshifts (due to in-plane bond contraction) and a shoulder peak that redshifts (due to out-of-plane bond extension). The comparison of the experimental and simulated Raman spectra of the **c**, strain-free, and **d**, -2.4% strained α-$FAPbI_3$ lattices. The discrepancy between experimental and simulated Pb-I stretching wavenumbers may be due to the anharmonicity of the bonds and the van der Waals interactions between the inorganic cages and organic cations. For the strained lattice, an obvious peak splitting takes place in both the experimental and the simulated spectra. The splitting of the Pb-I symmetric stretching peak originates from the in-plane compression and out-of-plane stretching, while the intensity enhancement comes from the breakage of the cubic symmetry. The weak FA^+ cation bending peak at 377 cm^{-1} fails to be detected, which is due to the dynamic FA^+ cation rotation at room temperature. **e**, Raman spectra of $MAPbCl_{0.00}Br_{3.00}$, $MAPbCl_{0.60}Br_{2.40}$, $MAPbCl_{0.70}Cl_{2.30}$, $MAPbCl_{1.05}Br_{1.95}$, and $MAPbCl_{1.50}Br_{1.50}$ substrates with a 488-nm laser as the excitation source. No Raman signals can be detected in the wavenumber range of interest. Therefore, possible interference from the substrates can be excluded. **f**, Thickness-dependent Raman spectra of -2.4% strained α-$FAPbI_3$ samples. Strained α-$FAPbI_3$ thin film has a sharp and strong signal, which can be attributed to the increased tetragonality of the crystal structure. As the film thickness increases, the strain gets gradually relaxed and the lattice transforms back to less Raman-active cubic structure. The Raman peak position also shifts to lower wavenumbers because of the softer and longer Pb-I bonds (inset image).

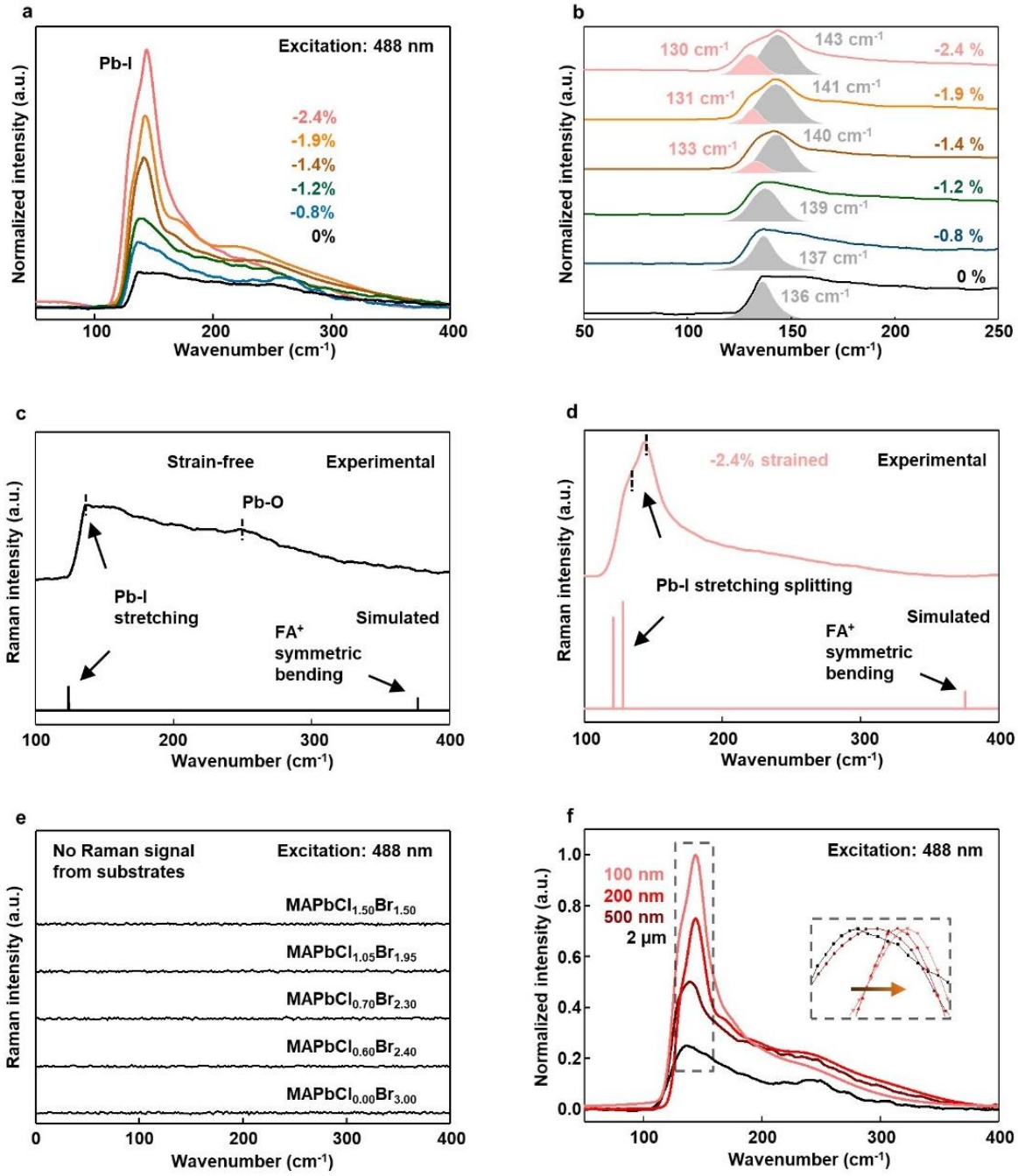
a
Excitation: 488 nm
Pb-I
-2.4%
-1.9%
-1.4%
-1.2%
-0.8%
0%
Normalized intensity (a.u.)
Wavenumber (cm-1)
b
130 cm-1
143 cm-1
-2.4 %
131 cm-1
141 cm-1
-1.9 %
133 cm-1
140 cm-1
-1.4 %
-1.2 %
139 cm-1
-0.8 %
137 cm-1
0 %
136 cm-1
Normalized intensity (a.u.)
Wavenumber (cm-1)
c
Strain-free
Experimental
Pb-O
Pb-I stretching
Simulated
FA+ symmetric bending
Raman intensity (a.u.)
Wavenumber (cm-1)
d
-2.4% strained
Experimental
Pb-I stretching splitting
Simulated
FA+ symmetric bending
Raman intensity (a.u.)
Wavenumber (cm-1)
e
No Raman signal from substrates
Excitation: 488 nm
MAPbCl1.50Br1.50
MAPbCl1.05Br1.95
MAPbCl0.70Br2.30
MAPbCl0.60Br2.40
MAPbCl0.00Br3.00
Raman intensity (a.u.)
Wavenumber (cm-1)
f
Excitation: 488 nm
100 nm
200 nm
500 nm
2 μm
Normalized intensity (a.u.)
Wavenumber (cm-1)

3.5 Optical Characterizations of the Strained α-$FAPbI_3$

Epitaxial strain effectively deforms the lattice structure of α-$FAPbI_3$, which will affect its electronic band structure and tune the optical and electrical properties of α-$FAPbI_3$. Photoluminescence (PL) spectra (Figure 19a) reveal changes in the bandgap of a sub-100 nm epitaxial α-$FAPbI_3$ thin films under different strain (0% – -2.4%, on different substrates). The PL peak of α-$FAPbI_3$ gradually shifts from ~1.523 eV at 0% strain to ~1.488 eV at -2.4% strain, corresponding to a ~35 meV reduction in the bandgap. We note that the PL measurements are carried out by a Renishaw inVia Raman spectrometer. To confirm whether the redshift of PL peaks is caused by the in-plane compressive strain, several possible mechanisms are discussed. It has been reported that as the perovskite thickness decreases, surface charges will induce depletion micro-electric field near the perovskite surface and increase the bandgap, which causes the PL to blueshift[145,146], opposite to this case here. Thus, this surface field effect can be ruled out. We also rule out the possibility of reabsorption of short-wavelength photons by the material itself, which may cause PL redshift. This effect is only observed in bulk crystals and thick films (>1 μm in thickness) and can be neglected for <100 nm films[147]. Additionally, the possible incorporation of Br or Cl element is excluded since those foreign atoms will lead to PL blueshift[148]. Hence, we can conclude that the PL redshift is due to the compressive strain generated by the lattice mismatch.

The absorption spectrum is also studied to validate the bandgap measured by PL. We note that improper measurement methods can lead to inaccurate results in both absorption and PL. For example, the absorption spectrum of thick materials obtained by the transmission mode cannot distinguish the light being absorbed or being scattered due to the large thickness of the sample[149]. Meanwhile, PL emission peaks show dependence on the illumination intensity[150] as well as material dimensions[145]. Therefore, absorption and PL measurements can be used to validate each

other. Due to the large thickness (1 to 2 mm) and the high absorption coefficients (~10^5 cm^{-1}) of the substrates, light transmittance cannot be detected[151]. Therefore, we adopt the reflection mode of UV-VIS to detect the absorption onset of the samples. The collected absorption results (Figure 19b) also demonstrate a red-shift when the strain goes up, which is consistent with the PL measurements.

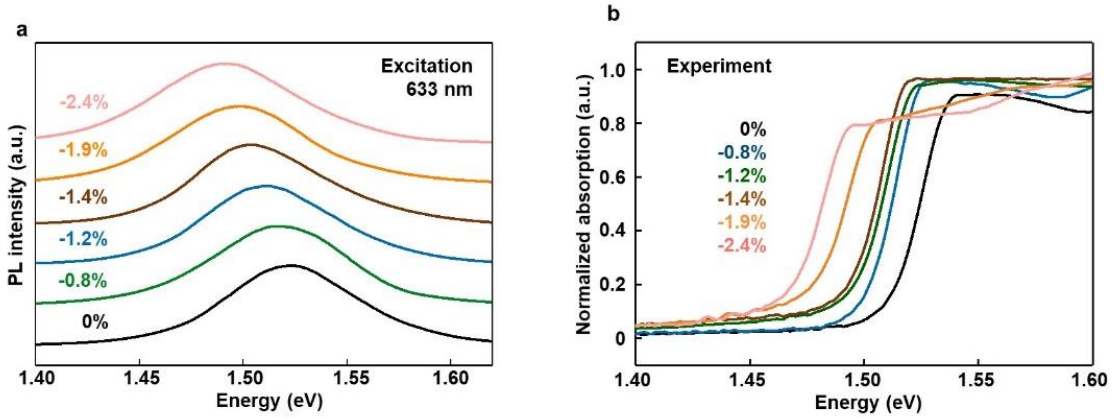

Figure 19. Strain-dependent bandgap of the epitaxial α-$FAPbI_3$.
a, PL spectra of α-$FAPbI_3$ at different strains. The redshift of the PL peak with strain is due to bandgap reduction under compressive strain. **b,** The absorption spectra of the strained α-$FAPbI_3$ thin films. The absorption onset redshifts with the increasing strain, which agrees with the PL spectra and prove that the strain can alter the bandgap of the α-$FAPbI_3$.

The bandgap change is consistent with the first-principles calculations and absorption measurements (Figure 20**)**. First-principles calculations allow a better understanding of the structural deformation and prediction of any emerging new properties. Cubic α-$FAPbI_3$ unit cells are calculated with the N-N axis of the FA^+ cation along (001), (101), and (111), respectively (left panel of Figure 3.10). These three low Miller index directions represent FA's typical orientations, and their calculated total energies could reveal potential orientation preferences. As the first step,

we optimized the cubic lattice parameter for each orientation to obtain the lowest total energy. Our calculations show a = 6.35 Å for the FA along (001), a = 6.40 Å for the FA along (101), and a = 6.37 Å for the FA along (111). The optimized structure with the FA along (101) has the lowest total energy of -52.73 eV, and the optimized structure with the FA along (001) shows the highest total energy of -52.68 eV. The total energy difference between these two structures is within 50 meV, and thus the structural model with FA along (101) direction was used in our calculations. Then we applied bi-axial strains in the ab-plane of the optimized structure for each orientation. The range is from 3% tensile strain to -3% compressive strain. The strained cells keep their original FA orientation after optimization along the z-direction. The calculated bandgap energy (lower right of Figure 20) and cell volume (upper right of Figure 20) are displayed as a function of the bi-axial strain. The cell volume decreases as the strain changes from tensile to compressive for each FA orientation. This is a result of the decreased a and b and slightly increased c. The bandgap decreases as well when the strain changes from tensile to compressive for each FA orientation.

We note that the first-principles DFT calculations were performed using the Vienna ab Initio Simulation Package[152]. Electron-ion interactions were described using the Projector Augmented Wave pseudopotential[153]. Electron-electron exchange-correlation functional was treated using the Generalized Gradient Approximation parametrized by Perdew, Burke, and Ernzerhof[154]. For bandgap calculations, spin-orbit coupling (SOC) was incorporated due to the heavy element Pb, and hybrid functionals within Heyd–Scuseria–Ernzerhof (HSE) formalism with 25% Hartree–Fock (HF) exchange were employed. A cutoff energy of 400 eV for the plane-wave basis set was used. All structures were fully optimized until all components of the residual forces were smaller than 0.01 eV/Å. The convergence threshold for self-consistent-field iteration was set at 10^{-5} eV.

Meanwhile, we notice that there is a quantitative discrepancy between the calculated bandgap reduction (~120 meV) and the experimental bandgap reduction (~35 meV) under -2.4% compressive strain. Note that the first-principle calculations of the strain-dependent bandgap serve as a general prediction. The main purpose is to predict the trend of the change instead of showing quantitative agreement with experimental results. Due to the approximation in the exchange-correlation functionals, deviation in the order of 10^2 meV in calculated bandgap energy from experiments is within a reasonable and tolerable range. Additionally, the geometry approximation of the strained lattice model doesn't reveal the actual deformation of the strained lattice. For example, the lattice parameters a and b are set to be different values to mimic different in-plane biaxial strain levels in the simulation, which changes the bond length between atoms. In real lattice deformation, however, the bond angle will also change to accommodate the in-plane biaxial strain (e.g., by octahedral rotation). Therefore, the calculated values can be different from the experimental values.

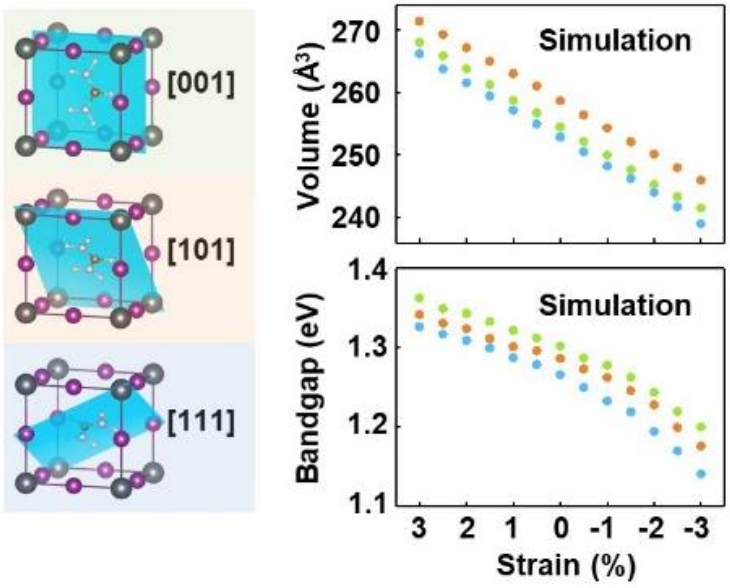

Figure 20. First-principles calculations of the strained α-$FAPbI_3$.
Evolution of the bandgap as a function of strain for three α-$FAPbI_3$ lattices with different FA^+ organic cation orientations.

Additionally, we studied the focal-point-dependent confocal PL spectra at different locations in a ~3 μm α-$FAPbI_3$ film on $MAPbCl_{1.50}Br_{1.50}$ (Figure 21a). The PL peak shifts from ~1.479 eV when the laser is focused at the interface where the local strain is high, to ~1.523 eV at 3 μm from the interface where the strain is relaxed. As a control, the PL redshift in a strain-free sample is less obvious (from ~1.516 eV to ~1.523 eV, Figure 21b), which is attributed to reabsorption[147]. Besides, focal-point-dependent confocal PL spectra of a mixed epitaxial α-$FAPbI_3$ grown at a low temperature indicate that increasing the focus depth causes the PL peak to blueshift, which is due to the increase of Br and Cl incorporation in the epitaxial layer (Figure 21c).

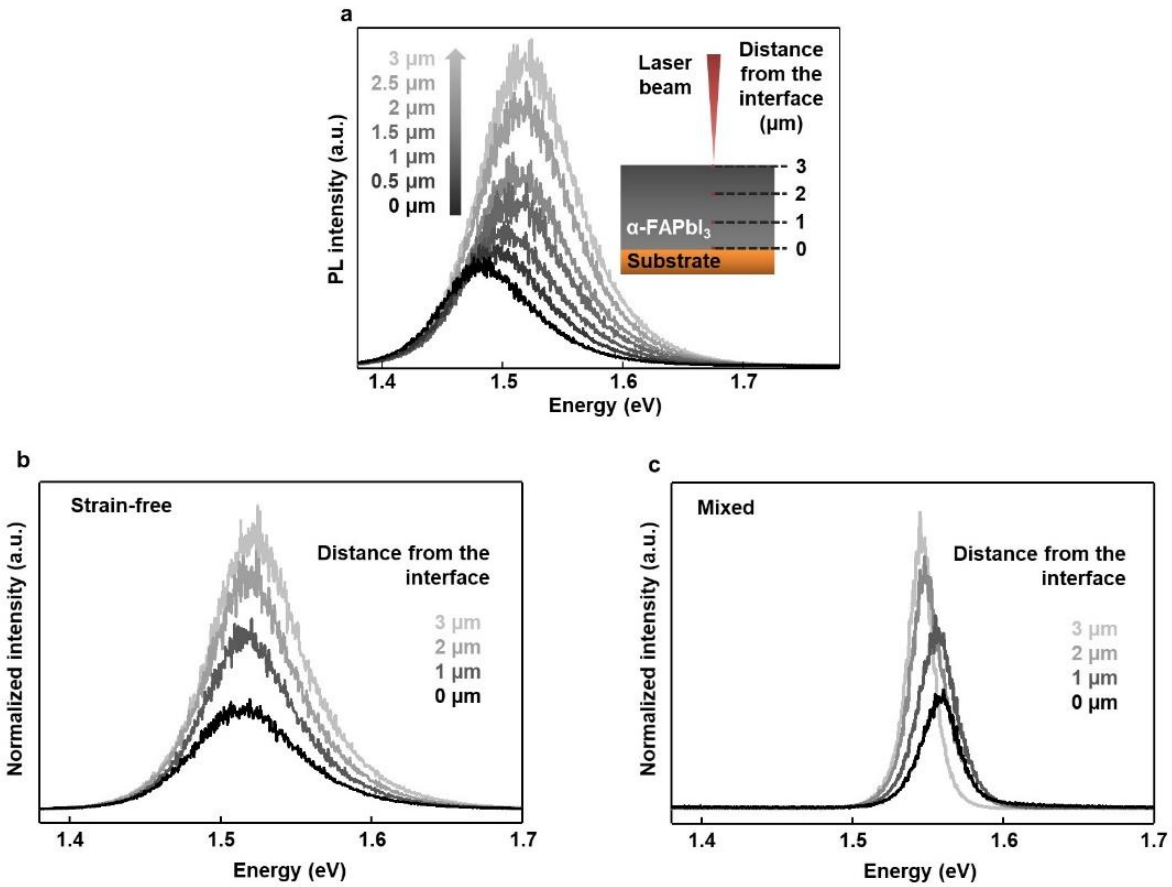

Figure 21. Focal-point-dependent confocal PL measurements of the strained, strain-free and mixed α-FAPbI$_3$.
a, Focal-point-dependent confocal PL spectra of a 3 μm thick film. When the focal point moves towards the epitaxial interface, the PL emission peak shifts from ~1.523 eV to ~1.479 eV, which is due to the large compressive strain close to the interface. **b,** Focal-point-dependent confocal PL spectra of a strain-free α-FAPbI$_3$ bulk crystal. The redshift of the PL peak from ~1.523 eV to ~1.516 eV, less pronounced than the PL peak redshift of the strained sample in **a**, is due to reabsorption. **c**, Focal-point-dependent confocal PL spectra of a mixed epitaxial α-FAPbI$_3$ grown at a low temperature. The increase of focus depth causes the PL peak to blueshift, due to the increase of Br and Cl incorporation in the epitaxial layer.

Temperature-dependent PL studies show the bandgap of α-FAPbI$_3$ under both 0% and -2.4% strain shows a strong temperature dependence due to the soft nature of α-FAPbI$_3$ (Figure 22)[122]. Due to the soft nature, external stimuli (i.e., temperature, pressure) can effectively alter the lattice structure of halide perovskites, and, therefore, change the electronic band structures[122,124,155]. Under such considerations, temperature-dependent PL was studied on both

epitaxial α-$FAPbI_3$ and free-standing α-$FAPbI_3$. Epitaxially grown thin films are subjected to the lattice deformation of the substrates due to the strong chemical bonds at the interface and the much bulkier size of the substrate. In this case, the epitaxial film will adopt a similar thermal expansion coefficient α_t to that of the substrate[156]. A reported study has shown that the α_t of halide perovskites are subjected to the molecular radius of halides. Therefore, the I-based perovskite epitaxial layer will have a larger α_t due to the large radius of I^- than the Br^- and Cl^- based halide perovskite substrate[157], and the epitaxial α-$FAPbI_3$ on a Br^- and Cl^- based substrate exhibited a reduced temperature dependency compared with the freestanding α-$FAPbI_3$. Additionally, if the substrate has a larger α_t than that of the strained layer, we should expect to see the strained sample has a stronger temperature dependence than that of the free-standing sample. Our temperature-dependent PL results show that the strained sample bandgap is less temperature-dependent compared to the strain-free sample, because of the constraint from the substrate that has a smaller thermal expansion coefficient than that of the epitaxial layer[157].

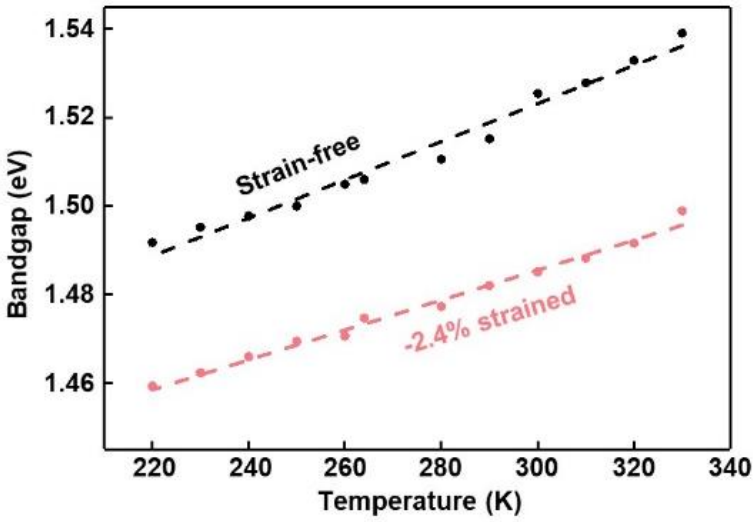

Figure 22. Temperature-dependent PL spectra of a strained and a strain-free sample.
The bandgap of the strain-free sample shows a stronger temperature dependence than the strained one, indicating that the substrate can constrict lattice deformation caused by the temperature change.

Ultraviolet photoelectron spectroscopy (UPS) reveals the band structure evolution of the α-$FAPbI_3$ under strain (Figure 23a for 0% and -2.4% strain). We note that the UPS measurements are carried out by Kratos AXIS Supra with a He I (21.22 eV) source. Figure 23b shows the cutoff energy region, and Figure 23c shows the valence band region of all α-$FAPbI_3$ under different strains. Take the UPS spectrum of the strain-free α-$FAPbI_3$ as an example, the position of the electron affinity (Fermi level) versus vacuum is the difference between the high binding energy cutoff and the radiation energy of He I (21.22 eV):

$$16.09\ \text{eV} - 21.22\ \text{eV} = -5.13\ \text{eV} \quad (5)$$

The low binding energy cutoff (0.62 eV) determines the position of Valence Band Maximum (VBM). Therefore, the position of the VBM relative to the vacuum level is:

$$-5.13\ \text{eV} - 0.62\ \text{eV} = -5.75\ \text{eV} \quad (6)$$

Considering the measured optical bandgap of ~1.51 eV, the Conduction Band Minimum (CBM) is determined to be -4.24 eV. This also suggests that the Fermi level is closer to the VBM than to the CBM, and therefore the strain-free α-$FAPbI_3$ is p-type. Similarly, all other strained epitaxial thin films show a p-type character.

In conclusion, all samples exhibit p-type behavior. The Fermi level and the VBM of the samples can be extracted from the UPS data. The results show that -2.4% strain lifts the VBM upward by ~50 meV compared to the strain-free scenario. Considering the change in the bandgap (~35 meV), the -2.4% strain pushes the CBM position upward by ~15 meV compared to the strain-free scenario. The VBM mainly consists of Pb 6*s* and I 5*p* orbitals, and the enhanced coupling between these orbitals under compressive strain pushes the VBM upward[158]. The CBM, which

consists mostly of nonbonding localized states of Pb p orbitals, is less sensitive to the deformation of PbI_6 octahedrons[122]. Therefore, the in-plane compressive strain pushes up the VBM more than the CBM.

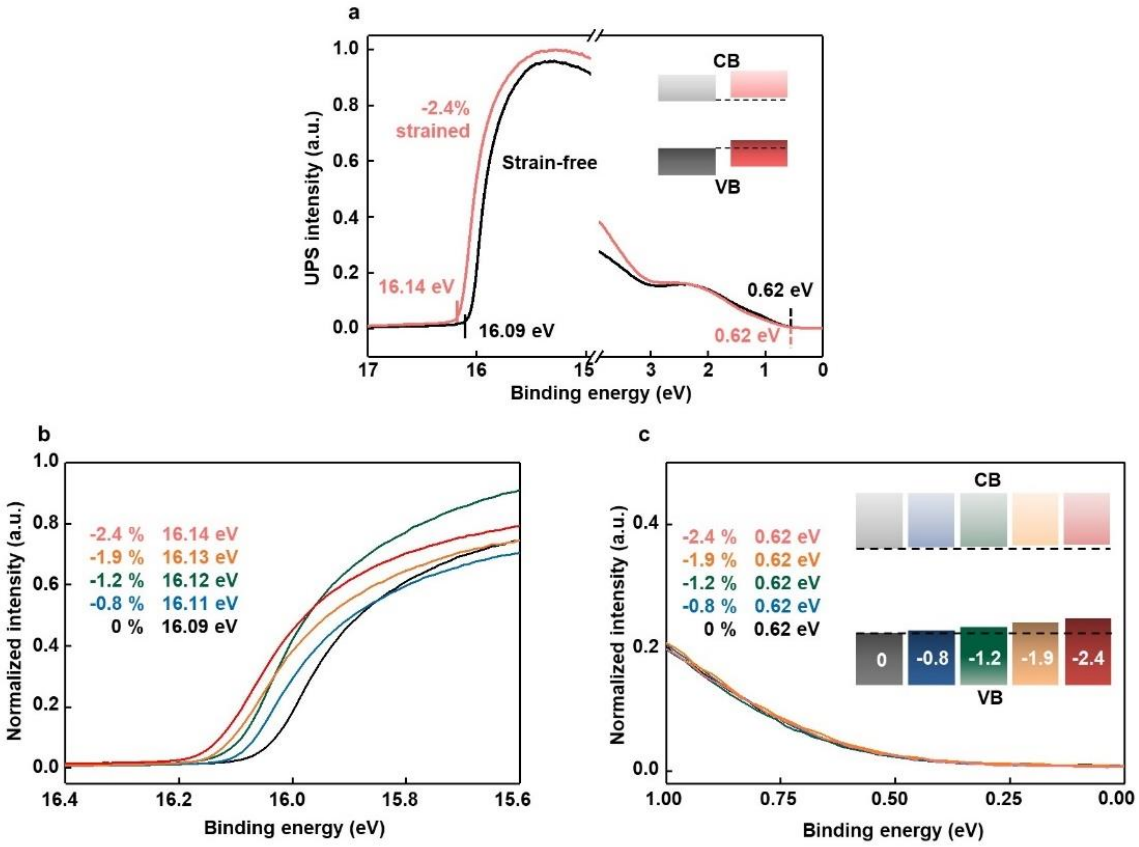

Figure 23. Electronic band structure study by UPS.
a, UPS spectra of a -2.4% strained and a strain-free sample. The Fermi level and the VBM of the samples can be extracted from the intersections of the curves with the horizontal axis, marked by the solid and dashed lines, respectively. **b**, The intersects of the curves with the baseline in the high binding energy region tell the Fermi level position of corresponding strained α-$FAPbI_3$ films. There is an obvious shift of the intersects to higher binding energy levels when the compressive strain becomes larger. **c**, The intersects of the curves with the baseline in the low binding energy region tell the energy difference between the Fermi level and the VBM. All α-$FAPbI_3$ films have p-type character according to the calculated Fermi level position in the bandgap. Meanwhile, the VBM is pushed up more than the CBM with increasing strain. A schematic band evolution is shown as inset.

3.6 Electrical Characterizations of the Strained α-$FAPbI_3$

The lattice deformation can alter the electronic band structure and, therefore, the carrier dynamics. The effective mass of charge carriers can be assessed by the band curvature extracted from first-principles calculations[159]. To investigate the effect of strain on carrier dynamics in α-$FAPbI_3$, we analyzed the variation of charged carrier mobility via predicting effective masses of charged carriers from first-principles calculations. In the calculations, the mean free time of carriers was assumed to be a constant, and the reversely proportional relationship between the effective mass and charged carrier mobility was used. Carrier effective masses are determined by the curvature of the highest energy at the VBM for holes and lowest energy at the CBM for electrons in the k space. Figure 24 shows the calculated results of electron effective mass, m_e^*, and hole effective mass, m_h^* (top panel), and three typical electronic band structures (bottom panels) under different strain. The E-k dispersion of the conduction band remains relatively unaltered, and m_e^* only shows a slight variation from 3% to -3% strain. On the other hand, a compressive strain can modulate the E-k dispersion of the valence band and reduce m_h^* considerably. This is due to the fact that the VBM that determines m_h^* mainly consists of Pb 6*s* and I 5*p* orbitals. Under tensile strain, the distance between Pb and I atoms increases and, therefore, the Pb-I bond interaction is weakened, thus leading to the increase of effective mass. In contrast, the hole mobility will increase under compressive strain due to the enhanced Pb-I bond interaction and the decreased effective mass. However, the CBM that determines the electron effective mass mainly consists of Pb p orbitals is less sensitive to the deformation of Pb-I bonds, which is why m_e^* barely changes with applied strain[119].

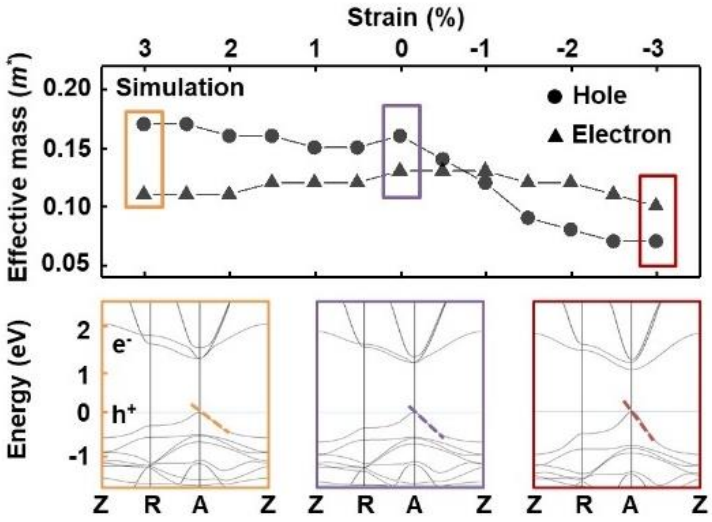

Figure 24. Calculated carrier effective masses at different strain, and electronic band structures under three strain levels (3%, 0%, and -3%).
The electron effective mass remains relatively stable with the change in strain, while the hole effective mass decreases with increasing the compressive strain. Dashed lines represent the dispersivity of the valence band; a less dispersive valence band structure indicates a smaller hole effective mass.

To validate these calculations, Hall effect carrier mobilities of the α-$FAPbI_3$ thin films under 0 – -2.4% strains are carried out. Before the Hall measurement, we study the possible carrier collection from the substrates since the substrates are halide perovskites with high carrier mobility as well. We first analyze the device structure with the Finite Element Analysis (FEA) simulation by COMSOL. The schematic device structure is shown in Figure 25a where four Au electrodes are deposited with a layer of Parylene-C beneath. The Parylene-C serves as the insulating layer to prevent the carrier collection from the substrate to the electrodes. To better understand the carrier transfer between the epitaxial layer and the substrate, we also study the band alignment between them (Figure 25b). Herein, α-$FAPbI_3$ and $MAPbBr_3$ are analyzed as an example. α-$FAPbI_3$ has a very different band structure compared with $MAPbBr_3$ in terms of bandgap, VBM as well as CBM. For α-$FAPbI_3$, VBM and CBM are determined to be -5.75 eV and -4.25 eV by the ultraviolet photoelectron spectroscopy, respectively. For $MAPbBr_3$, VBM and CBM are determined to be -

6.20 eV and -3.90 eV from the literature[160]. For the Hall measurement, the injected carriers are subject to the Lorentz force applied by the vertical magnetic field and are accumulated at the diagonal electrodes to build up the Hall voltage. However, the large energy barrier at the heterojunction interface blocks the carrier injection from the α-$FAPbI_3$ to the $MAPbBr_3$. Therefore, there is a very low concentration of free carriers in the substrate that can hardly generate a significant Hall voltage during the measurement. This analysis also applies to other substrates $MAPbCl_xBr_{3-x}$ in this study with different compositions from $MAPbBr_3$. When incorporating more Cl into the $MAPbBr_3$ substrate, the bandgap will further increase by lifting up the CBM and pushing down the VBM, and the energy barrier between the α-$FAPbI_3$ and the substrates will be even larger[161]. Thus, interfacial charge transport will be even less favorable. Additionally, we also exclude the free carrier transfer from the $MAPbBr_3$ to the α-$FAPbI_3$. We then simulate the current distribution within the device by FEA simulation. We also intend to quantify the current density in both the epitaxial layer and the substrate to study the contribution of the substrate to the Hall measurement. With the combined energy diagram and the electric field distribution, we simulate the current distribution in the device (Figure 25c upper panel). The simulation results show that the current distribution is completely different from the electric field distribution. Current density in the epitaxial layer (9.8 A m^{-2}) is much higher than that of the substrate (0.4 A m^{-2}), which means that the large energy barrier between the epitaxial layer and the substrate, as well as the minimal vertical electric field distribution and the insulation of the Parylene-C, minimizes the carrier injection to the substrate. A closer look at the area that is close to the electrode suggests that the carrier injection to the substrate is indeed prohibited (Figure 25c lower panel, red arrows indicate the direction of the current flow). To quantify the ratio of the current in the substrate to that in the epitaxial layer, we study the current density along the vertical orange line where the current flows

horizontally (at a steady state). Figure 25d shows the vertical current density distribution along the vertical orange line where the heterostructural interface locates at 500 nm from the bottom (0 nm). The ratio of current density across the interface is shown to ~ 24.5:1 where the epitaxial layer is 9.8 A m^{-2}, and the substrate is 0.4 A m^{-2}. By integrating the area below the current distribution curve, we obtain the ratio of the current density in the substrate to the total current density along the vertical line to be 0.8%. Therefore, we conclude that the carrier in the substrate is negligible compared with that in the epitaxial layer, and we attribute this result to the large energy barrier between the epitaxial layer and the substrate, as well as the minimal vertical electrical field distribution and the insulation of the Parylene-C layer.

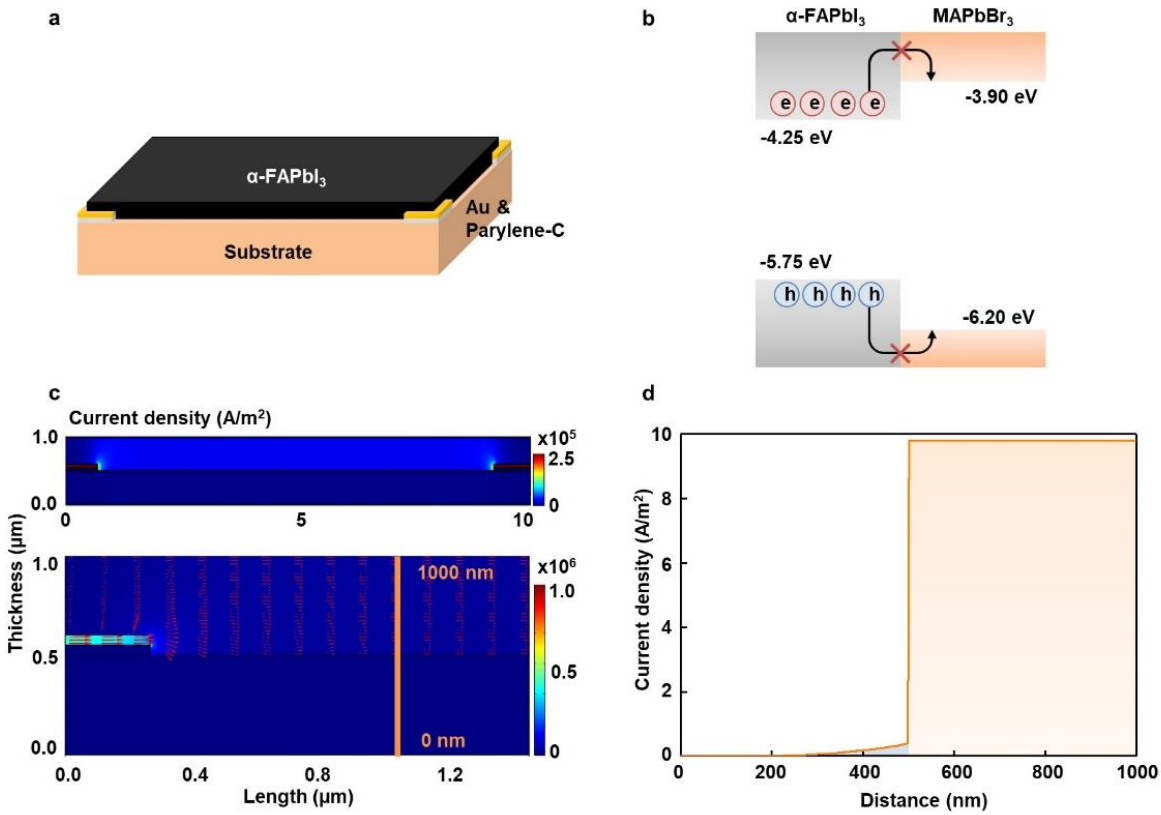

Figure 25. Possible carrier collection by the interfacial carrier transfer during Hall effect measurements.

a, The schematic structure of the device. Parylene-C (grey) is used as an insulating layer to prevent the injection of carriers from the Au electrode (yellow) to the substrate. **b**, The bandgap diagram of the heterostructure shows that the large energy barrier between the α-$FAPbI_3$ and the $MAPbBr_3$ blocks the carrier injection to the $MAPbBr_3$. **c**, Current density distribution by FEA simulation. The upper panel shows the current mapping where the current density in the epitaxial layer is much higher than that of the substrate. The lower panel shows the zoomed-in current distribution image around the electrode. Red arrows show the direction of current flow, which suggests a minimal carrier injection into the substrate due to the energy. **d**, Current density distribution along the vertical orange line in **c**, where the current in the substrate takes 0.8% of the total current.

Without the concern of possible carrier collection from the substrates, we perform Hall effect measurement to the epitaxial α-$FAPbI_3$ thin films under different strains. We note that the Hall effect measurements are carried out with a Lake Shore Hall measurement system (HM 3000) using the van der Pauw method. All samples measured by the Hall effect show a p-type character, which is consistent with the UPS results. Of all strain levels tested, films under -1.2% strain on $MAPbCl_{0.60}Br_{2.40}$ have the highest hole mobility (Figure 26). Further increasing the strain will

result in a drastic drop in the hole mobility, because of higher dislocation densities that arise at higher strain levels. Note that the devices for Hall effect measurements have an epitaxial layer thickness larger than the critical thickness to ensure a sufficient contact area between the halide perovskite and the bottom electrode. Therefore, a high strain level will induce a high concentration of dislocations that degrade the hole mobility.

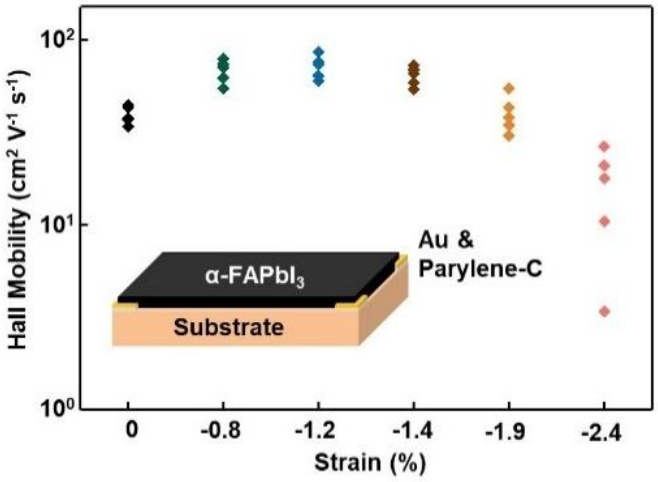

Figure 26. Strain-dependent carrier mobility characterizations by Hall effect measurement. Hole mobilities by Hall effect measurements showing -1.2% strained α-$FAPbI_3$ has the highest hole mobility. The decrease of the hole mobility with strain higher than -1.2% is attributed to the increase of dislocation density. Inset shows the structure of the measurement setup.

To validate the results from the Hall effect measurement, we study the carrier mobility of the epitaxial α-$FAPbI_3$ thin films under different strains by ToF measurements. The schematic device structure is shown in the inset of Figure 27b. A layer of Parylene-C was deposited between the Au electrode and the substrate to block the carrier extracted from the substrate as demonstrated above. Besides, we adopted a 685 nm laser as the excitation source so that the photon can only be absorbed by the epitaxial layer rather than the substrate that has a larger bandgap than the excitation laser energy. In this case, we guarantee the measured photovoltages coming from the epitaxial layer absorption are the same. Similarly, the excited electrons that occupy the CBM of the α-$FAPbI_3$ are less likely to be extracted to the CBM of the substrate due to the large energy barrier.

ToF measurements were carried out with the designed structure where the distance between the two electrodes is controlled to be 100 μm in lateral directions. The 685 nm pulse laser (10 mW/cm^2) has a pulse width $<10^{-10}$ s. The photoresponse was measured with an oscilloscope (Agilent MSO6104A Channel Mixed Signal). The thickness of the epitaxial layer is controlled to be ~500 nm, and all the devices are biased with 1 V. A 1 MΩ resistor was connected in series to simulate the open-circuit condition so that the carriers were effectively blocked in the devices[89]. The measurement was carried out in the dark while the bias and the laser power were kept at constant. The experiment setup followed the reported ToF measurement of halide perovskite single crystals[89,162-164]. The measured transient photocurrents are shown in Figure 27a where the carrier transit time can be extracted as the inflection point of the photocurrent curve. The carrier mobility can be calculated by:

$$\mu = \frac{d^2}{Vt} \tag{7}$$

where μ is the calculated carrier mobility, d is the thickness of the target region, V is the applied voltage, and t is the measured carrier transit time. The measured carrier mobilities are plotted in Figure 27b. Our measured ToF mobility of the epitaxial α-$FAPbI_3$ with different strains showed a similar trend compared with the measured Hall mobility. -1.2% strained α-$FAPbI_3$ exhibits the highest carrier mobility while further increasing the strain can lead to faster relaxation, and the accumulation of dislocations will reduce the carrier mobility. We note that the absolute mobility values from the ToF and Hall effect measurements differ, due to experimental uncertainties in the type and quality of electronic contacts made during the fabrication processes[9].

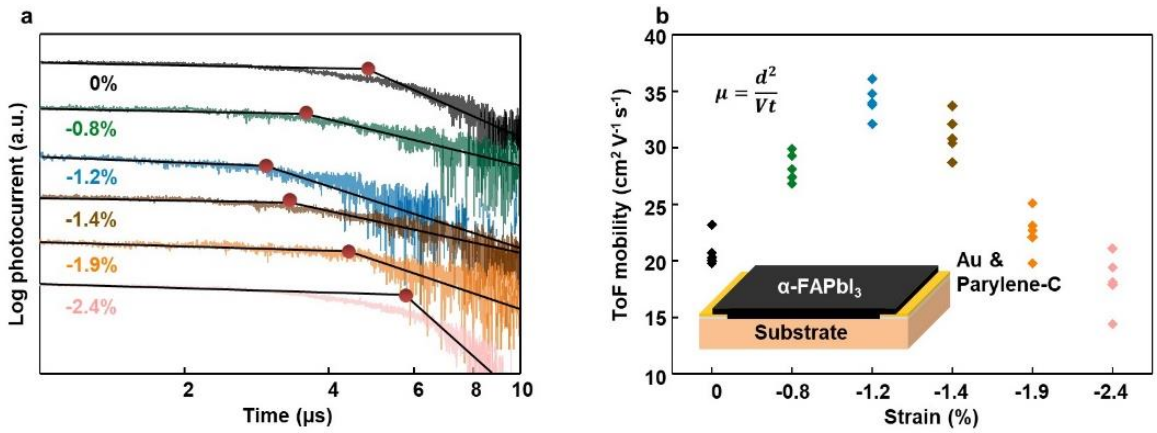

Figure 27. Strain-dependent carrier mobility characterizations by ToF measurement. **a**, Transient photocurrent curves of the epitaxial α-$FAPbI_3$ under different strain. The transient photocurrent curves are plotted on a log-log scale. The carrier transit time, the inflection point of the photocurrent curve, is marked by a solid red circle. The inflection point indicates the switching of charge transport carriers from the majority to minority carriers. **b**, Plots of calculated carrier mobilities as a function of the strain magnitudes. Inset equation transforms the carrier transit time to the carrier mobility, where μ is the calculated carrier mobility, d is the target region thickness, V is the applied voltage, and t is the measured carrier transit time.

Besides, bias and laser power dependence of the ToF measurement are also discussed. ToF mobility is calculated by $\mu = \frac{d^2}{Vt}$. The applied bias will only change the carrier transient time rather than the carrier mobility. This is because the carrier mobility is an intrinsic property of the semiconductor materials and is independent of the magnitude of the applied bias. This rule has been demonstrated by many ToF measurements of halide perovskites, in which the carrier mobility is independent of the applied bias but the measured carrier transient time is inversely proportional to the applied bias[89,162]. In the measurements, all experiments are tested under 1 V DC bias with other experimental parameters well-controlled. Therefore, the transient photocurrents of the epitaxial films under different strain magnitudes appropriately reveal the carrier mobility of the epitaxial thin films. For the ToF measurement, it has been reported that the photogenerated carrier density shows laser power dependency, and a high carrier density can generate the space charge effect which affects carrier extraction[165,166]. However, the space charge effect will be significant only in systems where the ratio between the electron mobility and the hole mobility excesses two

orders of magnitude[167]. According to the reported carrier mobility of halide perovskites, the electron and hole mobilities are usually on the same order of magnitude when they are from the same literature[9]. Therefore, the space charge effect can be safely ignored, and the laser power dependence of ToF measurements is less significant in this study. In the measurements, the laser intensity is kept at constant (10 mW cm^{-2}) throughout the entire measurement so that the only variation is the strain magnitude of the epitaxial thin film.

The possible influence of the *I-V* hysteresis on the ToF measurement is also discussed here. During the ToF measurement, the devices are biased under a constant voltage, e.g., 1 V, to collect photogenerated carriers in the epitaxial thin films. In this case, the baseline current due to ion migration and mobile electron and hole carriers under a fixed electric field is considered to be in a steady state. Adding on top of the baseline current, a pulsed laser is used as the excitation source to generate carriers in the epitaxial thin film. The corresponding photocurrent-time characteristics are recorded by an oscilloscope. The timescale of the excited transient current, i.e., ToF, is measured to be ~10^{-6} s (as seen in Figure 27a). *I-V* hysteresis is reported to originate from ion migration, device capacitive charging, and perovskite ferroelectric polarization[168,169]. For the ion migration, the timescale is reported to be in the range of seconds to minutes in halide perovskites[170], which is much longer than that of the ToF. For the device capacitive charging, whose timescale is reported to be in the range of milliseconds to seconds[168], which is also much longer than that of the ToF. Also, the timescale of ferroelectric dipole switching is reported to be faster than 10^{-8} s [171], which is much shorter than that of the ToF. Besides, since the devices are biased under 1 V DC voltage during the measurement, the capacitive charge and the ferroelectric dipoles are almost kept constant in the devices. Therefore, it is safe to exclude the possible influence of the *I-V* hysteresis on the ToF measurement.

Besides, we also study the possible influence of the ion migrations to the carrier mobility measurements. Ion migrations of halide perovskites have been studied in the literature and are believed to be the origin of the reported current-voltage hysteresis in halide perovskites. Reported studies showed that the mobility of the vacancies and the ions in polycrystalline perovskites were determined to be ~1.6×10^{-6} $cm^2\,V^{-1}\,s^{-1}$ and ~5×10^{-8} $cm^2\,V^{-1}\,s^{-1}$, respectively[172,173]. However, these values are much smaller than that of the measured hole mobilities (~50 $cm^2\,V^{-1}\,s^{-1}$) in this study. Additionally, the carrier transit time in the ToF measurement of this study was in the range of μs, which was too short for the ions to move a substantial distance. Therefore, it is safe to exclude the contribution of ions and structural vacancies from the measured hole mobility in this study. Besides, grain boundaries of the polycrystalline halide perovskites were reported to be a major pathway for ion migrations[54,174,175]. In this study, the epitaxial growth of single-crystalline perovskites minimizes the formation of grain boundaries and, therefore, minimizes the influence of the ion migrations. In a reported study, the ion migration mobility in both polycrystalline and single-crystal $MAPbI_3$ were measured[62]. Compared with the ion migration in polycrystalline $MAPbI_3$ whose ion migration mobility was ~1×10^{-9} $cm^2\,V^{-1}\,s^{-1}$, the ion migration in single-crystal $MAPbI_3$ can hardly be detected[62]. Therefore, we can conclude that the influence of ionic movements in the halide perovskites can be excluded from this study.

3.7 Crystalline Quality Characterizations of the Strained α-$FAPbI_3$

In this section, the crystalline quality of the epitaxial thin films for both structural/optical and electrical characterizations will be separately discussed since the film thicknesses used in these

two characterizations are different. The strain relaxation mechanism is also discussed to explain the crystalline quality reduction in the electrical measurements.

In our previous PL measurements, PL emission peak full width of half maximum (FWHM) of the epitaxially strained α-$FAPbI_3$ thin film is shown to increase with the strain (Figure 28a). There are multiple possibilities origins of the PL broadening. We can first rule out the influence of the domain size because the sample is a single domain thin film[176]. For semiconductors, emission linewidth broadening is governed by charged carrier-phonon coupling, including crystalline quality, acoustic phonon scattering, optical phonon scattering, and impurity[177]. In semiconductors with heterojunctions, charged carrier transfer can also take place with specific band structure at the interfaces. Such charged carrier transfer usually leads to carrier quenching without direct recombination[178-180], and emission peak shifting due to the energy change[181], while very few reported PL broadening due to the carrier relaxation[182]. Here, we discuss the possible emission peak broadening mechanism in the epitaxially strained α-$FAPbI_3$ thin films.

Possible interfacial charge transfer-induced emission peak broadening will be discussed first. The α-$FAPbI_3$ grown on $MAPbBr_3$ is analyzed as an example. α-$FAPbI_3$ has a very different band structure compared with $MAPbBr_3$ in terms of bandgap, VBM, and CBM, as shown in Figure 28b. The heterojunction shows a straddling band alignment where the charged carrier transfer is only allowed from the larger bandgap side to the smaller bandgap side when the larger bandgap side is excited. During the PL measurement in this study, a 633-nm laser (corresponding to 1.95 eV) was used for exciting the epitaxial layer (bandgap 1.50 eV) without exciting the substrates (bandgap 2.30 eV). Upon absorption, electrons in the α-$FAPbI_3$ will be excited to the conduction band while the $MAPbBr_3$ remains unexcited. Here, the large barrier between α-$FAPbI_3$ and $MAPbBr_3$ blocks the carrier transfer from the α-$FAPbI_3$ to the $MAPbBr_3$ across the interface. This

analysis also applies to other substrates $MAPbCl_xBr_{3-x}$ in this study with different compositions from $MAPbBr_3$. When incorporating more Cl into the $MAPbBr_3$ substrate, the bandgap will further increase by lifting up the CBM and pushing down the VBM, and the energy barrier between the α-$FAPbI_3$ and the substrates will be even larger[161]. Thus, interfacial charge transport will be even less favorable. Additionally, we also consider the carrier transfer from the $MAPbBr_3$ to the α-$FAPbI_3$. Since the $MAPbBr_3$ remains unexcited due to the large bandgap, the intrinsic electrons are extremely minor compared with the excited carrier in α-$FAPbI_3$. Therefore, we exclude the possibility of carrier transfer from the $MAPbBr_3$ to the α-$FAPbI_3$. Considering that the laser for the PL measurement doesn't excite the carriers in the substrate, as well as the large energy barrier that blocks the interfacial carrier transfer between the epitaxial layer and the substrate, we draw the conclusion that the charged carrier transfer between the epitaxial layer and the substrates will not take place in the PL measurements and, therefore, will not contribute to the PL broadening.

For inorganic semiconductors, emission linewidth is associated with different mechanisms of scattering between charged carriers and phonons or impurities, which can be expressed as[183]:

$$\Gamma(T) = \Gamma_{imp} + \Gamma_{ac} + \Gamma_{LO} + \Gamma_0 \quad (8)$$

where $\Gamma(T)$ is the temperature-dependent emission linewidth, Γ_{imp} is the broadening terms of scattering with impurities, Γ_{ac} and Γ_{LO} are the broadening terms of the scattering from the acoustic phonons and the optical phonons, and Γ_0 is a temperature-independent broadening term associating with the scattering due to the structural disorder, respectively.

Experimentally speaking, as mentioned above, impurity during epitaxial growth can be controlled by adopting the same growth solutions and epitaxial growth protocol. Therefore, the

impurity in the epitaxial films will have a similar concentration. The influence on the PL FWHM from impurity variation will be very minimal. Additionally, theoretical studies have identified that impurity scattering should be an inhomogeneous broadening term for PL FWHM in halide perovskites[177,184] and other semiconductors[185], which should show a weak temperature dependence. This is because impurities can lead to local electric field heterogeneity, and the existence and scattering of impurities are independent of the temperature. The PL FWHM will not change much with the temperature. However, experiments have shown a homogeneous broadening behavior of the PL FWHM of halide perovskites, with a strong temperature dependency[177,184]. Therefore, the contribution of impurity-induced emission broadening of the PL FWHM is considered to be minor in halide perovskites.

As we mentioned above, the temperature-dependent PL FWHM of halide perovskites shows a homogeneous behavior, which can be attributed to optical phonon and acoustic phonon scattering[177,184]. This is due to the fact that acoustic and optical phonons are strongly temperature-dependent. However, the contribution of the acoustic scattering Γ_{ac} in the emission broadening is also demonstrated to be minor in halide perovskites[184]. According to the expression equation of the acoustic scattering, Γ_{ac} is linearly proportional to the temperature[184]. However, the experimental temperature-dependent PL FWHM of halide perovskites, especially $FAPbI_3$, behave nonlinearly with temperature[184]. This is due to the fact that the polar Pb-I bond mainly generates optical phonons. Therefore, the contribution of the acoustic phonon scattering to the emission linewidth broadening is considered to be minor, and the optical phonon scattering is the dominating factor.

As demonstrated by extensive prior works[177,184,186,187], the above equation can be expressed in the following form, with the consideration that the acoustic phonon scattering and the impurity scattering contribute little to the emission linewidth in halide perovskites:

$$\Gamma(T) = \Gamma_{LO} + \Gamma_0 = \frac{\gamma_{LO}}{e^{(\frac{E_{LO}}{k_b T})} - 1} + \Gamma_0 \quad (9)$$

where γ_{LO} is the charged carrier-optical phonon coupling constant, E_{LO} is the energy of the optical phonon, and k_b is the Boltzmann constant. Based on this equation, we studied the relationship between PL FWHM and the temperature for the strained and the strain-free α-$FAPbI_3$ (Figure 28c and 28d). A clear redshift can be observed while the intensity of the emission peak increases with reducing the temperature due to the reduced scattering between the phonon and carriers at low temperatures. Figure 28e and 28f show the PL FWHM as a function of the temperature for a -2.4% strained and a strain-free sample, respectively. Data were fitted with the equation introduced above. Fitted results indicate the main increment of Γ_0 in the strained sample can be attributed to the increased scattering by the crystalline quality reduction. Meanwhile, the increment of both γ_{LO} and E_{LO} suggests an enhanced charged carrier-optical phonon coupling and higher phonon energy in the strained lattice, which can be attributed to the strain-induced lattice deformation[188]. Therefore, we can conclude that the PL FWHM difference of the strained and the strain-free sample mainly comes from the increased scattering by the strain-induced crystalline quality reduction.

To sum up, we discussed several possible mechanisms that might have led to the PL peak broadening and focused on the crystalline quality and charged carrier-optical phonon coupling. By analyzing the temperature-dependent PL FWHM of both strained and strain-free α-$FAPbI_3$, the

calculation results demonstrate that the PL broadening with strain is caused by the strain-induced crystalline quality reduction and enhanced optical phonon scattering.

Figure 28. PL peak broadening study by temperature-dependent PL measurements.
a, Strain-dependent PL FWHM. The results show that the FWHM of the PL peak increases with the strain. A bulk a-$FAPbI_3$ single crystal is used as the strain-free reference. **b**, Band diagram of the heterostructure. The analysis shows that the charged carrier transfer in the heterojunction can be excluded due to the straddling band alignment with a prohibited carrier transfer direction and a large energy barrier. Temperature-dependent PL of **c,** strained and **d**, strain-free α-$FAPbI_3$. Both samples exhibited uniform bandgap narrowing and FWHM narrowing with decreasing the temperature. Temperature-dependent PL FWHM of **e,** strained α-$FAPbI_3$ and **f,** strain-free α-$FAPbI_3$ with fitting. Results show that the strained α-$FAPbI_3$ has a higher Γ_0 and Γ_{LO} than that of strain-free α-$FAPbI_3$ due to the due to the strain-induced crystalline quality reduction and the strain-enhanced carrier-phonon scattering.

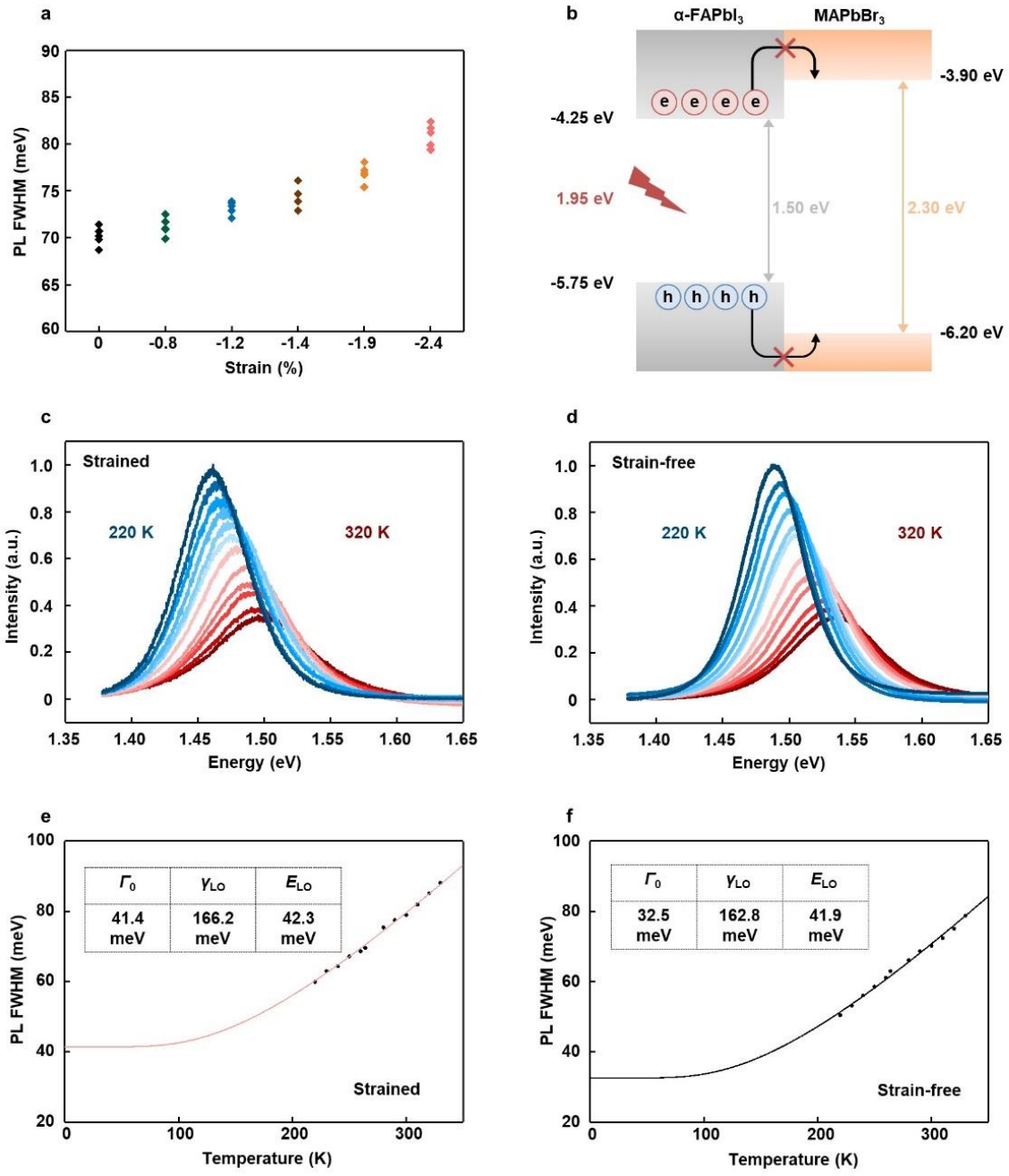
a
PL FWHM (meV)
Strain (%)
0
-0.8
-1.2
-1.4
-1.9
-2.4
b
α-FAPbI3
MAPbBr3
-3.90 eV
-4.25 eV
1.95 eV
1.50 eV
2.30 eV
-5.75 eV
-6.20 eV
c
Strained
220 K
320 K
Intensity (a.u.)
Energy (eV)
d
Strain-free
220 K
320 K
Intensity (a.u.)
Energy (eV)
e
Γ0
γLO
ELO
41.4 meV
166.2 meV
42.3 meV
PL FWHM (meV)
Strained
Temperature (K)
f
Γ0
γLO
ELO
32.5 meV
162.8 meV
41.9 meV
PL FWHM (meV)
Strain-free
Temperature (K)

Besides the crystalline quality measurements of the epitaxial thin films for the optical characterizations, we will also discuss the thin film crystalline quality for the electrical characterizations. The SCLC method is used to quantitatively evaluate the crystalline quality of the epitaxial thin film (Figure 29). Devices adopt the same structure as the one used in ToF measurement. Devices with different strain levels (strain-free, -0.8%, -1.4%, and -2.4%) are fabricated and tested. We note that bulk α-$FAPbI_3$ single crystals were used as the substrates to fabricate strain-free devices.

We first study the *I-V* characteristic curves of the devices with forward and reverse scans from 0.01 V to 2 V. Note that the devices adopt a planar structure to correlate with the devices used in the Hall effect measurements. A layer of Parylene-C (50 nm) and a layer of Au (50 nm) are sequentially deposited on the substrates while the lateral distance between two Parylene-C/Au electrodes is 100 μm. Epitaxially strained α-$FAPbI_3$ thin films are then grown from the gaps between the electrodes and cover part of the electrodes for electrical contact.

In the forward scan, the log-log *I-V* characteristic curves show different regions of behavior. At low voltages, the *I-V* curves exhibit a typical ohmic conduction behavior, where the current is linearly related to the applied voltage (n~1, blue line). In this region, the quantity of the thermally generated free carriers exceeds that of the externally injected carriers[83]. With increasing the applied voltage, the externally injected carriers gradually increase and start to fill the traps. Therefore, a trap-filling process is identified by the end of the linear ohmic region (n>3, green). By further increasing the voltage, traps in the bandgap are completely filled by the externally injected carriers, and the carriers move freely[189]. In this region, the current is squarely related to the applied voltage (n~2, orange). V_{TFL} is extracted by finding the voltage where the ohmic region ends. The extracted V_{TFL} in samples with different strains is used to evaluate the trap density.

The forward scan is followed by a reverse scan where the *I-V* characteristic curves of the reverse scan show only a linear region. By fitting the *I-V* curves of the reverse scan, we find out that the current is squarely related to the applied voltage (n~2, red). During the reverse scan, the filled traps will not undergo a de-trapping process because of the existence of the applied electric field as well as the continuously injected carriers. Therefore, the reverse scan cannot be used to study the trap-filling process, and the evaluation of the V_{TFL} can only be studied with the forward scan. Trap density of the epitaxial film can be calculated by:

$$V_{TFL} = {en_t d^2}/{2\varepsilon\varepsilon_0} \tag{10}$$

where d is the layer thickness, ε (=47) is the relative dielectric constant of α-$FAPbI_3$ and ε_0 is the vacuum permittivity.

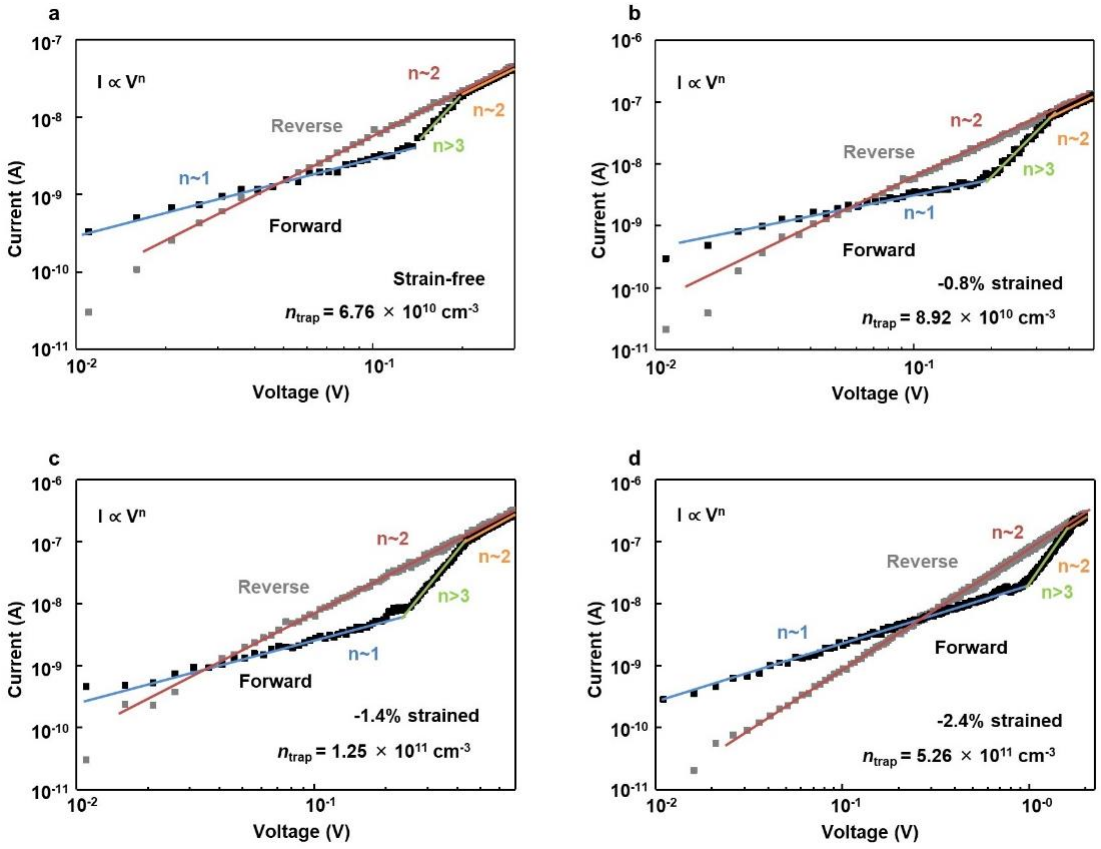

Figure 29. SCLC measurement of the epitaxial α-FAPbI$_3$ with different strains.
a to **d**, *I-V* characteristic curves for the SCLC measurement of the epitaxial α-FAPbI$_3$ film with a different strain. While the forward scans indicate a typical trap-filling process with increasing applied voltage, the reverse scan doesn't show a detrapping process.

We also statistically study the trap density in the epitaxial α-FAPbI$_3$ film with different strain magnitudes to evaluate the robustness of the measured trap density values. Here, five different devices of each strain value are tested. The trap densities of the epitaxial α-FAPbI$_3$ film from different samples are calculated and displayed in Figure 30a. The average trap densities and the standard deviation are shown in Figure 30b. With increasing the strain, the average trap densities show an increasing trend, indicating that a higher strain level induces a higher defect density in the epitaxial α-FAPbI$_3$ film. Meanwhile, the standard deviation of the trap density also increases with the strain, which reveals an increased disorder in the epitaxial α-FAPbI$_3$ film at higher strain values.

Besides, we also investigate *I-V* characteristic curves from the same device under different measurement conditions, e.g., different scan rates and scan directions. *I-V* curves of the halide perovskites are reported to be scan rate-dependent due to the fact that the scan rate can alter the charged carrier collection efficiency of the devices, which results in artificial *I-V* curves[169,170,190]. However, this discrepancy can be effectively minimized by adopting a relatively slow scan rate[168] since a fast scan rate has been reported to go beyond the response speed of free carriers to the electric field[191]. To prove that the 50 mV s^{-1} scan rate we use in this work does not produce artificial *I-V* curves, we study *I-V* curves under four representative scan rates (Figure 30c). *I-V* curves with 10 mV s^{-1}, 50 mV s^{-1}, and 200 mV s^{-1} scan rates show distinct trap filling behavior as we discussed above. The V_{TFL} extracted from the *I-V* curves with 10 mV s^{-1} and 50 mV s^{-1} scan rates are similar, indicating that 10 mV s^{-1} and 50 mV s^{-1} are sufficiently slow to avoid artificial *I-V* curves and V_{TFL} values. Meanwhile, increasing the scan rate to 200 mV s^{-1} leads to a smaller V_{TFL} because of the limited response of free carriers to the rapid electric field change. No trap filling process can even be measured when further increasing the scan rate to 1000 mV s^{-1}, showing that the *I-V* curve under a very fast scan rate can skew the results. Therefore, we can conclude that the 50 mV s^{-1} scan rate we use in the SCLC measurements helps produce reliable *I-V* curves and V_{TFL}. Besides, we study how the scan direction may possibly affect the SCLC measurement. Figure 30d shows *I-V* curves of the same device with different scan directions. The *I-V* curves from positive and negative scan directions, with ~10 min in between the scans, are similar to each other, which is because the device adopts a symmetric Au/perovskite/Au structure. The initial direction of the forward scan along either direction should give the same result. Therefore, we can conclude that the SCLC measurements under different scan conditions, with a slow scan rate (50 mV s^{-1}), and a symmetric device structure can produce reliable results.

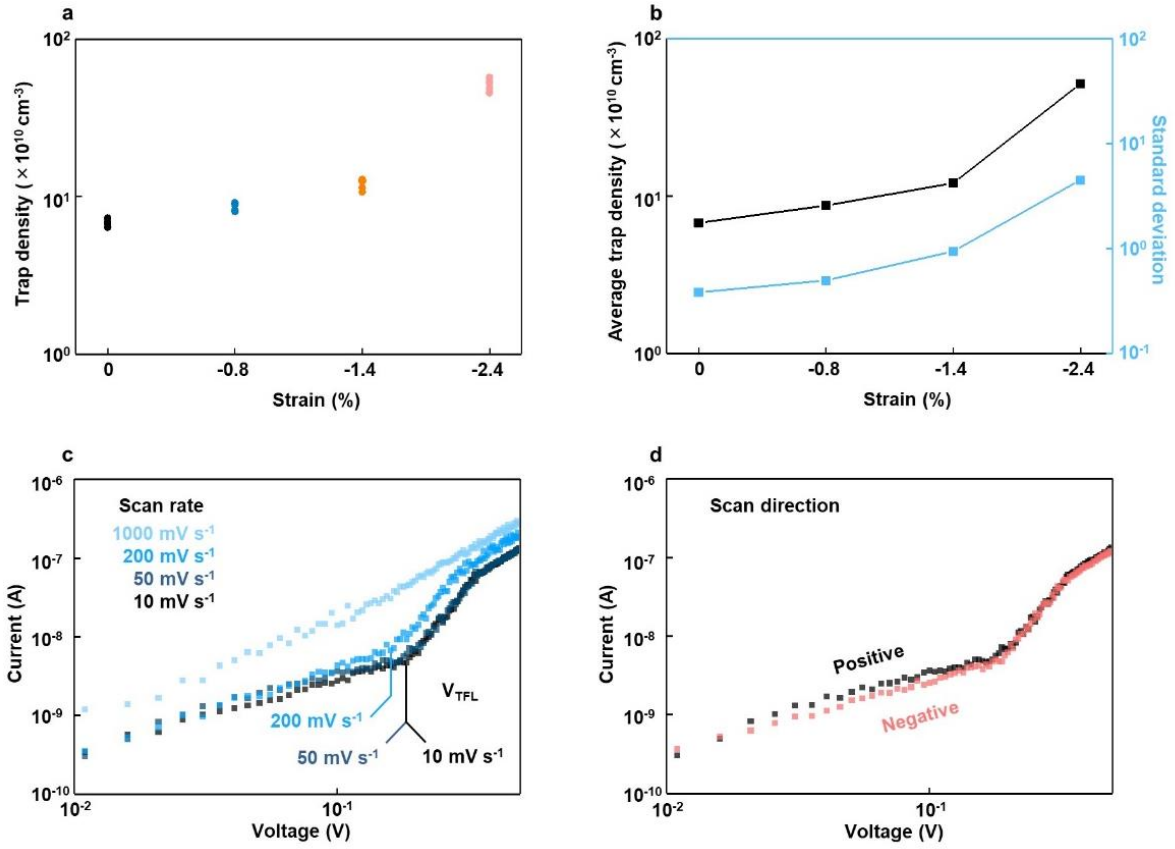

Figure 30. SCLC measurement condition study.
a, Strain-dependent trap density of the epitaxial α-$FAPbI_3$. Note the number of experiments $n = 5$ for each strain value. **b,** Statistics of the strain-dependent trap density. Results show that the average trap density will increase with increasing the strain, which can be attributed to the strain-induced defects. Meanwhile, the standard deviation of the trap density values also increases with the strain, indicating the increased disorder due to the higher defect density with the strain. **c**, Scan-rate-dependent *I-V* curves. *I-V* curves with 10 mV s^{-1} and 50 mV s^{-1} scan rates are similar, indicating that these scan rates are sufficiently slow to avoid artificial results. The *I-V* curve with 200 mV s^{-1} results in a smaller V_{TFL} because of the limited response of free carriers from the fast scan. Further increasing the scan rate to 1000 mV s^{-1} leads to the vanish of the trap-filling process. **d**, *I-V* curves with different scan directions of the same device. The high similarity of the two curves concludes that the scan direction will not affect the SCLC measurements due to the symmetric Au/Perovskite/Au device structure.

We note that the goal in this study is not to distinguish the origins or the densities of various traps but is to study the trap density increment in the epitaxial α-$FAPbI_3$ thin films when the strain magnitude is increased. For lattice-mismatched heteroepitaxial growth, the density of misfit dislocations will be increased with increasing the interfacial misfit magnitude and the epitaxial layer thickness, to partially release the strain[192]. These misfit dislocations tend to degrade the

properties of the epitaxial layers and, therefore, the performance of the devices by introducing below-gap trap states. For the impurity, the growth precursor was controlled to be the same, which will keep a similar impurity source for all α-$FAPbI_3$ films in this study. Without additional impurity source being introduced during epitaxial growth, the epitaxial film with different strain levels should share a similar impurity density. Therefore, we exclude the contribution of impurities to the measured trap density increment. For the other crystallographic defects (e.g., vacancies, interstitials, antisites, etc.), their contributions to the trap density increment are considered to be minor, because it is a convention that the generation of dislocations is the main reason for strain relaxation in heteroepitaxy[131,192]. For the interfacial defects formed at the perovskite/electrode interface, all device fabrication adopted the same protocol. Therefore, the interfacial traps caused by the interfacial defects are similar for different strain values and can be excluded from the possible reason for the trap density increment in the epitaxial samples. In this case, the impurities and the interfacial defects will not lead to the significant trap density increment, up to ~1000% as observed in the studies with increasing the strain magnitude from 0% to -2.4%.

Based on the above discussions, we demonstrate that the trap density increments with increasing the interfacial misfit magnitude and the film thickness can be attributed to the strain-induced dislocations. Even though there is currently a lack of an experimental characterization technique that would allow accurately quantifying the separate contribution of each defect due to the complexity of these defects[193], contributions from all other types of traps are minor and can be safely excluded in this study by adopting the unique variable principle throughout the experiment. Actually, the unique variable principal is commonly used to exclude irrelevant factors in trap density measurements, as evidenced by many examples in the literature. Vapor deposition of relatively thick perovskite film is reported to show reduced trap density due to the reduced

crystallographic defects. The trap density increment in the relatively thinner sample excludes the contribution of impurities and the interfacial defects because they are considered to be similar to those of the thicker sample and will not lead to trap density reduction[194]. Also, it is recently reported that the addition of CuBr into inorganic perovskite will reduce the trap density. The influence of the interfacial defects and the impurities are considered of minor influence to the trap density reduction in the control sample due to the same fabrication protocol[195]. Similarly, the addition of Eu^{3+}-Eu^{2+} ionic pair can reduce the crystallographic defects generated by the Pb^0 and I^0. The trap density increment in the control sample rules out the contribution of interfacial defects and impurities because the samples share similar fabrication processes[196]. Additionally, perovskite seeding growth is reported to improve the crystallinity and reduce the trap density. The interfacial defects and the impurities in the control sample are considered to be similar in the seeded grown sample and control sample[197]. What's more, modifying the interface between the perovskite and the electron transporting layer is shown to reduce interfacial defects and trap density. The influence of the impurities and crystallographic defects can be excluded because they are considered to be similar in different devices[198]. Finally, incorporating bilateral alkylamine additives is shown to reduce interfacial defects and trap density in the perovskite film. Contributions from impurities and crystallographic defects are ruled out due to the fact these two factors are similar in different devices[199]. We also investigate the literature to study the minimum trap density difference that can be measured by the SCLC method. Researchers demonstrated the reduced trap density by 15% due to the incorporation of Cl in the perovskite film[194]. In two-dimensional perovskite nanowires with different layer numbers, a one-fold increment of trap density was also reported[200]. Meanwhile, researchers demonstrated the decrease of trap density by ~20% with a modified ITO surface[201]. Similarly, a decrease of trap density by ~50% with a modified interface was also reported[202].

Compared with the reported works, the results demonstrate a difference from ~30% to up to ~1000%, which is sufficiently large to conclude that a higher strain can induce more defects.

Characterizing the trap density in halide perovskite thin films has been widely studied. Quantitative characterization of the trap density in halide perovskites are mostly done by the SCLC method (the dark *I*-*V* characteristic curve). It is believed to be the most facile, accurate, and direct technique for trap density characterization and has been extensively used[89,162,164]. Besides the SCLC method, tuning the excitation density of input photons in the transient photocurrent measurement is also reported to roughly estimate the trap density by generating different densities of free carriers and monitoring the decay rate[203,204]. The measurement accuracy is relatively low. Additionally, capacitance-frequency (*C*-ω) spectroscopy has been reported to study the trap density in organic materials[205,206] and halide perovskites[207-210]. The low-frequency capacitance originates from the carrier trapping/detrapping of electronic traps, while the high-frequency capacitance is attributed to the geometrical capacitance and the depletion capacitance[207,209].

In this study, we use the *C*-ω spectroscopy as an alternative probe for trap density of epitaxial α-$FAPbI_3$ thin films with different strain magnitudes. Devices for *C*-ω measurements have a lateral configuration with a 3 mm width. Au and ITO are used as the two electrodes with a 2×2 mm^2 area. During the measurement, a 0.5 V AC voltage is applied. The resulting electric field is 1.67×10^{-4} V μm^{-1}, which is insufficient for generating ion migration[210]. In this case, we exclude the contribution of charged ions to the measured capacitance. The capacitance of α-$FAPbI_3$ thin films with different strain magnitudes are measured in the frequency range of $1\sim10^5$ Hz in dark. To eliminate the influence of the parasitic capacitance from the substrate and air, we first measure the capacitance-frequency spectra of the bare substrate without the epitaxial layer. After measuring the capacitance-frequency spectra of the devices with the epitaxial layer, we subtract the spectra

of the substrates from that of the devices to obtain the capacitance-frequency spectra of the epitaxial layer, which therefore exclude the capacitance contributions from the substrates and air. The results after subtraction are shown in Figure 31a. The measured capacitance gradually increases with increasing the strain magnitudes, indicating the accumulation of electronic traps. We then calculate the trap density with the *C-ω* measurement results. The trap density can be calculated by:

$$N_t(E_\omega) = -\frac{V_b}{qkAtT}\frac{d\,C(\omega)}{d\,\ln(\omega)} \tag{11}$$

where N_t is the trap density at a certain trap energy E_ω, V_b is the build-in potential and is estimated to be ~0.5 V from the work function difference between Au and ITO, q is the element charge, k is the Boltzmann constant, A is the device area, t is the thickness, and T is the temperature. Trap energy E_ω is calculated by:

$$E_\omega = kT\ln\left(\frac{\omega_0}{\omega}\right) \tag{12}$$

where ω_0 is the attempt-to-escape frequency, which is reported to be ~2×10^{11} s^{-1} for halide perovskites[211]. The calculated trap density of the epitaxial α-$FAPbI_3$ thin films with different strain magnitudes are shown in Figure 31b, and an obvious trap density increment can be seen with increasing strain magnitudes. To quantitatively evaluate the trap density in the epitaxial thin films, we fit the calculated trap density distribution with the following Gaussian distribution equation:

$$N_t(E_\omega) = \frac{n_t}{\sigma\sqrt{2\pi}}\exp\left[-\frac{(E_0 - E_\omega)^2}{2\sigma^2}\right] \tag{13}$$

where n_t is the trap density, σ is the disorder parameter, and E_0 is the mean energy of the traps. The fitted trap density (n_t) for 0%, -0.8%, -1.4%, and -2.4% strained epitaxial thin films are 2.6×10^{11} cm^{-3}, 3.2×10^{11} cm^{-3}, 7.2×10^{11} cm^{-3}, and 2.4×10^{12} cm^{-3}, respectively. The trap density increment with increasing the strain magnitude indicates an accumulation of dislocations under a higher strain magnitude[192]. The trend also agrees with that measured by the SCLC method. We note that the *C-ω* method measures the sum of electron and hole traps[205] while the SCLC methods can distinguish electron and hole traps with selected electrodes[89]. In the SCLC measurements, we adopt an Au/perovskite/Au structure that only reveals the hole traps due to the energy alignment of the Au electrode for hole injection[89]. This may be the main reason that leads to the small discrepancy in the results measured by the *C-ω* and the SCLC methods.

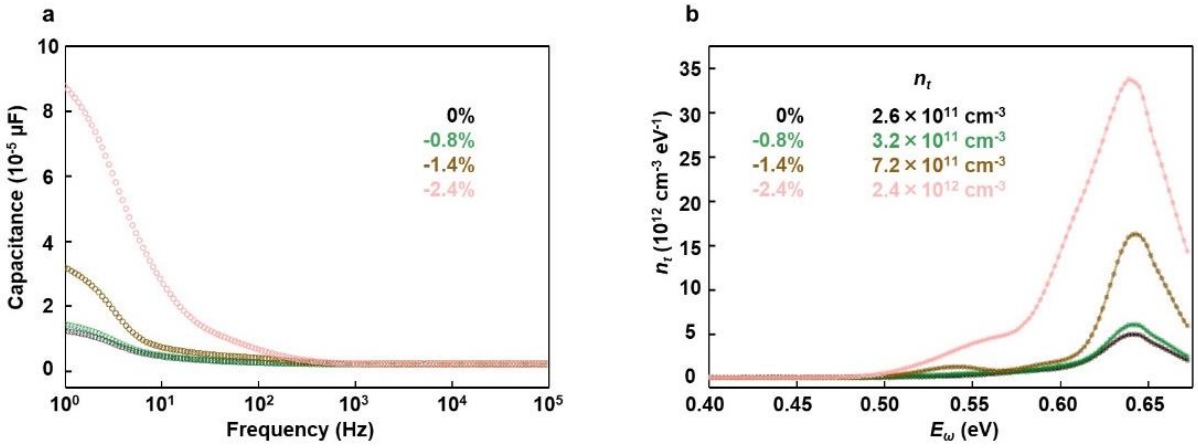

Figure 31. *C-ω* measurements of the epitaxial α-$FAPbI_3$ to evaluate the trap density.
a, *C-ω* spectra of the epitaxial α-$FAPbI_3$ thin films with different strain magnitudes. The low-frequency capacitance originates from the carrier trapping/detrapping processes. The larger capacitance at a higher strain magnitude suggests a higher density of traps. The high-frequency capacitance is attributed to the geometrical capacitance and the depletion capacitance. **b**, Trap density distribution extracted from the *C-ω* spectra. An obvious trap density increment is evident with increasing the strain magnitude. The fitted trap densities (n_t) by the Gaussian distribution equation indicate a higher trap density at a higher strain magnitude.

Considering that the strain-induced dislocations relax the epitaxial strain and reduce the crystalline quality of the epitaxial thin films for the electrical measurements, we carry out the

quantification of the strain relaxation in our strained perovskite thin film. Besides, metal halide perovskites are also considered as a class of soft materials where the strain can possibly be elastically relaxed. Therefore, we will study both the possible elastic strain relaxation due to the soft nature of halide perovskite and the plastic strain relaxation from the strain-induced dislocation.

To exclude the elastic relaxation in our epitaxial samples, we carry out FEA simulations. The simulation results are shown in Figure 32 where an α-$FAPbI_3$ thin film with a 30 μm × 30 μm × 3 μm dimension in l × w × t. Elastic constants C_{11}, C_{12}, and C_{44} of α-$FAPbI_3$ come from the reported literature[212]. Different biaxial compressive strains (-1.2% and -2.4%) are applied at the bottom of the α-$FAPbI_3$ to simulate the interfacial strain. Plastic relaxation from the dislocations is ignored in the simulation to focus on the influence of the elastic relaxation only. Figure 32a and 32b show the planar stress distribution from the bottom view of the -1.2% and -2.4% strained α-$FAPbI_3$, respectively. Figure 3.22c and 3.22d show the vertical stress distribution from the cross-sectional view of the -1.2% and -2.4% strained α-$FAPbI_3$, respectively. Simulated results indicate a uniform strain distribution throughout the entire epitaxial α-$FAPbI_3$ thin film. We further study the thickness-dependent stress distribution along the vertical direction (Figure 32 e and 32 f), as labeled by the blue line and the red line in Figure 32c and 32d, respectively. From the results, the strain maintains almost the same along with the thickness. For a sample thickness of 3 μm, the elastic relaxation is calculated to be 0.096% and 0.093% for -1.2% and -2.4% strained α-$FAPbI_3$, respectively. The small discrepancy between the elastic relaxation under the two strain magnitudes is due to the numerical dispersive error because the FEA simulation uses a dispersive model for approximation[213]. Therefore, the elastic relaxation in the epitaxially strained α-$FAPbI_3$ is not as prominent as we expected, due to the small thickness (in the range of hundreds of nanometers to a

few micrometers) used in this study. Halide perovskites are in fact still brittle solids even though they are softer in nature than other conventional semiconductors[214].

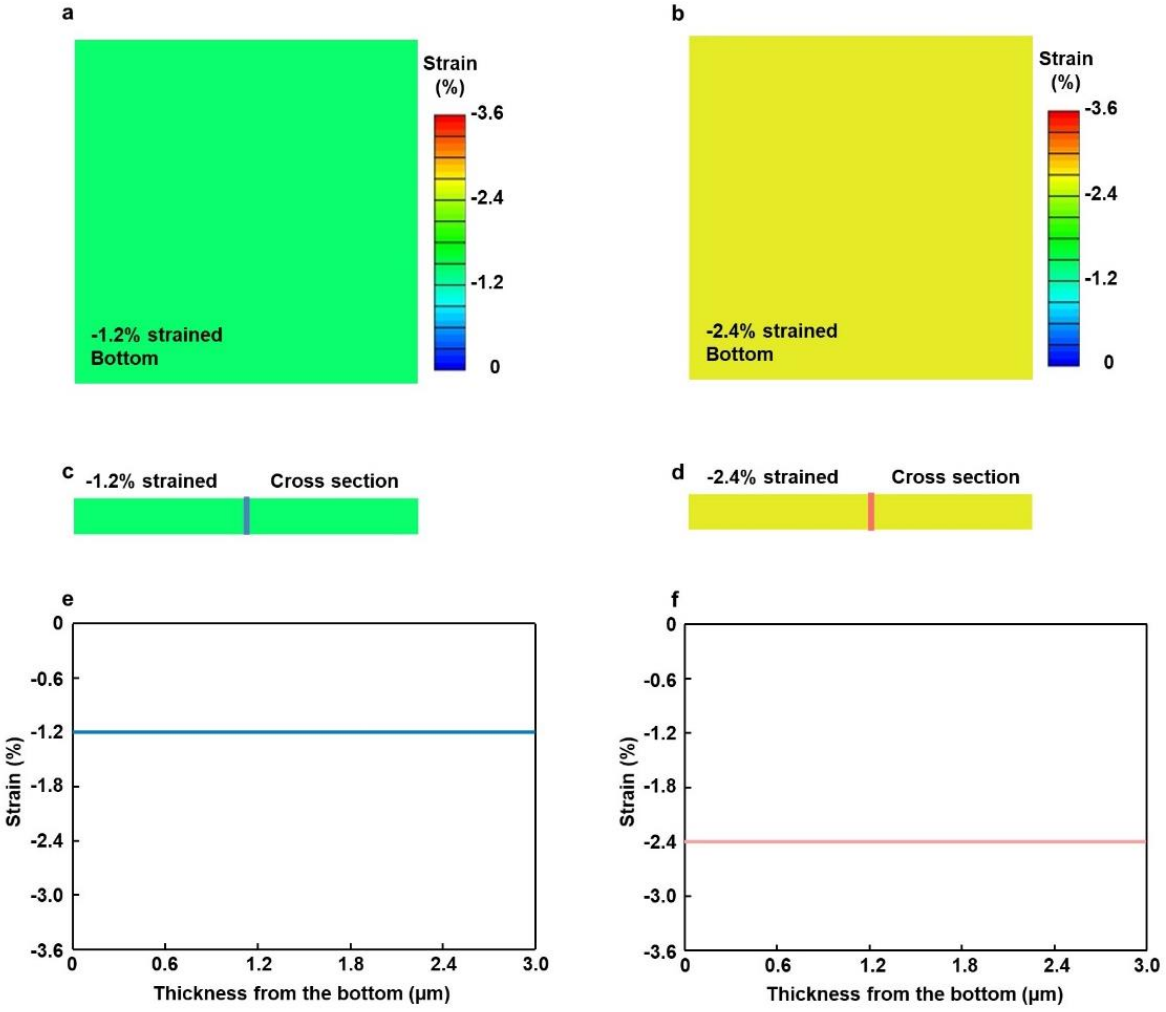

Figure 32. Elastic strain relaxation study of the epitaxial α-FAPbI$_3$ thin films.
Planar strain distribution of the α-FAPbI$_3$ with **a,** -1.2% and **b,** -2,4% strain. Vertical strain distribution of the α-FAPbI$_3$ with **c,** -1.2% and **d,** -2,4% strain. Results show uniform strain distribution in both α-FAPbI$_3$ thin films. Thickness-dependent strain distribution of the α-FAPbI$_3$ with **e,** -1.2% and **f,** -2,4% strain. Colors are correlated with the lines in **c** and **d**. Results indicate that the elastic strain relaxations in both α-FAPbI$_3$ thin films are 0.096% and 0.093%, respectively.

In heteroepitaxial growth, strain usually relaxes plastically rather than elastically. The calculations of the critical thickness where the dislocations form and relax the strain have been determined theoretically and experimentally. There are two models that have been widely used for the critical thickness calculations: the Matthews and Blakeslee (MB) model[215] and the People and

Bean (PB) model[216]. The MB model is a mechanical equilibrium model that stems from the force balance of dislocations. In this model, the critical thickness is defined as the thickness when the strain force is equal to the dislocation tension force and can be expressed as:

$$h_c = \frac{b(1 - v\cos^2\alpha)}{8\pi f(1+v)\cos\lambda}\left[1 + \ln\left(\frac{h_c}{b}\right)\right] \tag{14}$$

where is h_c the critical thickness, b is the length of Burger's vector, v is the Poisson's ratio, α is the angle between the Burger's vector and the line vector for the dislocation, f is the misfit strain, and λ is the angle between the Burger's vector and the line in the interface plane that is perpendicular to the intersection of the glide plane with the interface. The PB model is an alternative prediction method based on the energy equilibrium that is widely studied and experimentally proved. In this model, the critical thickness is defined as the thickness where the strain energy is equal to the dislocation formation energy and can be expressed as:

$$h_c = \frac{(1-v)b^2}{(1+v)\left(16\sqrt{2}\pi a f^2\right)}\ln\left(\frac{h_c}{b}\right) \tag{15}$$

where a is the lattice constant of the material. Many studies show a large discrepancy with the MB model. Even the epilayer is thicker than the MB limit, the dislocations are still absent[217]. Therefore, the MB model underestimates the critical thickness. The MB model may not give a quantitatively matched result. Besides, α and λ in PB need to be determined for different dislocations. However, the PB model gives a closer estimation of the critical thickness[217], and will, therefore, be used in this study.

We first study the thickness-dependent strain relaxation of the epitaxial α-$FAPbI_3$ thin films with different strain by in-plane XRD. In-plane XRD measures the in-plane lattice constant of the crystalline materials, which can be directly used to calculate the strain and contains information about the plastic strain relaxation in heteroepitaxy. Figure. 33a and 33b show the thickness-dependent in-plane XRD patterns of two representative epitaxially strained α-$FAPbI_3$ thin films with -1.2% and -2.4% strain, respectively. The -1.2% strained epitaxial α-$FAPbI_3$ thin film with a thickness of 200 nm shows obvious plastic strain relaxation, as evidenced by the peak shifting (to a lower angle, the vertical line labels the fully strained peak position) and broadening. For the -2.4% strained epitaxial α-$FAPbI_3$ thin films, plastic relaxation can be measured in films above 50 nm with obvious peak shifting and broadening. The vertical line labels the fully strained peak position. Besides, we can also obtain the thickness-dependent in-plane lattice constants, based on which we can calculate the in-plane strain by comparing with the in-plane lattice constant. The degree of plastic strain relaxation can be quantified by comparing the local in-plane strain with the highest measured in-plane strain. Quantification of the degree of plastic strain relaxation is done by calculating the relaxation constant R:

$$R = \frac{a_{measured} - a_{strained}}{a_{\alpha-FAPbI_3} - a_{strained}} \tag{16}$$

where $a_{measured}$ is the measured in-plane lattice constant at different thicknesses, $a_{strained}$ is the in-plane lattice constant with maximum strain, and $a_{\alpha-FAPbI_3}$ is the lattice constant of the strain-free α-$FAPbI_3$. For the epitaxial film with the same substrate but different thicknesses, R ($0 \leq R \leq 1$) reveals the relationship between the film thickness and the degree of plastic strain relaxation. For R equals to one, the epitaxial film is considered as fully-relaxed. Otherwise, the film is considered as partially-relaxed. At relatively low thickness, R remains at zero without any

relaxation. With increasing thickness, R will gradually increase due to the formation of dislocations, which plastically relax their surrounding strain.

The thickness-dependent relaxation constants of each epitaxial α-$FAPbI_3$ with different substrates (i.e., different strain) are calculated and shown in Figure. 33c. The error bars label the range of calculated R of the films with the same substrate and thickness. Results show that the film with a -2.4% strain quickly relaxes at the thickness of ~50 nm while the film with -0.8% starts to relax at ~200 nm. Note that the thinnest film we can obtain is ~50 nm, and we assume that the monolayer α-$FAPbI_3$ will be fully strained without relaxation. Critical thicknesses are extracted from Figure. 33c where R is larger than 0 and fitted with both the MB and PB models (Figure. 33d). Results show that the critical thickness decreases with the increasing strain. Our experimental results agree more with the predicted PB model, indicating that the plastic strain relaxation due to the dislocations generated during the epitaxial growth is the dominating relaxation mechanism.

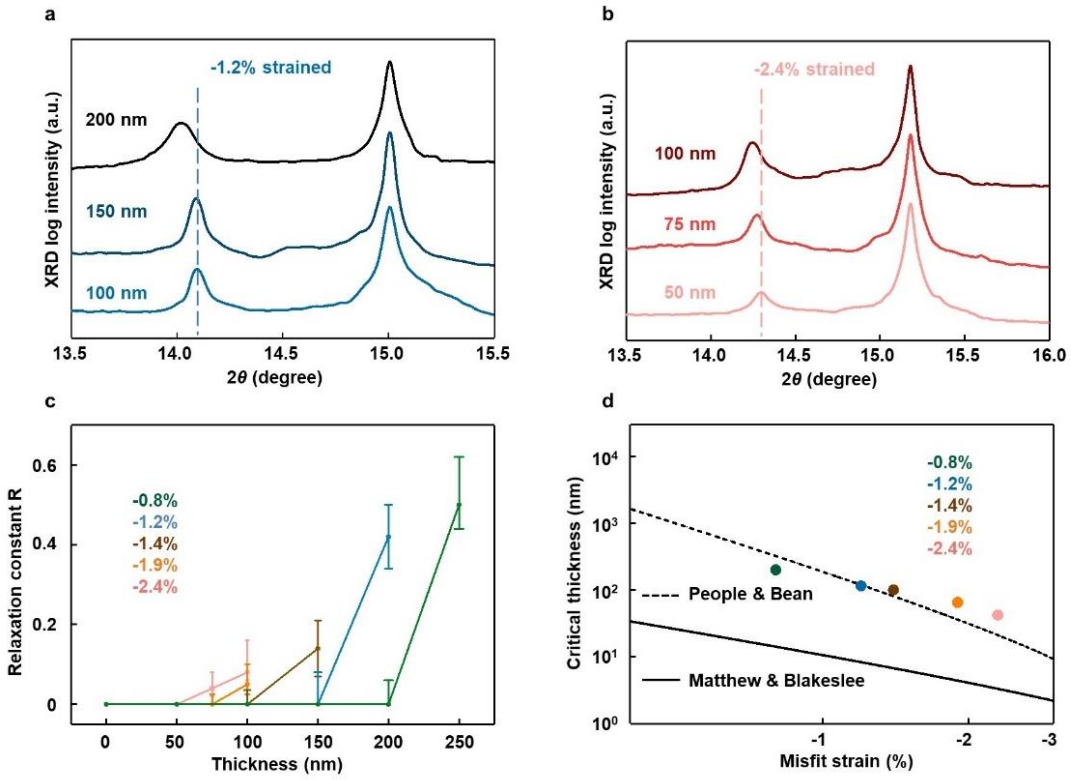

Figure 33. Plastic strain relaxation study of the epitaxial α-FAPbI$_3$ thin films. Thickness-dependent in-plane XRD of **a**, -1.2% strained and **b**, -2.4% strained α-FAPbI$_3$ thin films. Vertical lines label the peak position of the fully strained films. Plastic strain relaxation at relatively high thickness can be evident by the peak shifting to lower angle and peak broadening. **c**, Thickness-dependent relaxation constant R of the epitaxial α-FAPbI$_3$ thin films with different strains. Results show that the critical thickness decreases with increasing the strain. **d**, Fitting of the experimental critical thicknesses with the MB and PB models. Experimental results agree well with the PB model, indicating that the plastic strain relaxation due to the dislocations generated during the epitaxial growth is the dominating relaxation mechanism.

In summary, we exclude elastic relaxation although halide perovskites are much softer than conventional semiconductors[214]. Our FEA simulation results show the elastic relaxation for a 3 μm thick α-FAPbI$_3$ thin film is negligible, only ~0.09%. Thickness-dependent in-plane XRD is used to study the critical thickness at which the strain will start to be plastically relaxed. The results show that the critical thickness is much less than the thickness we used in this study and, therefore, the relaxation can be attributed to the plastic relaxation by forming dislocations.

We also find that the crystalline quality of the substrate is found to have a significant impact on the quality of the epitaxial thin film since defects in the substrates will propagate through the epitaxial layer and relax the strain. The substrate crystal quality prepared using the ITC[218] (Figure 34a) and the Slow Solvent Evaporation (SSE) methods (Figure 34b to 34f) are systematically characterized. The FWHM value in rocking curve measurements characterizes crystal mosaicity. Substrates grown by the SSE method show a much smaller FWHM value (~0.020°) compared with those by the ITC method (~0.084°) due to the extremely slow crystallization speed of SSE, indicating a higher crystal quality of substrates prepared by the SSE than those by the ITC. Figure 34g shows (001) XRD patterns of epitaxial α-$FAPbI_3$ grown on substrates with high quality (red curve) and low quality (black curve). For α-$FAPbI_3$ grown on the high-quality substrate, the FWHM of the XRD peak is also smaller than α-$FAPbI_3$ grown on the low-quality substrate. Additionally, the epitaxial α-$FAPbI_3$ grown on the high-quality substrate maintains the strained status with a shifted diffraction peak while the epitaxial α-$FAPbI_3$ grown on the low-quality substrate has a (001) peak close to that of the strain-free sample at 13.92° (position of the dashed line).

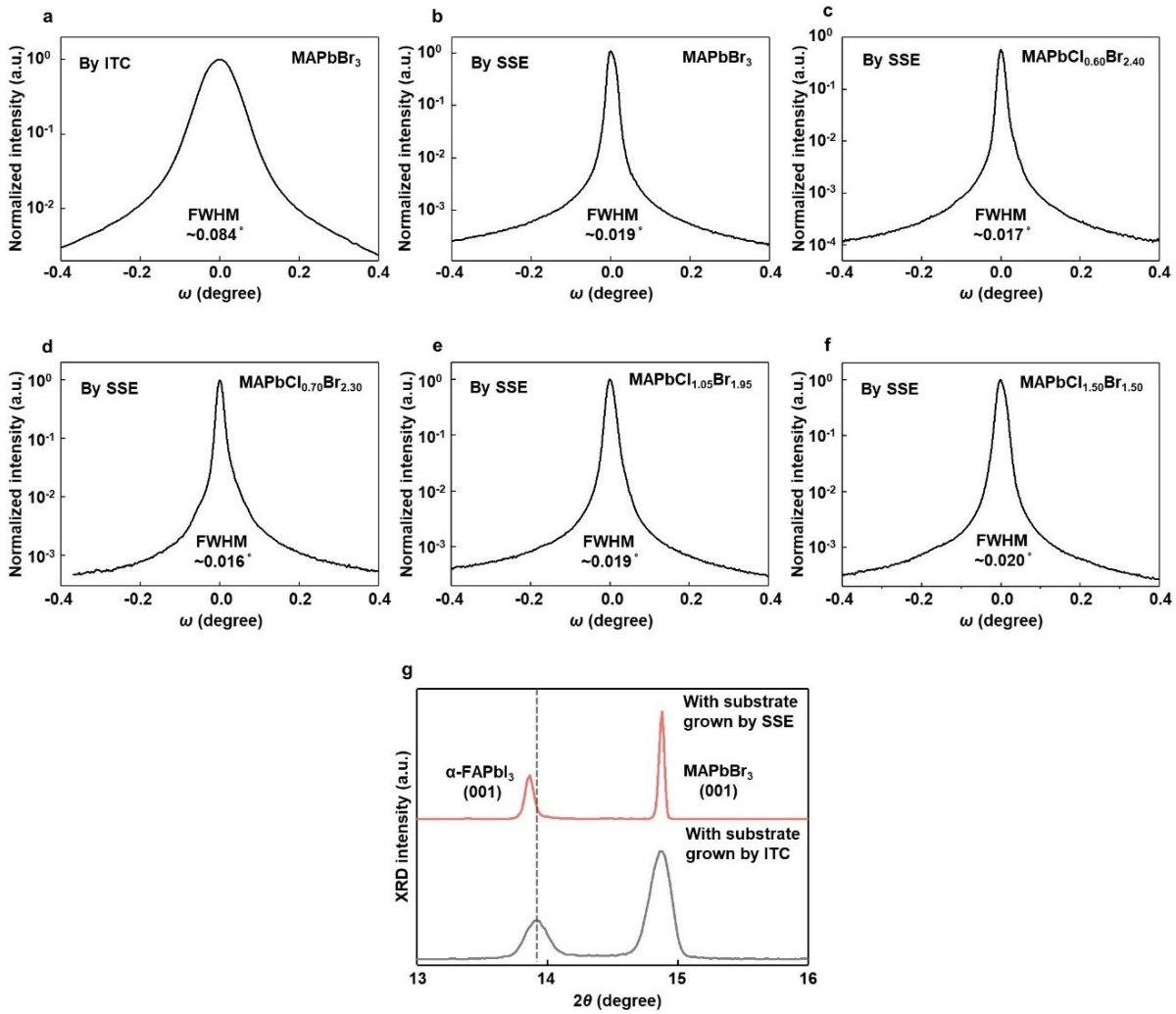

Figure 34. Characterization of substrate quality with different growth methods and its impact on the epitaxial strain.

a to **f**, Rocking curve measurements of substrates grown by the ITC and SSE methods. Lower FWHM values by the SSE indicates better crystal quality. **g**, XRD patterns of strained α-$FAPbI_3$ on a substrate with higher crystal quality (red curve) and relaxed α-$FAPbI_3$ on a substrate with lower crystal quality (gray curve). Dislocations in the substrates can propagate into and relax the strain in the epitaxial α-$FAPbI_3$. The vertical dash line labels the (001) peak position of strain-free α-$FAPbI_3$. The peak position from the strain-relaxed $FAPbI_3$ (gray curve) shifts back to that of strain-free α-$FAPbI_3$.

3.8 High-performance Photodetector Based on the Strained α-$FAPbI_3$

High-performance photodetectors are demonstrated as a use case of the strain engineered α-$FAPbI_3$ thin films. Based on the device structure and working principles, the halide perovskites

photodetectors are divided into two main categories: the photoconductor-type and photodiode-type. Compared with the photodiode-type one, the photoconductor-type photodetectors will have a much higher responsivity, and the EQE will be larger than 100% due to the injected carriers[5,58,219]. Here, we fabricate photodetectors with both structures and discuss them below. Photodetectors with a vertical photoconductor structure based on the strained α-$FAPbI_3$ thin films are fabricated with a structure shown in Figure 35.

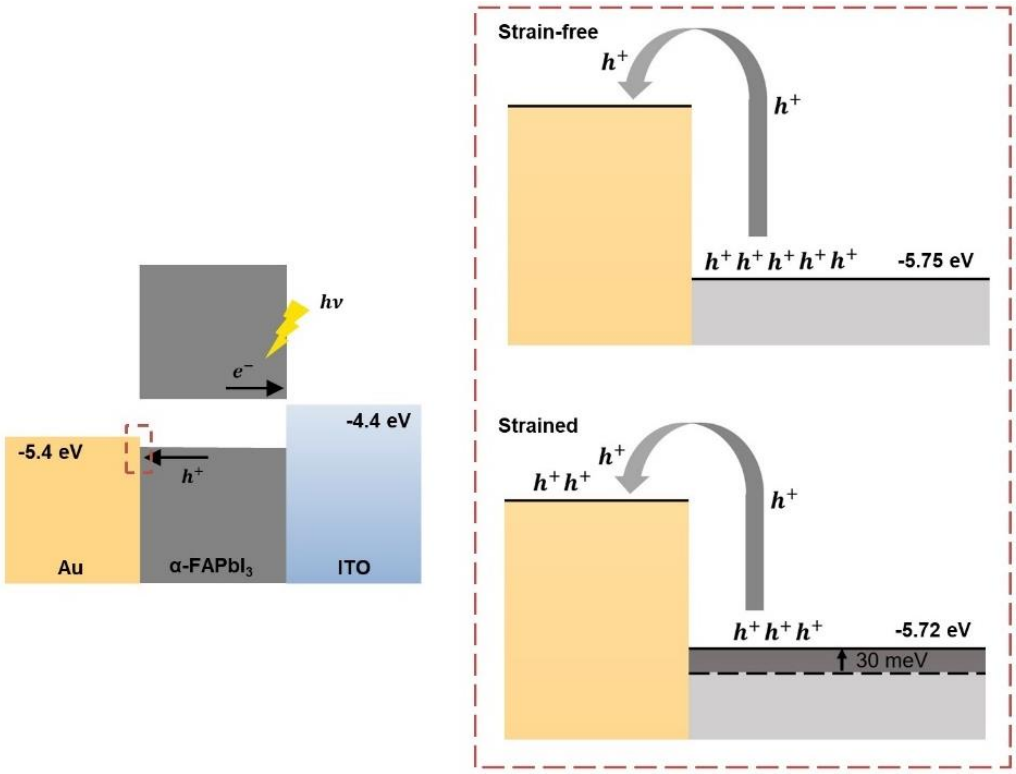

Figure 35. Schematic band diagrams of photodetectors.
Left panel is the flat band diagram of the photodetector. Due to the compressive strain, the VBM of α-$FAPbI_3$ at the interface will be pushed up and align better with the Au Fermi level (-5.4 eV), which allows better hole transfer from α-$FAPbI_3$ to Au and therefore enhances the device performance.

Figure 36a shows the *I-V* characteristics of a strain-free device and a device under -1.2% strain. The dark current at -1 V of the strained device is ~15% higher than that of the strain-free one, indicating its higher defect density of the strained device. However, the photocurrent of the strained device shows a ~180% increase compared to the strain-free one. We attribute the

photocurrent enhancement to the higher carrier mobility and the better alignment of VBM to the Au Fermi level under compressive strain (Figure 35). Responsivity of the two photodetectors, defined as the change in photocurrent per unit illumination intensity, is measured at various illumination intensities (Figure 36b). The responsivity of the strained device, with a maximum of 1.3×10^{6} A W^{-1} at an incident power density of 1.1×10^{-7} W cm^{-2}, is almost twice of that of the strain-free device. This is again attributed to the enhanced carrier mobility and the better band alignment of the strained device. We note that the responsivity of the photodetectors, defined as the change in photocurrent per unit illumination intensity, is calculated by:

$$R = \left(J_{light} - J_{dark}\right)/P \tag{17}$$

where J_{light} and J_{dark} are the current densities under illumination and dark conditions, respectively, and P is the input light power density. The strained device shows a much-enhanced external quantum efficiency (EQE) over the visible range (Figure 36c) due to the enhanced carrier mobility as well as better carrier transport across the Au/perovskite interface. The rise and fall times of the strained device are ~30% shorter than those of the strain-free device, indicating an improvement in carrier dynamics (Figure 36d). All devices we tested have a thickness of around 1 μm. A transparent indium tin oxide electrode is deposited as the top electrode with an area of 1×1 mm^{2}. *I-V* characteristics are measured under -1 V bias with a 685 nm laser as the excitation source under various illumination intensities.

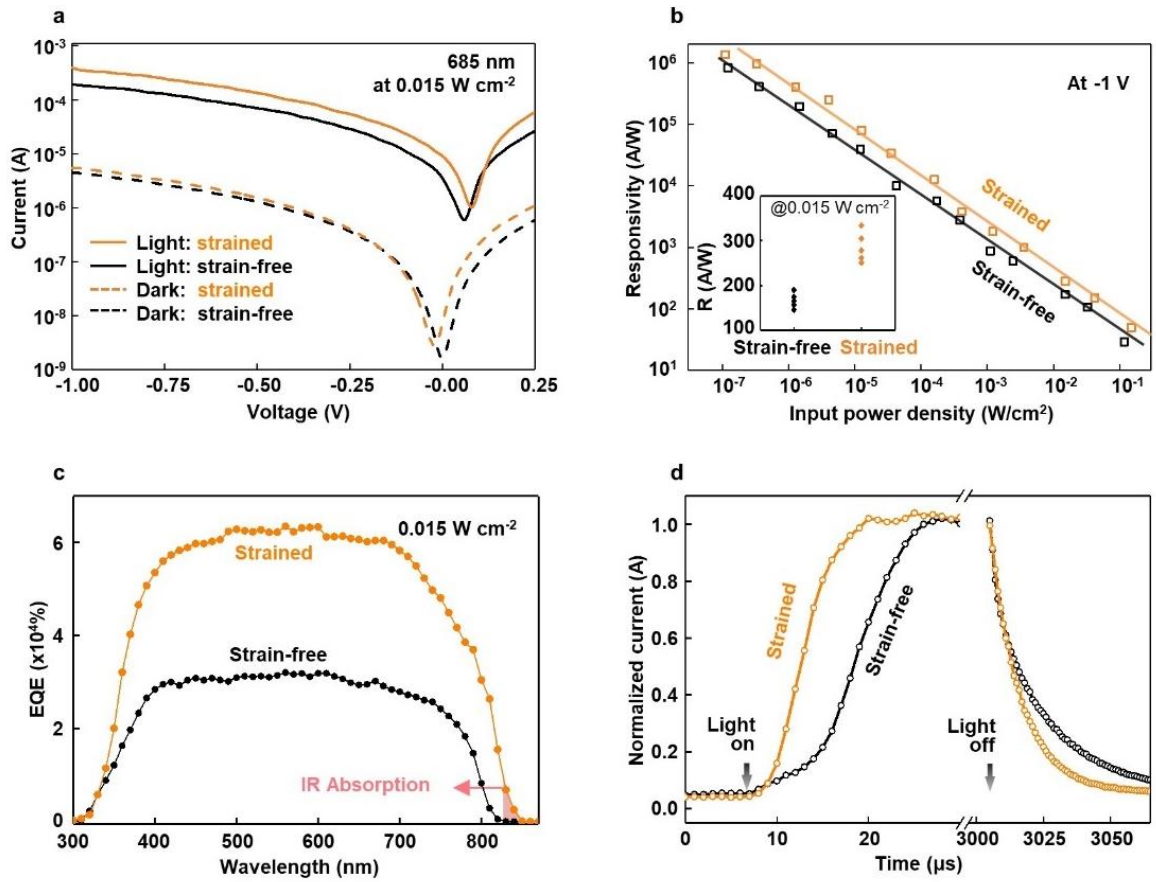

Figure 36. Photoconductor-type photodetector characterizations based on the -1.2% strained α-FAPbI$_3$ thin film (1).
a, *I-V* characteristics of Au/α-FAPbI$_3$/indium tin oxide (ITO) photoconductor structured photodetectors. The dark current and photocurrent of the strained detector are ~15% and ~180% higher than those of its strain-free counterpart. Detectors are tested with a 685 nm laser under 1 μW. **b**, Comparison of responsivity of the strained and strain-free photodetectors. The responsivity of both devices shows an increasing trend with decreasing incident power, as chances of carrier recombination go down at low illumination intensities[66]. The strained device yields a higher responsivity due to higher carrier mobility and better band alignment. The inset plot is the statistical average of the detector performance. **c**, EQE spectra of the strained and strain-free photodetectors showing that the strained photodetector yields a higher EQE as well as a broader absorption spectrum due to enhanced carrier mobility and bandgap reduction. **d**, Response times of the photodetectors, with faster rise and fall times for the strained (9 μs and 34 μs) than the strain-free (14 μs and 50 μs) device due to the enhanced carrier mobility and transport.

Figure 37a shows the responsivity of photodetectors at different strain levels under 0.015 W/cm^2 illumination. Compared with the strain-free device, devices at -0.8%, -1.2% and -1.4% strain levels show enhanced responsivity. Further increasing the compressive strain level will lead to a deterioration of the responsivity due to the accumulation of defects. Table 3 summarizes the

highest responsivity measured on α-$FAPbI_3$ in the literature. The responsivity of the device is comparable with the highest responsivity of a strain-free system with a similar device structure but at a much weaker illumination and higher bias voltage.

Table 3. Summary of representative halide perovskite photodetectors with high responsivities in the literature.

Device structure	Structure	Highest R	Light power	Bias	References
Au/$MAPbBr_3$/Au	Planar	~10 A W^{-1}	0.01 mW cm^{-2}	-2 V	[220]
Cr/$MAPbI_3$/Cr	Planar	~20 A W^{-1}	0.1 mW cm^{-2}	-1 V	[221]
Au/$MAPbI_3$/Au	Planar	~20.4 A W^{-1}	2 μW cm^{-2}	-1.5 V	[222]
Au/$MAPbBr_3$/Au	Planar	40 A W^{-1}	54 μW	-5 V	[223]
Au/ $(BA)_2(MA)_{n-1}Pb_nI_{3n+1}$ NWs/Au	Planar	2×10^4 A W^{-1}	10^{-6} mW cm^{-2}	-2 V	[200]
Au/$FAPbI_3$/ITO	Vertical	1.3×10^6 A W^{-1}	1.1×10^{-7} W cm^{-2}	-1 V	This Work

Besides, the detectivity, which characterizes how weak light can be detected, and the gain, which describes the number of charges flowing through an external circuit per incident photon, are calculated by:

$$D = {R}/{\sqrt{2qJ_d}} \tag{18}$$

$$G = {1240R}/{685} \tag{19}$$

where D is the detectivity, R is the responsivity, q is element charge, J_d is the dark current density, and G is the gain. They are also plotted as a function of illumination power level for both -1.2% strained and strain-free devices (Figure 37b and 37c). Results demonstrate that the strained device has better performance than the strain-free device. Additionally, after normalizing the EQE spectra, a distinct response in the short-wave infrared region can be identified for the strained device

(Figure 37d), consistent with the PL measurements showing bandgap reduction under compressive strain.

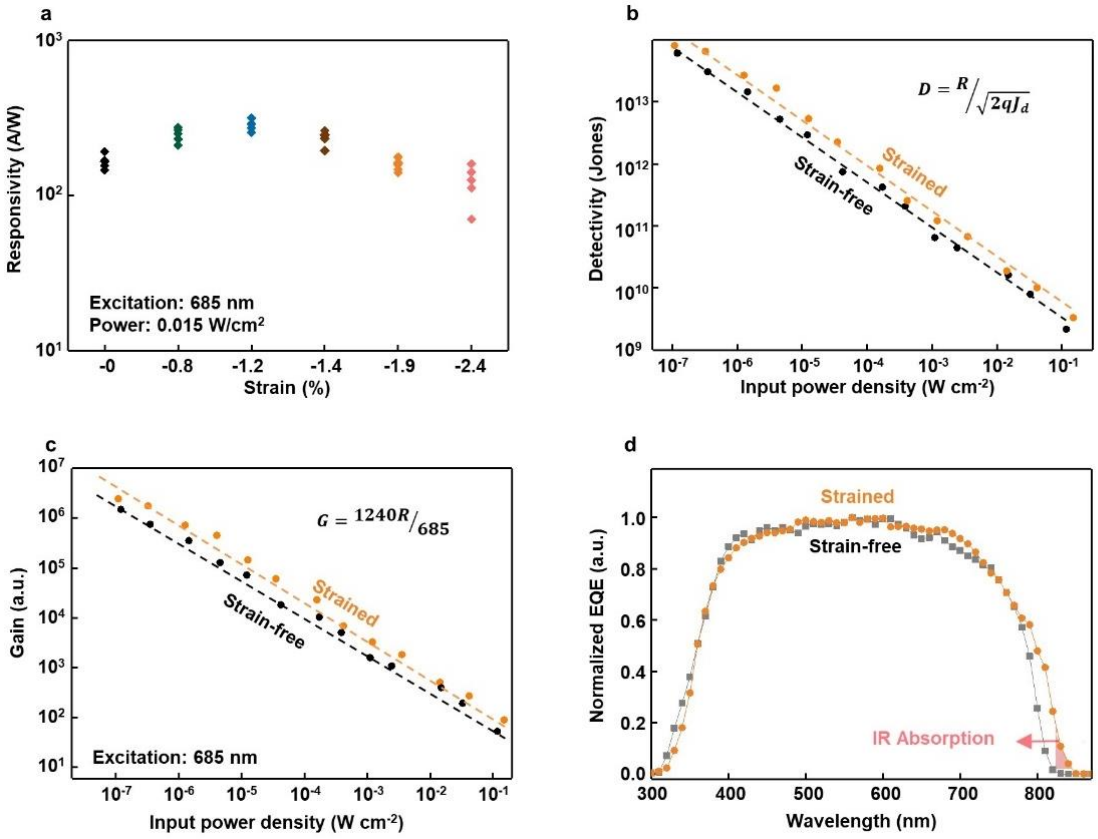

Figure 37. Photoconductor-type photodetector characterizations based on the -1.2% strained α-FAPbI$_3$ thin film (2).
a, Responsivity as a function of strain level in α-FAPbI$_3$. Devices under -0.8 %, -1.2 % and -1.4 % compressive strain give better responsivity compared to the strain-free device. Further increasing the compressive strain can lead to a higher density of dislocations, which reduces the responsivity. **b**, Detectivity, and **c**, Gain of the photodetector based on α-FAPbI$_3$ under -1.2% strain indicating enhanced performance. **d**, Normalized EQE of the photodetector based on α-FAPbI$_3$ under -1.2% strain, showing an extended absorption range.

Compared with the photoconductor-type photodetectors, the photodiode-type photodetectors exhibit a minimized dark current by blocking the external current injection with the electrons/holes blocking layers. In this study, we aim at fabricating a detector with high responsivity. Therefore, we fabricate and test the photodetector with the photodiode structure for comparison. We fabricated a photodiode-type photodetector by inserting PEDOT: PSS as the hole

transporting layer and tin dioxide (SnO_2) as the electron transporting layer. The structure of the photodiode type photodetector is Au/PEDOT: PSS/$FAPbI_3$/SnO_2/ITO, which is shown in Figure 38a. From the band diagram, the carrier injection under reverse bias is blocked due to the large energy barrier. The characterization of the photodetector was carried out with a 685 nm red laser, which is selected based on the highest EQE wavelength, under different input power levels. Figure 38b shows the *I-V* curves of the photodetector under the dark condition as well as under 1 μW illumination. The *I-V* curves show a typical diode-like behavior while the dark current under -0.5 V is measured to be ~ $2x10^{-8}$ A. This value is more than two orders of magnitude lower than that of the photoconductor type detector, as the reviewer pointed out. However, under the same illumination power level, the photocurrent is much smaller than that of the photoconductor type detector (~600 times lower at a 10^{-6} W incident power), therefore, leads to a lower responsivity (~500 times lower at a 10^{-6} W incident power). The responsivity and the photocurrent under different illumination power levels are also shown in Figure 38c. Under different illumination power levels, the responsivity of the photodetector is always lower than 1 A W^{-1} (in comparison with the responsivity of 200 A W^{-1} of the photoconductor type detector), indicating the block of external current injection with the presence of the different transporting layers.

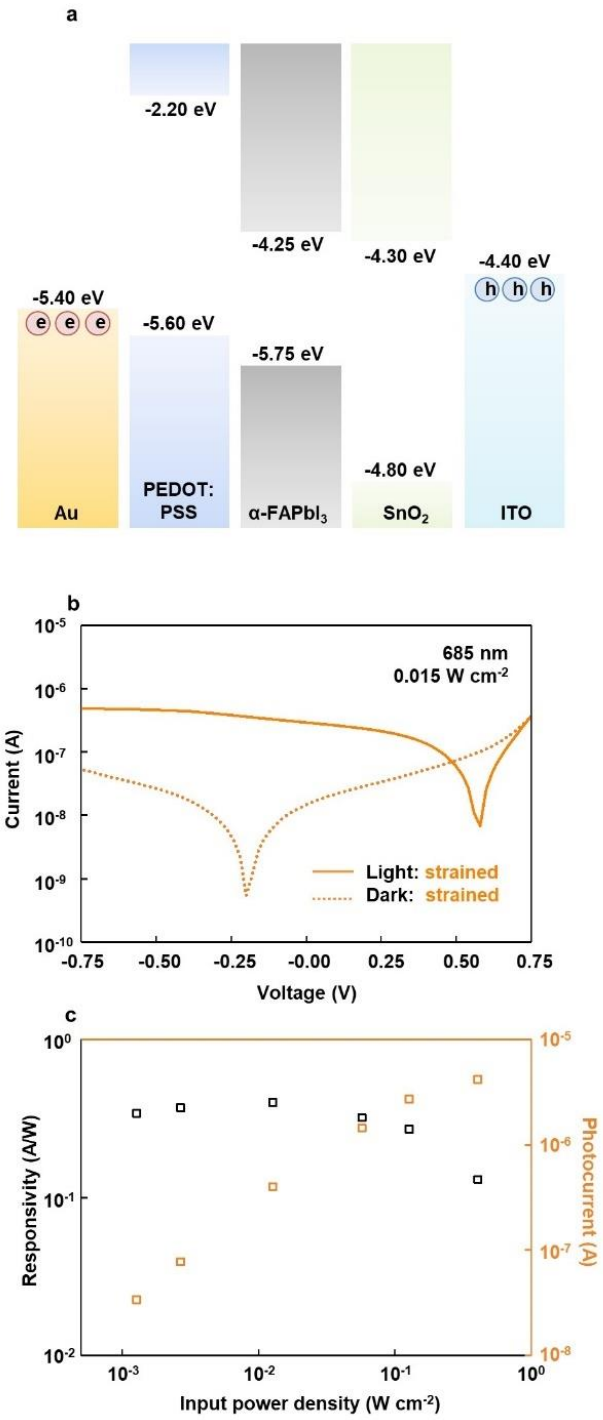

Figure 38. Photodiode-type photodetector characterizations.
a, The band diagram of the photodetector. An Au/PEDOT:PSS/α-$FAPbI_3$/SnO_2/ITO structure is used to build a photodiode. In this structure, the injection of external carriers under reverse bias is efficiently blocked due to the large energy barrier. **b,** *I-V* curves the photodetector. The dark current is reduced to ~10^{-8} A due to the diode structure. **c,** Responsivity and photocurrent of the photodetector under different illumination power levels. Results show that the responsivity is lower than 1 with the diode structure.

3.9 Conclusion

The technique we developed enables the controllable strain engineering of halide perovskites with epitaxial growth, which has a fundamental difference from the previous works. Structural characterizations reveal the tetragonality increment with the increasing compressive strain. Optical characterizations show a bandgap reduction and a VBM lifting with the increasing compressive strain. Meanwhile, the hole mobility is also found to increase with strain. The relaxation mechanism is systematically studied, and a high-performance photodetector is demonstrated. The epitaxial system we developed is a generalized approach that can presumably be applied to the entire halide perovskites family.

Chapter Three, in part, is a reprint of the material 'Strain Engineering and Epitaxial Stabilization of Halide Perovskites', Chen, Y., Lei, Y., Li, Y., Yu, Y., Cai, J., Chiu, M., Rao, R., Gu, Y., Wang, C., Choi, W., Hu, H., Wang, C., Li, Y., Song, J., Zhang, J., Qi, B., Lin, M., Zhang, Z., Islam, A., Maruyama, B., Dayeh, S., Li, L., Yang, K., Lo, Y., Xu, S., Nature, 2020, 577, 209. The dissertation author was the primary investigator and first author of this paper.

Chapter 4. Enhanced Structural Stability of Metal Halide Perovskites By Epitaxial Stabilization

4.1 Motivation for Enhancing the Structural Stability of Metal Halide Perovskites

As the first demonstrated perovskite material for photovoltaic applications in the broad metal halide perovskite family, $MAPbI_3$ is considered as the most widely studied metal halide perovskites and have received wide attention. In recent years, researchers also look into perovskites with different compositions to further enhance the performance and improve the stability (operation lifetime) of the devices. α-$FAPbI_3$, under such concerns, is seen as an alternative to replace conventional $MAPbI_3$. Due to the smaller bandgap compared with that of $MAPbI_3$, α-$FAPbI_3$ exhibits a better potential in photovoltaic applications. Solar cells based on α-$FAPbI_3$ has a much larger short-circuit current and, therefore, a higher power conversion efficiency. To date, α-$FAPbI_3$-based solar cells reached a certified 25.2% efficiency in 2019, which is much higher than that of $MAPbI_3$-based solar cells. Besides, it is also reported that α-$FAPbI_3$ has an enhanced thermal stability compared with conventional $MAPbI_3$, making it a better candidate in perovskite photovoltaic applications[224].

α-$FAPbI_3$, however, suffers from a structural stability issue under the room temperature. During the crystallization or annealing process at high temperature, $FAPbI_3$ crystallizes into the photo-active α phase with the cubic crystal structure and an idea bandgap of 1.5 eV. During the cooling down process to room temperature, α-$FAPbI_3$ gradually phase transfer into the photo-inactive δ phase with the hexagonal crystal structure and a bandgap of 2.4 eV, which makes it inappropriate for photovoltaic and optoelectronic applications. A variety of methods have been

carried out to stabilize the metastable α-$FAPbI_3$ under the room temperature, and these methods either introduce impurities into α-$FAPbI_3$, enlarge the bandgap of α-$FAPbI_3$, be impractical for applications, or cannot achieve long-term stability. Besides $FAPbI_3$, $CsPbI_3$ also faces the same structural stability problem at room temperature. Inorganic $CsPbI_3$ are shown to have a superior material stability compared to the organic-inorganic hybrid perovskites like $MAPbI_3$ and $FAPbI_3$, which makes it a better candidate for commercial devices. Similarly, photo-active α-$CsPbI_3$ will transit to photo-inactive δ-$CsPbI_3$ under the room temperature. Therefore, a long-term stabilization strategy that doesn't change the material properties and is practical for application integration for these metastable metal halide perovskites is needed.

It is also worth mentioning that with the advances in computational capability, new metal halide perovskites with different chemical compositions and crystal structures can be predicted by the high-throughput machine-learning computational study based on the designed properties. Even though these predicted perovskites may have excellent properties based on the computations, they may suffer from structural stability issues at room temperature or ambient conditions. Therefore, a general stabilization method is desired for the synthesis of the new metal halide perovskites predicted by high-throughput computational study.

4.2 Current Studies of Stabilizing Metastable Metal Halide Perovskites

The most popular stabilization method for α-$FAPbI_3$ is accomplished by mixing/doping small ions[225-227]. Several reported works discussed the possible stabilization mechanisms behind. Researchers explained the stabilization effect of mixing small ions by studying the entropy where the formation energy of the mixed α phase was too large for the phase transition to take place[225].

Meanwhile, the internal strain of α-$FAPbI_3$ lattice was reported as the driving force of the phase transition, and the compensation of the strain by incorporating small ions could prevent the phase transition[114]. Despite the success and reliability of this method, it should be pointed out that the incorporation of the small ions usually leads to an enlarged bandgap[225]. As a result, light absorption at the long-wavelength region will be inhibited, and the short-circuit current of the fabricated solar cells will decrease[228]. Recently, researchers reported several mixing strategies that stabilized the phase without the bandgap increment[228,229]. However, such incorporation showed short-term stability of no more than several weeks. Meanwhile, the incorporation of external ions that were not well-miscible with the α-$FAPbI_3$ matrix would eventually lead to disorders and heterogeneity in the lattice, and these heterogeneities would serve as non-radiative recombination centers that deteriorated the device performance[151].

Other stabilization methods of α-$FAPbI_3$ were also reported. Surface functionalization and dimension reduction are popular due to the recent emergence of low-dimensional halide perovskites. The reduction of surface energy was accomplished by large-sized/nonconductive organic molecules[230]. However, such functionalization with organic molecules would prohibit the transport of charged carriers and, therefore, led to relatively low performance. Recently, a new confinement strategy of α-$FAPbI_3$ stabilization was reported. α-$FAPbI_3$ was found to obtain phase stability within patterned nanochannels[231]. Long-term stability was achieved by limiting the expansion of α-$FAPbI_3$ during phase transition to δ-$FAPbI_3$ with the confinement of the surrounding nanochannels. However, this method lacked compatibility with conventional fabrication protocols and could hardly be applied to the device integration. Additionally, encapsulating the α-$FAPbI_3$ with mesoporous TiO_2 scaffolds was found to enhance the phase stability of α-$FAPbI_3$[232]. However, the stability didn't last long.

4.3 Epitaxial Stabilization of Metastable Metal Halide Perovskites

The epitaxially strained α-$FAPbI_3$ thin films demonstrate superior long-term structural stability in our study. Figure 39a shows XRD results of a sub-100 nm epitaxial α-$FAPbI_3$ thin film that is stable for at least 360 days after growth (red curves). In the 10 μm epitaxial thick film, which is far beyond the threshold thickness at which the strain is fully relaxed, the stabilization effect disappears: after 24 hours, XRD peaks from δ-$FAPbI_3$ can be detected (black curves). The phase stability of the strained α-$FAPbI_3$ is also verified by PL (Figure 39b) and Raman spectroscopy (Figure 39c).

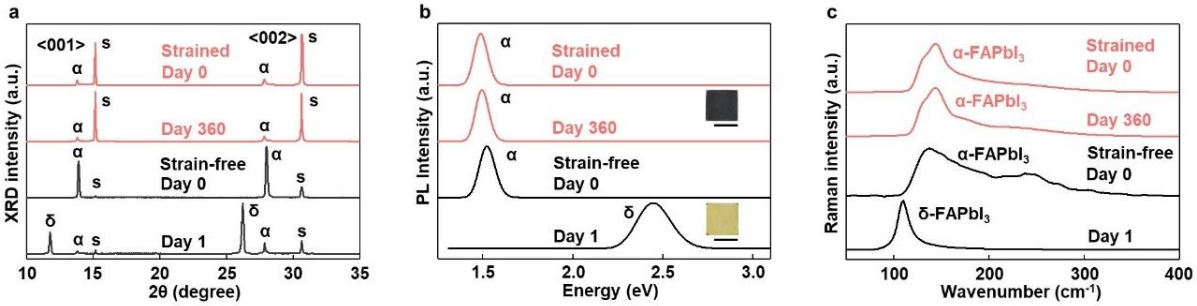

Figure 39. Epitaxial stabilization.
a, Phase stability study of thin (~100 nm, strained) and thick (~10 μm, strain-free) epitaxial α-$FAPbI_3$ on $MAPbCl_{1.50}Br_{1.50}$ substrates by XRD. α stands for α-$FAPbI_3$, δ stands for δ-$FAPbI_3$, and s stands for the substrates. The thin strained sample shows enhanced phase stability (red curves). For the thick sample, the (001) peak at 13.92˚is the same as the strain-free sample, which indicates that the top surface of the thick sample is fully relaxed (day 0, black curve). The X-ray can penetrate 10~20 μm in the halide perovskites, which explains why the substrate peaks are more intense in the thin sample than those of the thick one. The strain-free thick sample shows signs of the phase transition to δ-$FAPbI_3$ after 24 hours (black curve). **b**, Phase stability study by PL spectroscopy. Re-measurement of the thin strained sample after 360 days shows no obvious PL peak shift but a slight decrease in peak intensity due to its natural degradation into PbI_2 [126]. For the thick strain-free sample, the PL spectrum shows an emission peak close to 1.52 eV, similar to that of the strain-free α-$FAPbI_3$ bulk crystal, indicating strain relaxation in the thick sample. Re-measurement after 24 hours shows that the thick film undergoes a transition from α-phase to δ-phase. Insets are optical images of the two samples, showing clear visual clues of the phase stabilization in the thin strained sample and phase transition in the thick strain-free sample after 24 hours. Scale bars: 2 mm. **c**, Phase stability study by Raman spectroscopy. The Raman characteristics of a thin strained sample show a peak at 143 cm^{-1} with no significant difference after 360 days; the thick strain-free sample (with the peak at 136 cm^{-1}) shows signs of phase transformation to δ-$FAPbI_3$ after 24 hours, as revealed by its signature peak at 108 cm^{-1}.

Possible stabilization effect by incorporating Br or Cl into the α-$FAPbI_3$ is excluded because those foreign ions will stabilize the α-phase regardless of the epilayer thickness. X-ray photoelectron spectroscopy (XPS) measurements showing the absence of Br and Cl provide more evidence (Figure 40). We note that the XPS measurements are carried out by Kratos AXIS Supra with an aluminum Kα anode source.

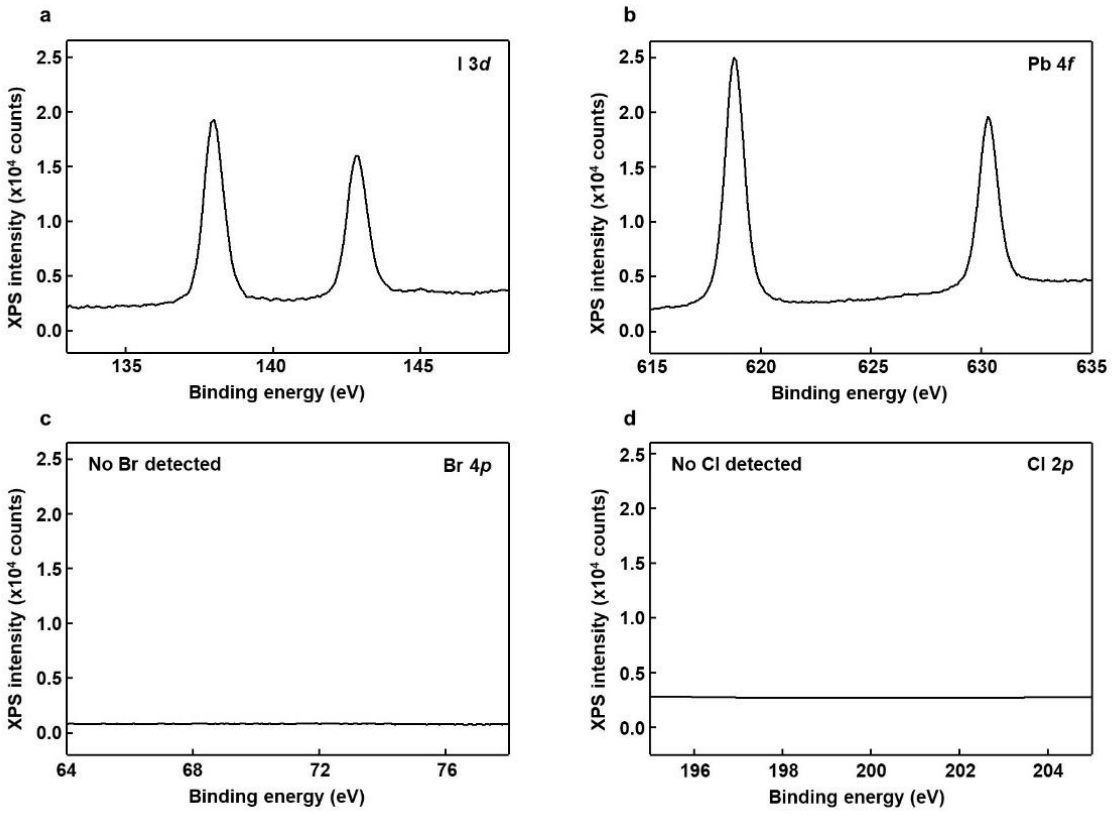

Figure 40. XPS spectra of strained α-FAPbI$_3$.
XPS spectra of **a**, I 3*d*, **b**, Pb 4*f*, **c**, Br 4*p*, and **d**, Cl 2*p* from a strained α-FAPbI$_3$ film. Results show that Br and Cl are absent in the strained α-FAPbI$_3$.

The mechanism of the stable thin α-FAPbI$_3$ can be explained by two reasons. First, the interfacial energy of the cubic α-FAPbI$_3$/cubic substrate is much lower than that of the hexagonal δ-FAPbI$_3$/cubic substrate, which is the most critical factor for the stabilization effect (see section 4.4 for calculational details). The epitaxial lattice will be constrained to the substrate due to the strong covalent bonds between them and, therefore, restricted from the phase transition. Second, the driving force of the α to δ phase transition is believed to be the internal tensile strain in the α-FAPbI$_3$ unit cell, which can induce the formation of vacancies and subsequent phase transition[113]. In this study, the epitaxial film is under compressive strain, which can neutralize the effect of the internal tensile strain. Therefore, the synergistic effect of the low-energy coherent epitaxial interface and the neutralizing compressive strain is the key to α-FAPbI$_3$ stabilization.

To experimentally demonstrate the phase stability originates from the substrate lattice constriction, we partially remove the epitaxial α-$FAPbI_3$ thin film from the substrate and investigate the phase stability of the removed α-$FAPbI_3$. Due to the limited thickness of the epitaxial α-$FAPbI_3$ thin film, it is difficult to remove the epitaxial thin film by a shape razor blade or needle. Therefore, we remove the epitaxial α-$FAPbI_3$ by polishing a substrate covered with the epitaxial α-$FAPbI_3$ thin film with sandpaper. As shown in Figure 41a, removed α-$FAPbI_3$ attached to the upper half of the sandpaper while the removed substrate ($MAPbBr_3$ in this case) attached to the lower half of the sandpaper due to the over-polish. Meanwhile, the right half of the substrate, which remains unpolished, is covered with epitaxial α-$FAPbI_3$, while the left half shows exposed substrate due to the removal of epitaxial α-$FAPbI_3$. The removed α-$FAPbI_3$, which attaches to the sandpaper, remains in black α phase right after removal. After 24 hours, the removed α-$FAPbI_3$ changes to the yellow δ phase, while the epitaxial α-$FAPbI_3$ on the right half of the substrate remains stable (Figure 41b). This experiment shows that the epitaxial stabilization of the α-$FAPbI_3$ thin film originates from the constraint by the substrate lattice and relies on the existence of the substrate. The $MAPbCl_xBr_{3-x}$ substrates are highly stable and, therefore, the epitaxial α-$FAPbI_3$ is expected to be highly stable as well.

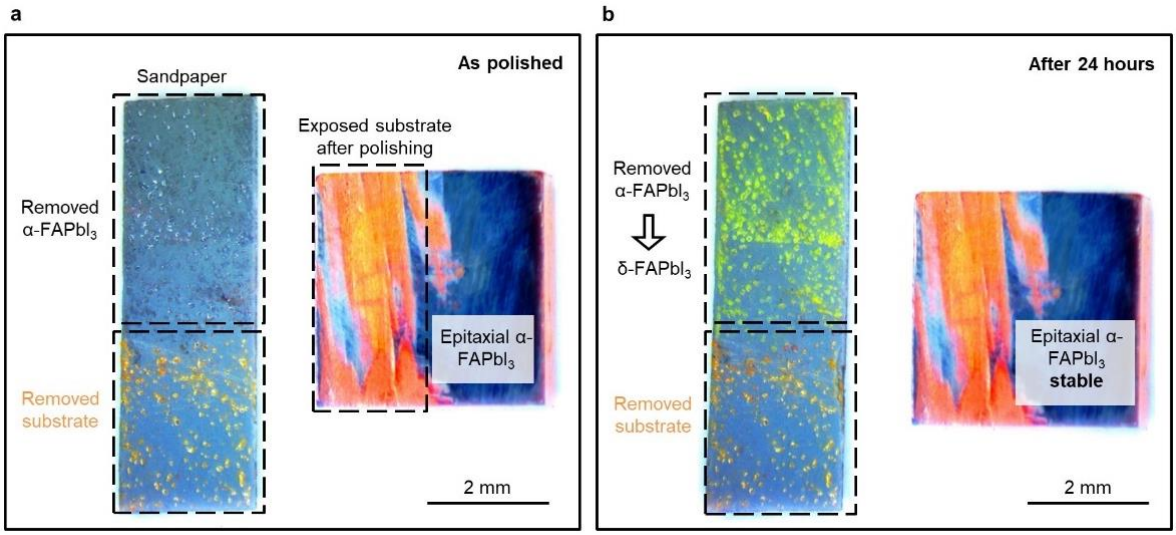

Figure 41. Stability investigation of the epitaxial and the removed α-$FAPbI_3$.
Images of the **a**, as-polished and the **b**, 24-hour aged epitaxial α-$FAPbI_3$ thin film. The left half of the epitaxial α-$FAPbI_3$ thin film is removed by a sandpaper while the right half of the epitaxial α-$FAPbI_3$ thin film remains on the substrate. Removed α-$FAPbI_3$ that is attached to the upper half of the sandpaper suffers from phase transition from black α phase to yellow □ phase after 24 hours. The epitaxial α-$FAPbI_3$ thin film remains on the substrate is stable without the phase transition. Results show the epitaxial stabilization of the epitaxial α-$FAPbI_3$ thin film relies on the constraint from the substrate lattices.

4.4 First-principle Calculations of Epitaxial Stabilization

First-principles calculations are performed to investigate epitaxial stabilization of α-$FAPbI_3$ with respect to δ-$FAPbI_3$ on $MAPbBr_3$ substrates. A typical model of epitaxial stabilization calculations compares the total energy changes of nucleating the two phases on the substrate[233]. Equation (20) shows an expression of this model for this specific system:

$$\Delta E^{\alpha-\delta} = \left(\Delta E_f^{\alpha} - \Delta E_f^{\delta}\right)d + \left(\Delta E_s^{\alpha} - \Delta E_s^{\delta}\right)d + \left(\sigma^{\alpha||S} - \sigma^{\delta||S}\right) \quad (20)$$

where the terms on the right-hand side for phase i (i = α, δ) are bulk formation energy (ΔE_f^i), strain energy (ΔE_s^i), and interfacial energy ($\sigma^{i||S}$, S means substrate) terms. Here, we use area-specific

bulk energy terms (ΔE_f^i and ΔE_s^i) by setting the film thickness to d = 1 nm. The sum of the three energy-difference terms is the total energy difference between strained α-$FAPbI_3$ and δ-$FAPbI_3$ ($\Delta E^{\alpha-\delta}$). A negative $\Delta E^{\alpha-\delta}$ indicates that the growth of α-$FAPbI_3$ is energetically more favorable than δ-$FAPbI_3$ on the $MAPbBr_3$ substrate, and thus the metastable α-$FAPbI_3$ is epitaxially stabilized. Calculation details and results for each energy term are discussed below.

The bulk formation energy (ΔE_f^i) is the energy difference between bulk i-$FAPbI_3$ and its elemental components, as shown in Equation (21):

$$\Delta E_f^i = E_i - E_{FA} - E_{Pb} - 3E_I \quad (21)$$

Because we are dealing with polymorphs with the same composition, the elemental components for both α and δ phases are the same. The total energy of the FA^+ cation is calculated based on an isolated molecule. Total energies of Pb and I are calculated using their most stable crystal structures, with a space group of Fm3m and Cmce, respectively. By setting the film thickness to 1 nm, we get area-specific bulk formation energies $\Delta E_f^\alpha = -2.279 \times 10^{-1}$ eV Å^{-2} and $\Delta E_f^\delta = -2.31 \times 10^{-1}$ eV Å^{-2}. The results indicate that δ-$FAPbI_3$ is more stable, which agrees with the experimental findings that δ-$FAPbI_3$ is more stable than α-$FAPbI_3$ at room temperature[129].

The strain energy of i-$FAPbI_3$ (ΔE_s^i) is induced by constraints from the substrate due to epitaxial nucleation and lattice mismatch. It equals to the energy difference between the films with and without the strain (Equation (22)).

$$\Delta E_s^i = E_i^{strained} - E_i \quad (22)$$

In the case of α-$FAPbI_3$, we have confirmed in the experiments that both $MAPbBr_3$ substrate and α-$FAPbI_3$ film are (001) oriented. Our calculations also show that lattice constants of α-$FAPbI_3$ and $MAPbBr_3$ have a relatively large mismatch of 6%. Therefore, we can explicitly obtain $E_{\alpha}^{strained}$ in Equation (22) by calculating α-$FAPbI_3$ with 6% bi-axial compressive strain along ab-axes. The area-specific ΔE_s^{α} is calculated to be 1.2×10^{-2} eV $Å^{-2}$.

In the case of δ-$FAPbI_3$, the possible growth model is not straightforward. Therefore, we perform a search for the lattice plane of minimal lattice mismatch with $MAPbBr_3$ (001). The hexagonal (001) close-packed plane of δ-$FAPbI_3$ has dimensions of a = b = 8.62 Å and γ = 120°. Based on this plane, the termination we found that is most compatible with $MAPbBr_3$ (001) substrate has a large vector strain of 13.2% and 3.43°, and an area strain of 18.3%. This obviously exceeds the strain threshold for a coherent interface, which is usually below 10% [233]. We thus consider δ-$FAPbI_3$ forms an incoherent interface with $MAPbBr_3$ (001). A film with the incoherent interface is not constrained by the substrate and the strain energy ΔE_s^{δ} is therefore 0.

To calculate the interfacial energy for α-$FAPbI_3$ (001)/$MAPbBr_3$ (001) ($\sigma^{\alpha||S}$), we build heterostructural models consisting of m layers of substrate and n layers of film. The two heterostructural models are shown in Figure 42a. They represent two different terminations, namely FAI/$PbBr_2$ (m = 5, n = 9) and PbI_2/MABr (m = 5, n = 11). Note that only nine layers of film material are shown in each structure for clarity.

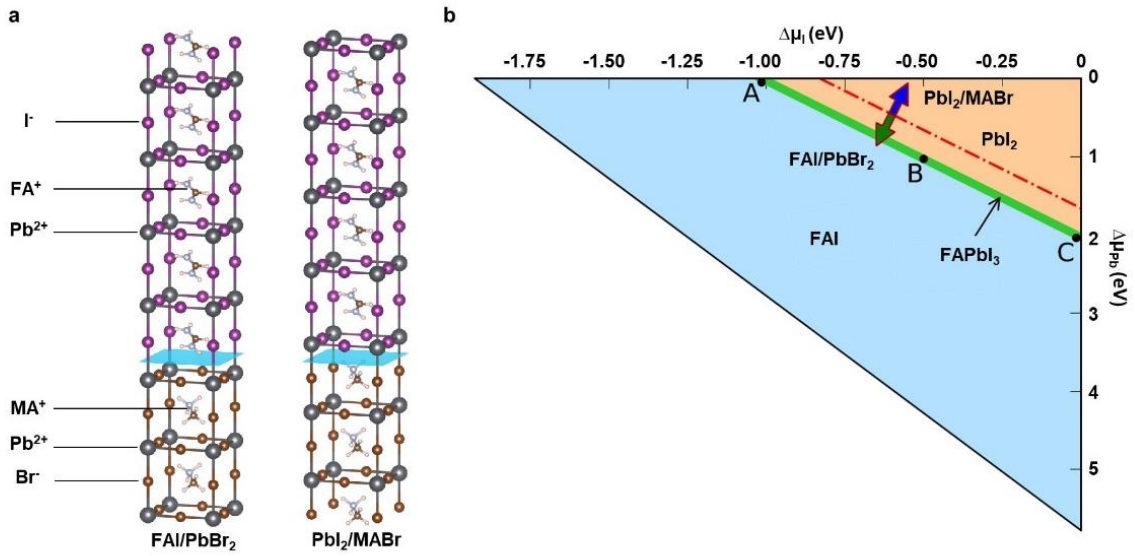

Figure 42. First-principles calculations of epitaxial stabilization.
a, Schematic heterostructural models used to calculate the epitaxial α-$FAPbI_3$ (001)/$MAPbBr_3$ (001) interface. The two interface terminations studied are FAI/$PbBr_2$ and PbI_2/MABr. In each model, the blue plane indicates the interface, the upper section indicates the $FAPbI_3$ film, and the lower section indicates the $MAPbBr_3$ substrate. **b**, Calculated phase diagram for α-$FAPbI_3$ and epitaxial α-$FAPbI_3$ (001)/$MAPbBr_3$ interface. The long, narrow region marked in green depicts the thermodynamically stable range for equilibrium growth of α-$FAPbI_3$ under different I and Pb chemical potentials. Outside this region, the compound decomposes into FAI or PbI_2. Three representative points A ($\Delta\mu_I = -1.02$ eV, $\Delta\mu_{Pb} = 0$ eV), B ($\Delta\mu_I = -0.50$ eV, $\Delta\mu_{Pb} = -1.03$ eV), and C ($\Delta\mu_I = 0$ eV, $\Delta\mu_{Pb} = -2.04$ eV) are selected for calculating the interfacial energy. The red dashed line separates the phase diagram into stability regions of the two different interfacial terminations in **a**. μ represents the chemical potentials of the corresponding atoms.

The other two possible terminations for the α-$FAPbI_3$ (001)/$MAPbBr_3$ (001) interfaces are FAI/MABr and PbI_2/$PbBr_2$ (not shown here). Through initial analysis of bonding characteristics, we find that these terminations cannot form ionic bonds between the film and the substrate like the Pb-I or Pb-Br bonds in FAI/MABr (PbI_2/$PbBr_2$). 'Physical contacts' like FAI/MABr and PbI_2/$PbBr_2$ [234] at the interface are less stable than 'chemical contacts' like FAI/$PbBr_2$ and PbI_2/MABr. Therefore, we only focus on FAI/$PbBr_2$ and PbI_2/MABr in this investigation.

After the heterostructural models are confirmed, the interfacial energy can be calculated by subtracting the bulk energy of all components in the heterostructural model. Specifically,

interfacial energy equations for these two heterostructural models are shown as Equations (23) and (24).

$$\sigma_{\mathrm{TERM1}}^{\alpha||\mathrm{S}} = \frac{1}{2\mathrm{A}}(\mathrm{E_{HS1}} - 2 \times \mathrm{E_{MAPbBr_3}} - 4 \times \mathrm{E_{FAPbI_3}^{strain}} - \mu_{\mathrm{Pb}}^{\mathrm{MAPbBr_3}} - 2 \times \mu_{\mathrm{Br}}^{\mathrm{MAPbBr_3}} - \mu_{\mathrm{FA}}^{\mathrm{FAPbI_3}} - \mu_{\mathrm{I}}^{\mathrm{FAPbI_3}}) \quad (23)$$

$$\sigma_{\mathrm{TERM2}}^{\alpha||\mathrm{S}} = \frac{1}{2\mathrm{A}}(\mathrm{E_{HS2}} - 2 \times \mathrm{E_{MAPbBr_3}} - 5 \times \mathrm{E_{FAPbI_3}^{strain}} - \mu_{\mathrm{MA}}^{\mathrm{MAPbBr_3}} - \mu_{\mathrm{Br}}^{\mathrm{MAPbBr_3}} - \mu_{\mathrm{Pb}}^{\mathrm{FAPbI_3}} - 2 \times \mu_{\mathrm{I}}^{\mathrm{FAPbI_3}}) \quad (24)$$

where $\mathrm{E_{HS}}$ is the total energy of the heterostructural model, $\mathrm{E_{MAPbBr_3}}$ is the total energy of the strain-free $MAPbBr_3$ lattice, $\mathrm{E_{FAPbI_3}^{strain}}$ is the total energy of the strained α-$FAPbI_3$ lattice, and μ represents the chemical potentials of the corresponding atoms/molecules. Each of the heterostructural models contains two identical interfaces, and A is the interfacial area.

On the right-hand side, the trailing terms represent the bulk energy of each component in the heterostructure. For example, there are nine layers of α-$FAPbI_3$ in FAI/$PbBr_2$, which equals to four intact α-$FAPbI_3$ unit cells (each has two layers) plus one extra layer of FAI. The extra or un-stoichiometric components require the determination of their chemical potentials in the corresponding film or substrate material. Here we show in detail how we obtained chemical potentials of un-stoichiometric α-$FAPbI_3$ components.

$$\Delta\mu_{\mathrm{FA}} + \Delta\mu_{\mathrm{Pb}} + 3\Delta\mu_{\mathrm{I}} = \Delta\mathrm{H}(\mathrm{FAPbI_3}) = -5.78\ \mathrm{eV} \quad (25)$$

$$\Delta\mu_{\mathrm{Pb}} + 2\Delta\mu_{\mathrm{I}} < \Delta\mathrm{H}(\mathrm{PbI_2}) = -2.02\ \mathrm{eV} \quad (26)$$

$$\Delta\mu_{FA} + \Delta\mu_{I} < \Delta H(FAI) = -3.74 \text{ eV} \quad (27)$$

According to thermodynamic stability limits expressed in Equations (25) - (27), we plot the phase diagram for α-$FAPbI_3$ against the chemical potential change $\Delta\mu_I$ and $\Delta\mu_{Pb}$. Figure 4.4b shows the phase diagram, and the long, narrow green region indicates the thermodynamic stability region for the synthesis of α-$FAPbI_3$. We select three representative points throughout the whole region for the following calculations: A ($\Delta\mu_I = -1.02$ eV, $\Delta\mu_{Pb} = 0$ eV), B ($\Delta\mu_I = -0.50$ eV, $\Delta\mu_{Pb} = -1.03$ eV), and C ($\Delta\mu_I = 0$ eV, $\Delta\mu_{Pb} = -2.04$ eV).

Similarly, we obtain the phase diagram for $MAPbBr_3$ substrate (not shown) and select one representative point P ($\Delta\mu_{Br} = -0.70$ eV, $\Delta\mu_{Pb} = -1.47$ eV) in the middle of the thermodynamically stable range. The values of point P are used as constants in Equations (23) and (24) for the un-stoichiometric $MAPbBr_3$ components.

We also added the stability limit for FAI/MABr and PbI_2/$PbBr_2$ in the phase diagram (Figure 42b). As the red dashed line shows, FAI/MABr is more stable in the region below this limit, and it covers the whole stability range of α-$FAPbI_3$. Therefore, we only need to calculate the interfacial energy for FAI/MABr, and the results are 2.86×10^{-4} eV Å^{-2}, 4.29×10^{-4} eV Å^{-2}, and 2.86×10^{-4} eV Å^{-2} at A, B, and C points, respectively. Interestingly, the composition of interfacial terminations and their preferred chemical potential conditions agree with each other. For the δ-$FAPbI_3$/$MAPbBr_3$ (001) interface, the interfacial energy $\sigma^{\delta||S}$ is given as 6.242×10^{-2} eV Å^{-2} (i.e., 1 J m^{-2}), a typical value for incoherent interfaces[233].

Results for all energy terms in Equation (20) are summarized in Table 4. The calculated total energy change of nucleating α-$FAPbI_3$ is around -2.155×10^{-1} eV Å^{-2} (regardless of chemical

potential conditions), while the value for δ-$FAPbI_3$ is -1.6858×10^{-1} eV Å^{-2}. Apparently, $\Delta E^{\alpha-\delta}$ has a negative value of around -4.7×10^{-2} eV Å^{-2} (i.e., -0.75 J m^{-2}), which indicates epitaxial stabilization of α-$FAPbI_3$ with respect to δ-$FAPbI_3$ on $MAPbBr_3$ substrates. This result is comparable to the prior successful prediction of epitaxial stabilization.

Table 4. Thermodynamic terms relevant to epitaxial nucleation of α-$FAPbI_3$ and δ-$FAPbI_3$ on cubic $MAPbBr_3$ substrates.

	α-$FAPbI_3$			□-$FAPbI_3$
	A	**B**	**C**	--
ΔE_f	-22.79×10^{-2}			-23.10×10^{-2}
ΔE_s	1.20×10^{-2}			0
σ	0.0286×10^{-2}	0.0429×10^{-2}	0.0286×10^{-2}	6.242×10^{-2}*
ΔE	-21.5614×10^{-2}	-21.5471×10^{-2}	-21.5614×10^{-2}	-16.858×10^{-2}
ΔE (α-□)	-4.7034×10^{-2}	-4.6891×10^{-2}	-4.7034×10^{-2}	--

The bulk formation energy (ΔE_f), strain energy (ΔE_s), interfacial energy (σ), total energy change (ΔE), and the difference between of the two phases (ΔE (α-δ)) are in eV Å^{-2}. The value marked with * indicates that the interface between the substrate and the □-$FAPbI_3$ is considered incoherent, and the interfacial energy term is set at 1 J m^{-2} = 6.242×10^{-2} eV Å^{-2}.

From Table 4, we can see that the bulk formation energy is the largest term but yields a small difference (3.1×10^{-3} eV Å^{-2}) between α-$FAPbI_3$ and δ-$FAPbI_3$. The strain energy term is in favor of δ-$FAPbI_3$ by a large value of 1.2×10^{-2} eV Å^{-2}. The main contribution to $\Delta E^{\alpha-\delta}$ is from interfacial energy, which is above 6×10^{-2} eV Å^{-2} and decides the overall energy preference. Notably, to accurately determine energetics using DFT calculations, we apply a large interfacial mismatch (strain = -6%) to calculate the strain energy term for α-$FAPbI_3$. However, the calculations represent an upper limit of strain's influence and guarantee a negative $\Delta E^{\alpha-\delta}$ in lower-strain circumstances. Strains below 6% would definitely yield a ΔE_s^{α} less than 1.2×10^{-2} eV Å^{-2} and a more negative $\Delta E^{\alpha-\delta}$, which better ensures epitaxial stabilization of α-$FAPbI_3$. Another experimental variable is the substrate composition. We use $MAPbBr_3$ as the substrate in the heterostructural model to calculate the interfacial energies, but in experiments we also use mixed-

halide substrates with Cl composition up to $MAPbCl_{1.50}Br_{1.50}$. This will not change the conclusion of the discussions here because the substrate energy is excluded in the calculation of the interfacial energy, as shown in Equations (23) and (24).

Besides, the consideration of the stabilization mechanism is based on the system with both the α-$FAPbI_3$ and substrate lattices rather than just focusing on the α-$FAPbI_3$ lattice alone. Two different heterostructures (i.e., the α-$FAPbI_3$/substrate and the δ-$FAPbI_3$/substrate) are used to study the interfacial energy of the nucleus crystallization during the epitaxial growth. The structure with lower interfacial energy will be more favorable during nucleus crystallization and, thus, more favorable to form. Calculation results show that the interfacial energy of the α-$FAPbI_3$/substrate (0.0286×10^{-2} eV $Å^{-2}$) is much lower than that of the δ-$FAPbI_3$/substrate (6.242×10^{-2} eV $Å^{-2}$). Therefore, the total energy of the α-$FAPbI_3$/substrate system is much smaller than that of the δ-$FAPbI_3$/substrate system because of the interfacial energy benefit, which stabilizes the epitaxial α-$FAPbI_3$ on the substrate. Additionally, the phase transition depends on not only the energy landscapes of both phases (phases before/after phase transition) but also the energy barrier between the two phases. This is where the epitaxial constraint from the substrate comes into play. In order to make the phase transition to happen, the α-$FAPbI_3$ needs to break the ionic bonds with the substrate, which represents a very high energy barrier. Therefore, due to the synergistic effects of strain and epitaxial constraint, the α-$FAPbI_3$ is stable for the long term, as observed in this study. In summary, our calculations show reliable and robust validation of the epitaxial stabilization of α-$FAPbI_3$.

4.5 Difference Between the Epitaxial Stabilization and the Current Stabilization Methods.

Besides the conventional stabilization by forming mixed perovskite alloys, the dimensional reduction, as well as the encapsulation effects, are also reported[230,231,235,236]. Herein, we discuss the differences between these methods with the epitaxial stabilization in this study and demonstrate that the epitaxial stabilization is from neither the dimensional reduction nor the encapsulation effect.

The dimensional reduction of the α-$FAPbI_3$ is usually accomplished by forming two-dimensional α-$FAPbI_3$with several atomic layers or zero-dimensional quantum dot with a limited number of lattices[230]. This low-dimensional α-$FAPbI_3$is usually capped with surfactants/capping agents to reduce the surface energy so that the metastable α phase can be stabilized. In the case of the epitaxially stabilized α-$FAPbI_3$, however, the thin film is far beyond several atomic layers and, therefore, will not be considered as the effect of the dimensional reduction.

The encapsulation effect is also reported to stabilize the α-$FAPbI_3$. Embedding the α-$FAPbI_3$ into the mesoporous TiO_2 scaffolds was reported to retard the phase transition due to the partial encapsulation by the mesoporous TiO_2 [232]. Meanwhile, the stabilization of α-$FAPbI_3$ within nanochannel was also reported[231,236]. The encapsulation of the α-$FAPbI_3$ with the nanochannels prohibits the phase transition by constraining the volume expansion of α-$FAPbI_3$ to δ-$FAPbI_3$ in the nanochannels. However, in both cases, an epitaxial relationship between the mesoporous TiO_2/nanochannel and the constrained α-$FAPbI_3$ is not necessary. In the case of the epitaxial stabilization, the α-$FAPbI_3$ is grown on the substrate, with only the bottom surface chemically bonded to the substrate. The α-$FAPbI_3$ lattice is constrained to the substrate, which is the essential difference from the encapsulation method.

By comparing these two methods with the epitaxial growth, we can conclude that both the dimensional reduction and the encapsulation effect require the entire capping/encapsulation of the α-$FAPbI_3$ by either the capping agents or space-confinement objects. In the epitaxial stabilization, the epitaxial α-$FAPbI_3$ grows on the substrate and leaves the top surface, and the side surfaces uncapped. The stabilization effect comes from the coherent growth of α-$FAPbI_3$ with the substrates. During nucleation, the crystalized α-$FAPbI_3$ will adopt the most conformal atom sequence to accommodate the existing substrate crystal structure. Once crystallized, the formed epitaxial lattice will be constrained to the substrate due to the strong chemical bonds between them. Therefore, the epitaxial growth is also used to stabilize the polymorphs that are unstable under ambient condition[237-239]. The origin of the epitaxial stabilization actually comes from the coherent interface rather than the reduced dimension or the encapsulation effect. The epitaxial α-$FAPbI_3$ thin film strongly bonds to the substrate, leaving other surfaces uncapped. Not to mention the passivation effect of the surfactant. Therefore, we can exclude the possibility of dimensional reduction and encapsulation effects regarding the phase stabilization of α-$FAPbI_3$.

Besides, a recent study shows that the residual strain produced from the thermal expansion coefficients difference during the thermal annealing can be used to temporarily stabilize the polycrystalline α-$CsPbI_3$ film[120]. However, the mechanism is different from the internal lattice strain neutralization. The isotropic (to the randomly orientated polycrystalline perovskite lattices) residual strain originates from the thermal expansion coefficients difference between the glass slide and the polycrystalline perovskites. During cooling down, the constraint from the glass will prevent the phase transition of the α-$CsPbI_3$ film. The weak constraint by van der Waals contact between the glass slides and the perovskite will be unstable against the environmental fluctuations and can gradually lose the stabilization effect. In the case of chemically epitaxially strained α-

$FAPbI_3$, we suggest that strong constraint from the ionic bond at the epitaxial interface restricts the phase transition, and neutralization of the lattice internal tensile strain can also be an important reason for stabilization. The strain we applied by epitaxial growth is an anisotropic lattice strain (to the aligned single-crystal lattices), which is different from the isotropic residual strain from the reported work[120].

4.6 Conclusion

In this chapter, we have demonstrated the long-term structural stability of the metastable phase-pure α-$FAPbI_3$ without sacrificing the semiconducting properties and the compatibility with the existing device fabrication protocol. Besides, the epitaxial strain can be applied to stabilize the polymorphs of metastable perovskites. Perovskites with new compositions are recently predicted through computational designs[240]. However, those predicted new perovskites with novel optical and electronic properties may have unstable crystal structures under room temperature or normal working conditions. In this case, epitaxial stabilization can be potentially applied to stabilize these unstable perovskites on suitable substrates. The reported approach can be generalized to other halide perovskites with different compositions and structures.

Chapter Four, in part, is a reprint of the material 'Strain Engineering and Epitaxial Stabilization of Halide Perovskites', Chen, Y., Lei, Y., Li, Y., Yu, Y., Cai, J., Chiu, M., Rao, R., Gu, Y., Wang, C., Choi, W., Hu, H., Wang, C., Li, Y., Song, J., Zhang, J., Qi, B., Lin, M., Zhang, Z., Islam, A., Maruyama, B., Dayeh, S., Li, L., Yang, K., Lo, Y., Xu, S., Nature, 2020, 577, 209. The dissertation author was the primary investigator and first author of this paper.

Chapter 5. Summary

Throughout the time in Professor Xu's group as a graduate student, I have worked towards making significant contributions in the controllable epitaxial growth of single-crystal metal halide perovskites and high-performance electronic devices based on single-crystal perovskites. Our contributions are substantial, as summarizing below.

In Chapter 2, we report the first single-crystal metal halide perovskite microarrays with controllable morphologies/orientations and large-area uniformity by the homoepitaxial growth method. The integration of the water-resist Parylene-C polymer layer enables the first direction fabrication on the single-crystal perovskite substrate, which is compatible with the advanced fabrication techniques. Based on our high-quality perovskite microarrays, we propose a platform for fabricating vertical-structure single-crystal perovskite devices with reduced dimension, high uniformity, and the ability to integrate multiple functional layers, which is fundamentally different from the previous single-crystal perovskite devices with bulky size, planar structure, and uncontrollability. Our controllable homoepitaxial growth method also shows compatibility with a broader perovskite family for high-quality single-crystal perovskite growth. As a result, a high-performance single-crystal-perovskite-based micro-LED with high EQE and high resolution is demonstrated.

In Chapter 3, we report the first controllable strain engineering of metal halide perovskites by leveraging the lattice mismatch at the heterointerface between two perovskites with different compositions and lattice constants. Preceding this endeavor, the strain engineering of metal halide perovskites has been unsuccessful, and the way of applying strain to the perovskites is

uncontrollable due to the lack of suitable substrate, inappropriate growth method, and failure to form strong chemical bonds at the interface. With the experience in the controllable homoepitaxial growth, we successfully strain the epitaxial perovskite with lattice-mismatch heteroepitaxial growth. As a result, compressively strained α-$FAPbI_3$ has demonstrated enhanced properties in light absorption and carrier dynamics.

In Chapter 4, we report a novel long-term epitaxial stabilization method to structurally stabilize the metastable α-$FAPbI_3$ without suffering from the phase transition. Our stabilization method overcomes the drawbacks of preceding stabilization methods such as the bandgap enlargement, carrier transport inhibition, fabrication incompatibility, and short-term stability. Our epitaxial stabilization method also provides insights into stabilizing other metastable perovskites and synthesizing predicted perovskites, which can potentially broaden the existing perovskite family.

In conclusion, we systematically study and solve the problems in the controllable epitaxial growth and device integration for the next-generation single-crystal metal halide perovskite electronic devices. Our unique epitaxial growth platform also provides insight into stabilizing metastable perovskite compounds, both existing and predicted. These scientific advancements can potentially benefit the broad metal halide perovskite family with different compositions and structures. Therefore, we conclude that our epitaxial growth platform significantly advances the single-crystal metal halide perovskite electronic devices.

References

1 Boyd, C. C., Cheacharoen, R., Leijtens, T. & McGehee, M. D. Understanding Degradation Mechanisms and Improving Stability of Perovskite Photovoltaics. *Chemical Reviews* **119**, 3418-3451, (2019).

2 Stranks, S. D. & Snaith, H. J. Metal-halide perovskites for photovoltaic and light-emitting devices. *Nature nanotechnology* **10**, 391-402, (2015).

3 Dunlap-Shohl, W. A., Zhou, Y., Padture, N. P. & Mitzi, D. B. Synthetic Approaches for Halide Perovskite Thin Films. *Chemical Reviews* **119**, 3193-3295, (2019).

4 Mehmood, U., Al-Ahmed, A., Afzaal, M., Al-Sulaiman, F. A. & Daud, M. Recent progress and remaining challenges in organometallic halides based perovskite solar cells. *Renewable and Sustainable Energy Reviews* **78**, 1-14, (2017).

5 Ahmadi, M., Wu, T. & Hu, B. A Review on Organic–Inorganic Halide Perovskite Photodetectors: Device Engineering and Fundamental Physics. *Advanced Materials*, (2017).

6 Huang, J., Yuan, Y., Shao, Y. & Yan, Y. Understanding the physical properties of hybrid perovskites for photovoltaic applications. *Nature Reviews Materials* **2**, 17042, (2017).

7 Yang, Z., Surrente, A., Galkowski, K., Bruyant, N., Maude, D. K., Haghighirad, A. A., Snaith, H. J., Plochocka, P. & Nicholas, R. J. Unraveling the Exciton Binding Energy and the Dielectric Constant in Single-Crystal Methylammonium Lead Triiodide Perovskite. *The journal of physical chemistry letters* **8**, 1851-1855, (2017).

8 Herz, L. M. Charge-Carrier Dynamics in Organic-Inorganic Metal Halide Perovskites. *Annual Review of Physical Chemistry* **67**, 65-89, (2016).

9 Herz, L. M. Charge-Carrier Mobilities in Metal Halide Perovskites: Fundamental Mechanisms and Limits. *ACS Energy Letters* **2**, 1539-1548, (2017).

10 Petrus, M. L., Schlipf, J., Li, C., Gujar, T. P., Giesbrecht, N., Müller-Buschbaum, P., Thelakkat, M., Bein, T., Hüttner, S. & Docampo, P. Capturing the Sun: A Review of the Challenges and Perspectives of Perovskite Solar Cells. *Advanced Energy Materials*, (2017).

11 Park, N. G. & Zhu, K. Scalable fabrication and coating methods for perovskite solar cells and solar modules. *Nature Reviews Materials* **5**, 333-350, (2020).

12 Jiang, Q., Zhao, Y., Zhang, X., Yang, X., Chen, Y., Chu, Z., Ye, Q., Li, X., Yin, Z. & You, J. Surface passivation of perovskite film for efficient solar cells. *Nature Photonics* **13**, 460-466, (2019).

13 Polman, A., Knight, M., Garnett, E. C., Ehrler, B. & Sinke, W. C. Photovoltaic materials: Present efficiencies and future challenges. *Science* **352**, aad4424, (2016).

14 Snaith, H. J. & Hacke, P. Enabling reliability assessments of pre-commercial perovskite photovoltaics with lessons learned from industrial standards. *Nature Energy* **3**, 459-465, (2018).

15 Matsushima, T., Bencheikh, F., Komino, T., Leyden, M. R., Sandanayaka, A. S. D., Qin, C. & Adachi, C. High performance from extraordinarily thick organic light-emitting diodes. *Nature*, (2019).

16 Xu, W., Hu, Q., Bai, S., Bao, C., Miao, Y., Yuan, Z., Borzda, T., Barker, A. J., Tyukalova, E., Hu, Z., Kawecki, M., Wang, H., Yan, Z., Liu, X., Shi, X., Uvdal, K., Fahlman, M., Zhang, W., Duchamp, M., Liu, J.-M., Petrozza, A., Wang, J., Liu, L.-M., Huang, W. & Gao, F. Rational molecular passivation for high-performance perovskite light-emitting diodes. *Nature Photonics* **13**, 418-424, (2019).

17 Wang, Q., Wang, X., Yang, Z., Zhou, N., Deng, Y., Zhao, J., Xiao, X., Rudd, P., Moran, A., Yan, Y. & Huang, J. Efficient sky-blue perovskite light-emitting diodes via photoluminescence enhancement. *Nature Communications* **10**, 5633, (2019).

18 Saidaminov, M. I., Adinolfi, V., Comin, R., Abdelhady, A. L., Peng, W., Dursun, I., Yuan, M., Hoogland, S., Sargent, E. H. & Bakr, O. M. Planar-integrated single-crystalline perovskite photodetectors. *Nature Communications* **6**, (2015).

19 Chen, Y., Lei, Y., Li, Y., Yu, Y., Cai, J., Chiu, M.-H., Rao, R., Gu, Y., Wang, C., Choi, W., Hu, H., Wang, C., Li, Y., Song, J., Zhang, J., Qi, B., Lin, M., Zhang, Z., Islam, A. E., Maruyama, B., Dayeh, S., Li, L.-J., Yang, K., Lo, Y.-H. & Xu, S. Strain engineering and epitaxial stabilization of halide perovskites. *Nature* **577**, 209-215, (2020).

20 Bao, C., Chen, Z., Fang, Y., Wei, H., Deng, Y., Xiao, X., Li, L. & Huang, J. Low-Noise and Large-Linear-Dynamic-Range Photodetectors Based on Hybrid-Perovskite Thin-Single-Crystals. *Advanced Materials* **29**, (2017).

21 Yu, W., Li, F., Yu, L., Niazi, M. R., Zou, Y., Corzo, D., Basu, A., Ma, C., Dey, S., Tietze, M. L., Buttner, U., Wang, X., Wang, Z., Hedhili, M. N., Guo, C., Wu, T. & Amassian, A. Single crystal hybrid perovskite field-effect transistors. *Nature Communications* **9**, 5354, (2018).

22 Senanayak, S. P., Yang, B., Thomas, T. H., Giesbrecht, N., Huang, W., Gann, E., Nair, B., Goedel, K., Guha, S., Moya, X., McNeill, C. R., Docampo, P., Sadhanala, A., Friend, R. H. & Sirringhaus, H. Understanding charge transport in lead iodide perovskite thin-film field-effect transistors. *Science Advances* **3**, e1601935, (2017).

23 Wang, J., Senanayak, S. P., Liu, J., Hu, Y., Shi, Y., Li, Z., Zhang, C., Yang, B., Jiang, L., Di, D., Ievlev, A. V., Ovchinnikova, O. S., Ding, T., Deng, H., Tang, L., Guo, Y., Wang, J., Xiao, K., Venkateshvaran, D., Jiang, L., Zhu, D. & Sirringhaus, H. Investigation of Electrode Electrochemical Reactions in CH3NH3PbBr3 Perovskite Single-Crystal Field-Effect Transistors. *Advanced Materials* **0**, 1902618, (2019).

24 Wei, H., DeSantis, D., Wei, W., Deng, Y., Guo, D., Savenije, T. J., Cao, L. & Huang, J. Dopant compensation in alloyed CH3NH3PbBr3-xClx perovskite single crystals for gamma-ray spectroscopy. *Nature Materials* **16**, 826-833, (2017).

25 Yakunin, S., Dirin, D. N., Shynkarenko, Y., Morad, V., Cherniukh, I., Nazarenko, O., Kreil, D., Nauser, T. & Kovalenko, M. V. Detection of gamma photons using solution-grown single crystals of hybrid lead halide perovskites. *Nature Photonics* **10**, 585-589, (2016).

26 Steele, J. A., Pan, W., Martin, C., Keshavarz, M., Debroye, E., Yuan, H., Banerjee, S., Fron, E., Jonckheere, D., Kim, C. W., Baekelant, W., Niu, G., Tang, J., Vanacken, J., Van der Auweraer, M., Hofkens, J. & Roeffaers, M. B. J. Photophysical Pathways in Highly Sensitive Cs2AgBiBr6 Double-Perovskite Single-Crystal X-Ray Detectors. *Advanced Materials* **0**, 1804450, (2018).

27 Yang, Z., Lu, J., ZhuGe, M., Cheng, Y., Hu, J., Li, F., Qiao, S., Zhang, Y., Hu, G., Yang, Q., Peng, D., Liu, K. & Pan, C. Controllable Growth of Aligned Monocrystalline CsPbBr3 Microwire Arrays for Piezoelectric-Induced Dynamic Modulation of Single-Mode Lasing. *Advanced Materials* **31**, 1900647, (2019).

28 Correa-Baena, J.-P., Saliba, M., Buonassisi, T., Grätzel, M., Abate, A., Tress, W. & Hagfeldt, A. Promises and challenges of perovskite solar cells. *Science* **358**, 739-744, (2017).

29 Green, M. A., Dunlop, E. D., Hohl-Ebinger, J., Yoshita, M., Kopidakis, N. & Ho-Baillie, A. W. Y. Solar cell efficiency tables (Version 55). *Progress in Photovoltaics: Research and Applications* **28**, 3-15, (2020).

30 Braly, I. L., deQilettes, D. W., Pazos-Outon, L. M., Burke, S., Ziffer, M. E., Ginger, D. S. & Hillhouse, H. W. Hybrid perovskite films approaching the radiative limit with over 90% photoluminescence quantum efficiency. *Nature Photonics* **12**, 355-+, (2018).

31 Song, Z., Zhao, J. & Liu, Q. Luminescent perovskites: recent advances in theory and experiments. *Inorganic Chemistry Frontiers* **6**, 2969-3011, (2019).

32 Protesescu, L., Yakunin, S., Bodnarchuk, M. I., Krieg, F., Caputo, R., Hendon, C. H., Yang, R. X., Walsh, A. & Kovalenko, M. V. Nanocrystals of Cesium Lead Halide Perovskites (CsPbX3, X = Cl, Br, and I): Novel Optoelectronic Materials Showing Bright Emission with Wide Color Gamut. *Nano Letters* **15**, 3692-3696, (2015).

33 Lu, M., Zhang, Y., Wang, S., Guo, J., Yu, W. W. & Rogach, A. L. Metal Halide Perovskite Light-Emitting Devices: Promising Technology for Next-Generation Displays. *Advanced Functional Materials* **29**, 1902008, (2019).

34 Bakr, O. M. & Mohammed, O. F. Powering up perovskite photoresponse. *Science* **355**, 1260-1261, (2017).

35 Lin, K., Xing, J., Quan, L. N., de Arquer, F. P. G., Gong, X., Lu, J., Xie, L., Zhao, W., Zhang, D., Yan, C., Li, W., Liu, X., Lu, Y., Kirman, J., Sargent, E. H., Xiong, Q. & Wei,

Z. Perovskite light-emitting diodes with external quantum efficiency exceeding 20 per cent. *Nature* **562**, 245-248, (2018).

36 Shen, Y., Cheng, L.-P., Li, Y.-Q., Li, W., Chen, J.-D., Lee, S.-T. & Tang, J.-X. High-Efficiency Perovskite Light-Emitting Diodes with Synergetic Outcoupling Enhancement. *Advanced Materials* **31**, 1901517, (2019).

37 Cao, Y., Wang, N., Tian, H., Guo, J., Wei, Y., Chen, H., Miao, Y., Zou, W., Pan, K., He, Y., Cao, H., Ke, Y., Xu, M., Wang, Y., Yang, M., Du, K., Fu, Z., Kong, D., Dai, D., Jin, Y., Li, G., Li, H., Peng, Q., Wang, J. & Huang, W. Perovskite light-emitting diodes based on spontaneously formed submicrometre-scale structures. *Nature* **562**, 249-253, (2018).

38 Liu, R. & Xu, K. Blue perovskite light-emitting diodes (LEDs): A minireview. *Instrumentation Science & Technology*, 1-21, (2020).

39 Xie, C., Liu, C.-K., Loi, H.-L. & Yan, F. Perovskite-Based Phototransistors and Hybrid Photodetectors. *Advanced Functional Materials* **30**, 1903907, (2020).

40 Wei, H. & Huang, J. Halide lead perovskites for ionizing radiation detection. *Nature Communications* **10**, 1066, (2019).

41 Kim, Y. C., Kim, K. H., Son, D.-Y., Jeong, D.-N., Seo, J.-Y., Choi, Y. S., Han, I. T., Lee, S. Y. & Park, N.-G. Printable organometallic perovskite enables large-area, low-dose X-ray imaging. *Nature* **550**, 87, (2017).

42 Yakunin, S., Sytnyk, M., Kriegner, D., Shrestha, S., Richter, M., Matt, G. J., Azimi, H., Brabec, C. J., Stangl, J., Kovalenko, M. V. & Heiss, W. Detection of X-ray photons by solution-processed lead halide perovskites. *Nature Photonics* **9**, 444-449, (2015).

43 Zhuang, R., Wang, X., Ma, W., Wu, Y., Chen, X., Tang, L., Zhu, H., Liu, J., Wu, L., Zhou, W., Liu, X. & Yang, Y. Highly sensitive X-ray detector made of layered perovskite-like (NH4)3Bi2I9 single crystal with anisotropic response. *Nature Photonics* **13**, 602-608, (2019).

44 Wei, W., Zhang, Y., Xu, Q., Wei, H., Fang, Y., Wang, Q., Deng, Y., Li, T., Gruverman, A. & Cao, L. Monolithic integration of hybrid perovskite single crystals with heterogenous substrate for highly sensitive X-ray imaging. *Nature Photonics* **11**, 315-321, (2017).

45 Yang, B., Pan, W., Wu, H., Niu, G., Yuan, J.-H., Xue, K.-H., Yin, L., Du, X., Miao, X.-S., Yang, X., Xie, Q. & Tang, J. Heteroepitaxial passivation of Cs2AgBiBr6 wafers with suppressed ionic migration for X-ray imaging. *Nature Communications* **10**, 1989, (2019).

46 Gao, Y., Wei, Z., Yoo, P., Shi, E., Zeller, M., Zhu, C., Liao, P. & Dou, L. Highly Stable Lead-Free Perovskite Field-Effect Transistors Incorporating Linear π-Conjugated Organic Ligands. *Journal of the American Chemical Society* **141**, 15577-15585, (2019).

47 Chen, Y., He, M., Peng, J., Sun, Y. & Liang, Z. Structure and growth control of organic–inorganic halide perovskites for optoelectronics: From polycrystalline films to single crystals. *Advanced Science* **3**, (2016).

48 Luo, D., Su, R., Zhang, W., Gong, Q. & Zhu, R. Minimizing non-radiative recombination losses in perovskite solar cells. *Nature Reviews Materials* **5**, 44-60, (2019).

49 Chu, Z., Yang, M., Schulz, P., Wu, D., Ma, X., Seifert, E., Sun, L., Li, X., Zhu, K. & Lai, K. Impact of grain boundaries on efficiency and stability of organic-inorganic trihalide perovskites. *Nature Communications* **8**, 2230, (2017).

50 Reid, O. G., Yang, M., Kopidakis, N., Zhu, K. & Rumbles, G. Grain-Size-Limited Mobility in Methylammonium Lead Iodide Perovskite Thin Films. *ACS Energy Letters* **1**, 561-565, (2016).

51 Wang, Q., Chen, B., Liu, Y., Deng, Y., Bai, Y., Dong, Q. & Huang, J. Scaling behavior of moisture-induced grain degradation in polycrystalline hybrid perovskite thin films. *Energy & Environmental Science* **10**, 516-522, (2017).

52 Szostak, R., Silva, J. C., Turren-Cruz, S.-H., Soares, M. M., Freitas, R. O., Hagfeldt, A., Tolentino, H. C. N. & Nogueira, A. F. Nanoscale mapping of chemical composition in organic-inorganic hybrid perovskite films. *Science Advances* **5**, eaaw6619, (2019).

53 Cheng, X., Yang, S., Cao, B., Tao, X. & Chen, Z. Single Crystal Perovskite Solar Cells: Development and Perspectives. *Advanced Functional Materials* **30**, 1905021, (2020).

54 Shao, Y., Fang, Y., Li, T., Wang, Q., Dong, Q., Deng, Y., Yuan, Y., Wei, H., Wang, M. & Gruverman, A. Grain boundary dominated ion migration in polycrystalline organic–inorganic halide perovskite films. *Energy & Environmental Science* **9**, 1752-1759, (2016).

55 Hong, K., Le, Q. V., Kim, S. Y. & Jang, H. W. Low-dimensional halide perovskites: review and issues. *Journal of Materials Chemistry C* **6**, 2189-2209, (2018).

56 Lei, Y., Chen, Y., Gu, Y., Wang, C., Huang, Z., Qian, H., Nie, J., Hollett, G., Choi, W., Yu, Y., Kim, N., Wang, C., Zhang, T., Hu, H., Zhang, Y., Li, X., Li, Y., Shi, W., Liu, Z., Sailor, M. J., Dong, L., Lo, Y.-H., Luo, J. & Xu, S. Controlled Homoepitaxial Growth of Hybrid Perovskites. *Advanced Materials* **30**, 1705992, (2018).

57 Jiang, X., Fu, X., Ju, D., Yang, S., Chen, Z. & Tao, X. Designing Large-Area Single-Crystal Perovskite Solar Cells. *ACS Energy Letters* **5**, 1797-1803, (2020).

58 Yang, Z., Deng, Y., Zhang, X., Wang, S., Chen, H., Yang, S., Khurgin, J., Fang, N. X., Zhang, X. & Ma, R. High-Performance Single-Crystalline Perovskite Thin-Film Photodetector. *Advanced Materials* **30**, (2018).

59 Babu, R., Giribabu, L. & Singh, S. P. Recent Advances in Halide-Based Perovskite Crystals and Their Optoelectronic Applications. *Crystal Growth & Design* **18**, 2645-2664, (2018).

60 Liu, Y., Yang, Z., Cui, D., Ren, X., Sun, J., Liu, X., Zhang, J., Wei, Q., Fan, H. & Yu, F. Two-Inch-Sized Perovskite CH3NH3PbX3 (X= Cl, Br, I) Crystals: Growth and Characterization. *Advanced Materials* **27**, 5176-5183, (2015).

61 Dang, Y., Liu, Y., Sun, Y., Yuan, D., Liu, X., Lu, W., Liu, G., Xia, H. & Tao, X. Bulk crystal growth of hybrid perovskite material CH 3 NH 3 PbI 3. *CrystEngComm* **17**, 665-670, (2015).

62 Xing, J., Wang, Q., Dong, Q., Yuan, Y., Fang, Y. & Huang, J. Ultrafast ion migration in hybrid perovskite polycrystalline thin films under light and suppression in single crystals. *Physical Chemistry Chemical Physics* **18**, 30484-30490, (2016).

63 Wang, Y., Sun, X., Chen, Z., Cai, Z., Zhou, H., Lu, T.-M. & Shi, J. Defect-engineered epitaxial VO2±δ in strain engineering of heterogeneous soft crystals. *Science Advances* **4**, eaar3679, (2018).

64 Wang, Y., Gao, L., Yang, Y., Xiang, Y., Chen, Z., Dong, Y., Zhou, H., Cai, Z., Wang, G.-C. & Shi, J. Nontrivial strength of van der Waals epitaxial interaction in soft perovskites. *Physical Review Materials* **2**, 076002, (2018).

65 Dong, Q., Song, J., Fang, Y., Shao, Y., Ducharme, S. & Huang, J. Lateral-Structure Single-Crystal Hybrid Perovskite Solar Cells via Piezoelectric Poling. *Advanced Materials* **28**, 2816-2821, (2016).

66 Liu, Y., Zhang, Y., Zhao, K., Yang, Z., Feng, J., Zhang, X., Wang, K., Meng, L., Ye, H., Liu, M. & Liu, S. A 1300 mm2 Ultrahigh-Performance Digital Imaging Assembly using High-Quality Perovskite Single Crystals. *Advanced Materials* **30**, 1707314, (2018).

67 Liu, Y., Zhang, Y., Yang, Z., Yang, D., Ren, X., Pang, L. & Liu, S. F. Thinness-and Shape-Controlled Growth for Ultrathin Single-Crystalline Perovskite Wafers for Mass Production of Superior Photoelectronic Devices. *Advanced Materials* **28**, 9204-9209, (2016).

68 Liu, Y., Sun, J., Yang, Z., Yang, D., Ren, X., Xu, H., Yang, Z. & Liu, S. F. 20-mm-Large Single-Crystalline Formamidinium-Perovskite Wafer for Mass Production of Integrated Photodetectors. *Advanced Optical Materials* **4**, 1829-1837, (2016).

69 Oksenberg, E., Sanders, E., Popovitz-Biro, R., Houben, L. & Joselevich, E. Surface-Guided CsPbBr3 Perovskite Nanowires on Flat and Faceted Sapphire with Size-Dependent Photoluminescence and Fast Photoconductive Response. *Nano Lett* **18**, 424-433, (2018).

70 Liu, Z., Li, Y., Guan, X., Mi, Y., Al-Hussain, A., Ha, S. T., Chiu, M.-H., Ma, C., Amer, M. R., Li, L.-J., Liu, J., Xiong, Q., Wang, J., Liu, X. & Wu, T. One-Step Vapor-Phase Synthesis and Quantum-Confined Exciton in Single-Crystal Platelets of Hybrid Halide Perovskites. *The journal of physical chemistry letters* **10**, 2363-2371, (2019).

71 Wang, Y., Sun, X., Chen, Z., Sun, Y. Y., Zhang, S., Lu, T. M., Wertz, E. & Shi, J. High-Temperature Ionic Epitaxy of Halide Perovskite Thin Film and the Hidden Carrier Dynamics. *Advanced Materials* **29**, (2017).

72 Wang, L., Chen, P., Thongprong, N., Young, M., Kuttipillai, P. S., Jiang, C., Zhang, P., Sun, K., Duxbury, P. M. & Lunt, R. R. Unlocking the Single-Domain Epitaxy of Halide Perovskites. *Advanced Materials Interfaces*, (2017).

73 Gu, Z., Huang, Z., Li, C., Li, M. & Song, Y. A general printing approach for scalable growth of perovskite single-crystal films. *Science Advances* **4**, eaat2390, (2018).

74 Liu, Y., Zhang, Y., Yang, Z., Ye, H., Feng, J., Xu, Z., Zhang, X., Munir, R., Liu, J., Zuo, P., Li, Q., Hu, M., Meng, L., Wang, K., Smilgies, D.-M., Zhao, G., Xu, H., Yang, Z., Amassian, A., Li, J., Zhao, K. & Liu, S. Multi-inch single-crystalline perovskite membrane for high-detectivity flexible photosensors. *Nature Communications* **9**, 5302, (2018).

75 Huang, Y., Zhang, Y., Sun, J., Wang, X., Sun, J., Chen, Q., Pan, C. & Zhou, H. The Exploration of Carrier Behavior in the Inverted Mixed Perovskite Single-Crystal Solar Cells. *Advanced Materials Interfaces* **5**, 1800224, (2018).

76 Chen, Z., Dong, Q., Liu, Y., Bao, C., Fang, Y., Lin, Y., Tang, S., Wang, Q., Xiao, X. & Bai, Y. Thin single crystal perovskite solar cells to harvest below-bandgap light absorption. *Nature Communications* **8**, 1890, (2017).

77 Lee, L., Baek, J., Park, K. S., Lee, Y., Shrestha, N. K. & Sung, M. M. Wafer-scale single-crystal perovskite patterned thin films based on geometrically-confined lateral crystal growth. *Nature Communications* **8**, 15882, (2017).

78 Zhumekenov, A. A., Burlakov, V. M., Saidaminov, M. I., Alofi, A., Haque, M. A., Turedi, B., Davaasuren, B., Dursun, I., Cho, N. & El-Zohry, A. M. The Role of Surface Tension in the Crystallization of Metal Halide Perovskites. *ACS Energy Letters* **2**, 1782-1788, (2017).

79 Liu, Y., Dong, Q., Fang, Y., Lin, Y., Deng, Y. & Huang, J. Fast Growth of Thin MAPbI3 Crystal Wafers on Aqueous Solution Surface for Efficient Lateral-Structure Perovskite Solar Cells. *Advanced Functional Materials* **0**, 1807707, (2019).

80 Xu, S., Shen, Y., Ding, Y. & Wang, Z. L. Growth and transfer of monolithic horizontal ZnO nanowire superstructures onto flexible substrates. *Advanced Functional Materials* **20**, 1493-1497, (2010).

81 Aharon, S., Cohen, B. E. & Etgar, L. Hybrid Lead Halide Iodide and Lead Halide Bromide in Efficient Hole Conductor Free Perovskite Solar Cell. *The Journal of Physical Chemistry C* **118**, 17160-17165, (2014).

82 Leblebici, S. Y., Leppert, L., Li, Y., Reyes-Lillo, S. E., Wickenburg, S., Wong, E., Lee, J., Melli, M., Ziegler, D., Angell, D. K., Ogletree, D. F., Ashby, Paul D., Toma, F. M., Neaton, J. B., Sharp, I. D. & Weber-Bargioni, A. Facet-dependent photovoltaic efficiency variations in single grains of hybrid halide perovskite. *Nature Energy* **1**, 16093, (2016).

83 Kang, K., Ahn, H., Song, Y., Lee, W., Kim, J., Kim, Y., Yoo, D. & Lee, T. High-Performance Solution-Processed Organo-Metal Halide Perovskite Unipolar Resistive Memory Devices in a Cross-Bar Array Structure. *Advanced Materials* **31**, 1804841, (2019).

84 Kalinowski, J. Organic Light Emitting Diodes: Principles. *Characteristics, and Processes, March Dekker, Rochester: New York* **273**, (2005).

85 Wong, A. B., Lai, M., Eaton, S. W., Yu, Y., Lin, E., Dou, L., Fu, A. & Yang, P. Growth and anion exchange conversion of CH3NH3PbX3 nanorod arrays for light-emitting diodes. *Nano Letters* **15**, 5519-5524, (2015).

86 Xiao, Z. G., Kerner, R. A., Zhao, L. F., Tran, N. L., Lee, K. M., Koh, T. W., Scholes, G. D. & Rand, B. P. Efficient perovskite light-emitting diodes featuring nanometre-sized crystallites. *Nature Photonics* **11**, 108-115, (2017).

87 Shi, Z.-F., Sun, X.-G., Wu, D., Xu, T.-T., Zhuang, S.-W., Tian, Y.-T., Li, X.-J. & Du, G.-T. High-performance planar green light-emitting diodes based on a PEDOT:PSS/CH3NH3PbBr3/ZnO sandwich structure. *Nanoscale* **8**, 10035-10042, (2016).

88 Ling, Y., Yuan, Z., Tian, Y., Wang, X., Wang, J. C., Xin, Y., Hanson, K., Ma, B. & Gao, H. Bright Light-Emitting Diodes Based on Organometal Halide Perovskite Nanoplatelets. *Advanced Materials* **28**, 305-311, (2016).

89 Dong, Q., Fang, Y., Shao, Y., Mulligan, P., Qiu, J., Cao, L. & Huang, J. Electron-hole diffusion lengths> 175 μm in solution-grown CH3NH3PbI3 single crystals. *Science* **347**, 967-970, (2015).

90 Tan, Z.-K., Moghaddam, R. S., Lai, M. L., Docampo, P., Higler, R., Deschler, F., Price, M., Sadhanala, A., Pazos, L. M. & Credgington, D. Bright light-emitting diodes based on organometal halide perovskite. *Nature nanotechnology* **9**, 687-692, (2014).

91 Zhou, H., Chen, Q., Li, G., Luo, S., Song, T.-b., Duan, H.-S., Hong, Z., You, J., Liu, Y. & Yang, Y. Interface engineering of highly efficient perovskite solar cells. *Science* **345**, 542-546, (2014).

92 Smith, C. S. Piezoresistance Effect in Germanium and Silicon. *Physical Review* **94**, 42-49, (1954).

93 Kisielowski, C., Krüger, J., Ruvimov, S., Suski, T., Ager, J. W., Jones, E., Liliental-Weber, Z., Rubin, M., Weber, E. R., Bremser, M. D. & Davis, R. F. Strain-related phenomena in GaN thin films. *Physical Review B* **54**, 17745-17753, (1996).

94 Zeches, R. J., Rossell, M. D., Zhang, J. X., Hatt, A. J., He, Q., Yang, C. H., Kumar, A., Wang, C. H., Melville, A., Adamo, C., Sheng, G., Chu, Y. H., Ihlefeld, J. F., Erni, R., Ederer, C., Gopalan, V., Chen, L. Q., Schlom, D. G., Spaldin, N. A., Martin, L. W. & Ramesh, R. A strain-driven morphotropic phase boundary in BiFeO3. *Science* **326**, 977-980, (2009).

95 Bark, C. W., Felker, D. A., Wang, Y., Zhang, Y., Jang, H. W., Folkman, C. M., Park, J. W., Baek, S. H., Zhou, H., Fong, D. D., Pan, X. Q., Tsymbal, E. Y., Rzchowski, M. S. & Eom, C. B. Tailoring a two-dimensional electron gas at the LaAlO3/SrTiO3 (001) interface

by epitaxial strain. *Proceedings of the National Academy of Sciences* **108**, 4720-4724, (2011).

96 Guinea, F., Katsnelson, M. I. & Geim, A. K. Energy gaps and a zero-field quantum Hall effect in graphene by strain engineering. *Nature Physics* **6**, 30, (2009).

97 Castellanos-Gomez, A., Roldán, R., Cappelluti, E., Buscema, M., Guinea, F., van der Zant, H. S. J. & Steele, G. A. Local Strain Engineering in Atomically Thin MoS2. *Nano Letters* **13**, 5361-5366, (2013).

98 Conley, H. J., Wang, B., Ziegler, J. I., Haglund, R. F., Pantelides, S. T. & Bolotin, K. I. Bandgap Engineering of Strained Monolayer and Bilayer MoS2. *Nano Letters* **13**, 3626-3630, (2013).

99 Yang, S., Wang, C., Sahin, H., Chen, H., Li, Y., Li, S.-S., Suslu, A., Peeters, F. M., Liu, Q., Li, J. & Tongay, S. Tuning the Optical, Magnetic, and Electrical Properties of ReSe2 by Nanoscale Strain Engineering. *Nano Letters* **15**, 1660-1666, (2015).

100 Cao, J., Ertekin, E., Srinivasan, V., Fan, W., Huang, S., Zheng, H., Yim, J. W. L., Khanal, D. R., Ogletree, D. F., Grossman, J. C. & Wu, J. Strain engineering and one-dimensional organization of metal–insulator domains in single-crystal vanadium dioxide beams. *Nature nanotechnology* **4**, 732, (2009).

101 Valencia, S., Crassous, A., Bocher, L., Garcia, V., Moya, X., Cherifi, R. O., Deranlot, C., Bouzehouane, K., Fusil, S., Zobelli, A., Gloter, A., Mathur, N. D., Gaupp, A., Abrudan, R., Radu, F., Barthélémy, A. & Bibes, M. Interface-induced room-temperature multiferroicity in BaTiO3. *Nature Materials* **10**, 753, (2011).

102 Llordés, A., Palau, A., Gázquez, J., Coll, M., Vlad, R., Pomar, A., Arbiol, J., Guzmán, R., Ye, S., Rouco, V., Sandiumenge, F., Ricart, S., Puig, T., Varela, M., Chateigner, D., Vanacken, J., Gutiérrez, J., Moshchalkov, V., Deutscher, G., Magen, C. & Obradors, X. Nanoscale strain-induced pair suppression as a vortex-pinning mechanism in high-temperature superconductors. *Nature Materials* **11**, 329, (2012).

103 Ohtomo, A. & Hwang, H. Y. A high-mobility electron gas at the LaAlO3/SrTiO3 heterointerface. *Nature* **427**, 423, (2004).

104 Matsuno, J., Ogawa, N., Yasuda, K., Kagawa, F., Koshibae, W., Nagaosa, N., Tokura, Y. & Kawasaki, M. Interface-driven topological Hall effect in SrRuO3-SrIrO3 bilayer. *Sci Adv* **2**, e1600304, (2016).

105 Fiebig, M., Lottermoser, T., Meier, D. & Trassin, M. The evolution of multiferroics. *Nature Reviews Materials* **1**, 16046, (2016).

106 Garcia-Barriocanal, J., Rivera-Calzada, A., Varela, M., Sefrioui, Z., Iborra, E., Leon, C., Pennycook, S. J. & Santamaria, J. Colossal ionic conductivity at interfaces of epitaxial ZrO2:Y2O3/SrTiO3 heterostructures. *Science* **321**, 676-680, (2008).

107 Lee, M. L., Fitzgerald, E. A., Bulsara, M. T., Currie, M. T. & Lochtefeld, A. Strained Si, SiGe, and Ge channels for high-mobility metal-oxide-semiconductor field-effect transistors. *Journal of applied physics* **97**, 011101, (2004).

108 Teng, C.-H., Zhang, L., Deng, H. & Ku, P.-C. Strain-induced red-green-blue wavelength tuning in InGaN quantum wells. *Applied Physics Letters* **108**, 071104, (2016).

109 Roldán, R., Castellanos-Gomez, A., Cappelluti, E. & Guinea, F. Strain engineering in semiconducting two-dimensional crystals. *Journal of Physics: Condensed Matter* **27**, 313201, (2015).

110 Sun, M., Fang, Q., Zhang, Z., Xie, D., Sun, Y., Xu, J., Li, W., Ren, T. & Zhang, Y. All-Inorganic Perovskite Nanowires-InGaZnO Heterojunction for High-Performance Ultraviolet-Visible Photodetectors. *ACS Appl Mater Interfaces* **10**, 7231-7238, (2018).

111 Chen, J., Morrow, D. J., Fu, Y., Zheng, W., Zhao, Y., Dang, L., Stolt, M. J., Kohler, D. D., Wang, X. & Czech, K. J. Single-Crystal Thin Films of Cesium Lead Bromide Perovskite Epitaxially Grown on Metal Oxide Perovskite (SrTiO3). *Journal of the American Chemical Society* **139**, 13525-13532, (2017).

112 Li, X. Y., Luo, Y. Q., Holt, M. V., Cai, Z. H. & Fenning, D. P. Residual Nanoscale Strain in Cesium Lead Bromide Perovskite Reduces Stability and Shifts Local Luminescence. *Chemistry of Materials* **31**, 2778-2785, (2019).

113 Saidaminov, M. I., Kim, J., Jain, A., Quintero-Bermudez, R., Tan, H. R., Long, G. K., Tan, F. R., Johnston, A., Zhao, Y. C., Voznyy, O. & Sargent, E. H. Suppression of atomic vacancies via incorporation of isovalent small ions to increase the stability of halide perovskite solar cells in ambient air. *Nature Energy* **3**, 648-+, (2018).

114 Zheng, X., Wu, C., Jha, S. K., Li, Z., Zhu, K. & Priya, S. Improved Phase Stability of Formamidinium Lead Triiodide Perovskite by Strain Relaxation. *ACS Energy Letters* **1**, 1014-1020, (2016).

115 Shai, X., Wang, J., Sun, P., Huang, W., Liao, P., Cheng, F., Zhu, B., Chang, S.-Y., Yao, E.-P., Shen, Y., Miao, L., Yang, Y. & Wang, M. Achieving ordered and stable binary metal perovskite via strain engineering. *Nano Energy* **48**, 117-127, (2018).

116 Tsai, H., Asadpour, R., Blancon, J.-C., Stoumpos, C. C., Durand, O., Strzalka, J. W., Chen, B., Verduzco, R., Ajayan, P. M. & Tretiak, S. Light-induced lattice expansion leads to high-efficiency perovskite solar cells. *Science* **360**, 67-70, (2018).

117 Jones, T. W., Osherov, A., Alsari, M., Sponseller, M., Duck, B. C., Jung, Y.-K., Settens, C., Niroui, F., Brenes, R., Stan, C. V., Li, Y., Abdi-Jalebi, M., Tamura, N., Macdonald, J. E., Burghammer, M., Friend, R. H., Bulović, V., Walsh, A., Wilson, G. J., Lilliu, S. & Stranks, S. D. Lattice strain causes non-radiative losses in halide perovskites. *Energy & Environmental Science* **12**, 596-606, (2019).

118 Zhao, J., Deng, Y., Wei, H., Zheng, X., Yu, Z., Shao, Y., Shield, J. E. & Huang, J. Strained hybrid perovskite thin films and their impact on the intrinsic stability of perovskite solar cells. *Science Advances* **3**, eaao5616, (2017).

119 Zhu, C., Niu, X., Fu, Y., Li, N., Hu, C., Chen, Y., He, X., Na, G., Liu, P., Zai, H., Ge, Y., Lu, Y., Ke, X., Bai, Y., Yang, S., Chen, P., Li, Y., Sui, M., Zhang, L., Zhou, H. & Chen, Q. Strain engineering in perovskite solar cells and its impacts on carrier dynamics. *Nature Communications* **10**, 815, (2019).

120 Steele, J. A., Jin, H., Dovgaliuk, I., Berger, R. F., Braeckevelt, T., Yuan, H., Martin, C., Solano, E., Lejaeghere, K., Rogge, S. M. J., Notebaert, C., Vandezande, W., Janssen, K. P. F., Goderis, B., Debroye, E., Wang, Y. K., Dong, Y., Ma, D., Saidaminov, M., Tan, H., Lu, Z., Dyadkin, V., Chernyshov, D., Van Speybroeck, V., Sargent, E. H., Hofkens, J. & Roeffaers, M. B. J. Thermal unequilibrium of strained black CsPbI3 thin films. *Science* **365**, eaax3878, (2019).

121 Lü, X., Wang, Y., Stoumpos, C. C., Hu, Q., Guo, X., Chen, H., Yang, L., Smith, J. S., Yang, W. & Zhao, Y. Enhanced Structural Stability and Photo Responsiveness of CH3NH3SnI3 Perovskite via Pressure-Induced Amorphization and Recrystallization. *Advanced Materials* **28**, 8663-8668, (2016).

122 Liu, G., Kong, L., Gong, J., Yang, W., Mao, H. k., Hu, Q., Liu, Z., Schaller, R. D., Zhang, D. & Xu, T. Pressure-Induced Bandgap Optimization in Lead-Based Perovskites with Prolonged Carrier Lifetime and Ambient Retainability. *Advanced Functional Materials* **27**, (2017).

123 Liu, S., Sun, S., Gan, C. K., del Águila, A. G., Fang, Y., Xing, J., Do, T. T. H., White, T. J., Li, H., Huang, W. & Xiong, Q. Manipulating efficient light emission in two-dimensional perovskite crystals by pressure-induced anisotropic deformation. *Science Advances* **5**, eaav9445, (2019).

124 Ma, Z., Liu, Z., Lu, S., Wang, L., Feng, X., Yang, D., Wang, K., Xiao, G., Zhang, L., Redfern, S. A. T. & Zou, B. Pressure-induced emission of cesium lead halide perovskite nanocrystals. *Nature Communications* **9**, 4506, (2018).

125 Jaffe, A., Lin, Y., Mao, W. L. & Karunadasa, H. I. Pressure-induced metallization of the halide perovskite (CH3NH3) PbI3. *Journal of the American Chemical Society* **139**, 4330-4333, (2017).

126 Han, Q., Bae, S.-H., Sun, P., Hsieh, Y.-T., Yang, Y., Rim, Y. S., Zhao, H., Chen, Q., Shi, W., Li, G. & Yang, Y. Single Crystal Formamidinium Lead Iodide (FAPbI3): Insight into the Structural, Optical, and Electrical Properties. *Advanced Materials* **28**, 2253-2258, (2016).

127 Fang, Y., Dong, Q., Shao, Y., Yuan, Y. & Huang, J. Highly narrowband perovskite single-crystal photodetectors enabled by surface-charge recombination. *Nature Photonics* **9**, 679, (2015).

128 Wang, W. F., Su, J., Zhang, L., Lei, Y., Wang, D., Lu, D. & Bai, Y. Growth of mixed-halide perovskite single crystals. *CrystEngComm* **20**, 1635-1643, (2018).

129 Chen, T., Foley, B. J., Park, C., Brown, C. M., Harriger, L. W., Lee, J., Ruff, J., Yoon, M., Choi, J. J. & Lee, S.-H. Entropy-driven structural transition and kinetic trapping in formamidinium lead iodide perovskite. *Science Advances* **2**, e1601650, (2016).

130 Maculan, G., Sheikh, A. D., Abdelhady, A. L., Saidaminov, M. I., Haque, M. A., Murali, B., Alarousu, E., Mohammed, O. F., Wu, T. & Bakr, O. M. CH3NH3PbCl3 Single Crystals: Inverse Temperature Crystallization and Visible-Blind UV-Photodetector. *The journal of physical chemistry letters* **6**, 3781-3786, (2015).

131 Pohl, U. W. *Epitaxy of Semiconductors: Introduction to Physical Principles*. (Springer Science & Business Media, 2013).

132 Steele, J. A., Yuan, H., Tan, C. Y. X., Keshavarz, M., Steuwe, C., Roeffaers, M. B. J. & Hofkens, J. Direct Laser Writing of δ- to α-Phase Transformation in Formamidinium Lead Iodide. *ACS nano* **11**, 8072-8083, (2017).

133 Quarti, C., Grancini, G., Mosconi, E., Bruno, P., Ball, J. M., Lee, M. M., Snaith, H. J., Petrozza, A. & Angelis, F. D. The Raman spectrum of the CH3NH3PbI3 hybrid perovskite: interplay of theory and experiment. *The journal of physical chemistry letters* **5**, 279-284, (2013).

134 Pérez-Osorio, M. A., Lin, Q., Phillips, R. T., Milot, R. L., Herz, L. M., Johnston, M. B. & Giustino, F. Raman Spectrum of the Organic–Inorganic Halide Perovskite CH3NH3PbI3 from First Principles and High-Resolution Low-Temperature Raman Measurements. *The Journal of Physical Chemistry C* **122**, 21703-21717, (2018).

135 Pering, S. R., Deng, W., Troughton, J. R., Kubiak, P. S., Ghosh, D., Niemann, R. G., Brivio, F., Jeffrey, F. E., Walker, A. B., Islam, M. S., Watson, T. M., Raithby, P. R., Johnson, A. L., Lewis, S. E. & Cameron, P. J. Azetidinium lead iodide for perovskite solar cells. *Journal of Materials Chemistry A* **5**, 20658-20665, (2017).

136 Steele, J. A., Yuan, H., Tan, C. Y., Keshavarz, M., Steuwe, C., Roeffaers, M. B. & Hofkens, J. Direct Laser Writing of δ-to α-Phase Transformation in Formamidinium Lead Iodide. *ACS nano*, (2017).

137 Niemann, R. G., Kontos, A. G., Palles, D., Kamitsos, E. I., Kaltzoglou, A., Brivio, F., Falaras, P. & Cameron, P. J. Halogen Effects on Ordering and Bonding of CH3NH3+ in CH3NH3PbX3 (X = Cl, Br, I) Hybrid Perovskites: A Vibrational Spectroscopic Study. *The Journal of Physical Chemistry C* **120**, 2509-2519, (2016).

138 Taylor, V. C. A., Tiwari, D., Duchi, M., Donaldson, P. M., Clark, I. P., Fermin, D. J. & Oliver, T. A. A. Investigating the Role of the Organic Cation in Formamidinium Lead Iodide Perovskite Using Ultrafast Spectroscopy. *The journal of physical chemistry letters* **9**, 895-901, (2018).

139 Govinda, S., Kore, B. P., Swain, D., Hossain, A., De, C., Guru Row, T. N. & Sarma, D. D. Critical Comparison of FAPbX3 and MAPbX3 (X = Br and Cl): How Do They Differ? *The Journal of Physical Chemistry C* **122**, 13758-13766, (2018).

140 Nakada, K., Matsumoto, Y., Shimoi, Y., Yamada, K. & Furukawa, Y. Temperature-Dependent Evolution of Raman Spectra of Methylammonium Lead Halide Perovskites, CH3NH3PbX3 (X = I, Br). *Molecules* **24**, 626, (2019).

141 Frank, O., Mohr, M., Maultzsch, J., Thomsen, C., Riaz, I., Jalil, R., Novoselov, K. S., Tsoukleri, G., Parthenios, J., Papagelis, K., Kavan, L. & Galiotis, C. Raman 2D-Band Splitting in Graphene: Theory and Experiment. *ACS nano* **5**, 2231-2239, (2011).

142 Chen, J., Conache, G., Pistol, M.-E., Gray, S. M., Borgström, M. T., Xu, H., Xu, H. Q., Samuelson, L. & Håkanson, U. Probing Strain in Bent Semiconductor Nanowires with Raman Spectroscopy. *Nano Letters* **10**, 1280-1286, (2010).

143 Mohiuddin, T. M. G., Lombardo, A., Nair, R. R., Bonetti, A., Savini, G., Jalil, R., Bonini, N., Basko, D. M., Galiotis, C., Marzari, N., Novoselov, K. S., Geim, A. K. & Ferrari, A. C. Uniaxial strain in graphene by Raman spectroscopy:Gpeak splitting, Grüneisen parameters, and sample orientation. *Physical Review B* **79**, 205433, (2009).

144 Ledinský, M., Löper, P., Niesen, B., Holovský, J., Moon, S.-J., Yum, J.-H., De Wolf, S., Fejfar, A. & Ballif, C. Raman Spectroscopy of Organic–Inorganic Halide Perovskites. *The journal of physical chemistry letters* **6**, 401-406, (2015).

145 Li, D., Wang, G., Cheng, H.-C., Chen, C.-Y., Wu, H., Liu, Y., Huang, Y. & Duan, X. Size-dependent phase transition in methylammonium lead iodide perovskite microplate crystals. *Nature Communications* **7**, 11330, (2016).

146 Sarmah, S. P., Burlakov, V. M., Yengel, E., Murali, B., Alarousu, E., El-Zohry, A. M., Yang, C., Alias, M. S., Zhumekenov, A. A., Saidaminov, M. I., Cho, N., Wehbe, N., Mitra, S., Ajia, I., Dey, S., Mansour, A. E., Abdelsamie, M., Amassian, A., Roqan, I. S., Ooi, B. S., Goriely, A., Bakr, O. M. & Mohammed, O. F. Double Charged Surface Layers in Lead Halide Perovskite Crystals. *Nano Letters* **17**, 2021-2027, (2017).

147 Kanemitsu, Y. Luminescence spectroscopy of lead-halide perovskites: materials properties and application as photovoltaic devices. *Journal of Materials Chemistry C* **5**, 3427-3437, (2017).

148 Xie, L.-Q., Chen, L., Nan, Z.-A., Lin, H.-X., Wang, T., Zhan, D.-P., Yan, J.-W., Mao, B.-W. & Tian, Z.-Q. Understanding the Cubic Phase Stabilization and Crystallization Kinetics in Mixed Cations and Halides Perovskite Single Crystals. *Journal of the American Chemical Society* **139**, 3320-3323, (2017).

149 Wenger, B., Nayak, P. K., Wen, X., Kesava, S. V., Noel, N. K. & Snaith, H. J. Consolidation of the optoelectronic properties of CH3NH3PbBr3 perovskite single crystals. *Nature Communications* **8**, 590, (2017).

150 Gershon, T., Shin, B., Gokmen, T., Lu, S., Bojarczuk, N. & Guha, S. Relationship between Cu2ZnSnS4 quasi donor-acceptor pair density and solar cell efficiency. *Applied Physics Letters* **103**, 193903, (2013).

151 Nayak, P., Sendner, M., Wenger, B., Wang, Z., Sharma, K., Ramadan, A. J., Lovrincic, R., Pucci, A., Madhu, P. K. & Snaith, H. J. The impact of Bi3+ heterovalent doping in organic-inorganic metal halide perovskite crystals. *Journal of the American Chemical Society*, (2017).

152 Kresse, G. & Furthmüller, J. Efficient iterative schemes for ab initio total-energy calculations using a plane-wave basis set. *Physical Review B* **54**, 11169-11186, (1996).

153 Blöchl, P. E. Projector augmented-wave method. *Physical Review B* **50**, 17953-17979, (1994).

154 Perdew, J. P., Burke, K. & Ernzerhof, M. Generalized Gradient Approximation Made Simple. *Physical Review Letters* **77**, 3865-3868, (1996).

155 Jiang, S., Luan, Y., Jang, J. I., Baikie, T., Huang, X., Li, R., Saouma, F. O., Wang, Z., White, T. J. & Fang, J. Phase Transitions of Formamidinium Lead Iodide Perovskite under Pressure. *Journal of the American Chemical Society* **140**, 13952-13957, (2018).

156 Chen, Z., Wang, Y., Sun, X., Xiang, Y., Hu, Y., Jiang, J., Feng, J., Sun, Y.-Y., Wang, X., Wang, G.-C., Lu, T.-M., Gao, H., Wertz, E. A. & Shi, J. Remote Phononic Effects in Epitaxial Ruddlesden–Popper Halide Perovskites. *The journal of physical chemistry letters* **9**, 6676-6682, (2018).

157 Ge, C., Hu, M., Wu, P., Tan, Q., Chen, Z., Wang, Y., Shi, J. & Feng, J. Ultralow Thermal Conductivity and Ultrahigh Thermal Expansion of Single-Crystal Organic–Inorganic Hybrid Perovskite CH3NH3PbX3 (X = Cl, Br, I). *The Journal of Physical Chemistry C* **122**, 15973-15978, (2018).

158 Yin, W.-J., Yang, J.-H., Kang, J., Yan, Y. & Wei, S.-H. Halide perovskite materials for solar cells: a theoretical review. *Journal of Materials Chemistry A* **3**, 8926-8942, (2015).

159 Giorgi, G., Fujisawa, J.-I., Segawa, H. & Yamashita, K. Small Photocarrier Effective Masses Featuring Ambipolar Transport in Methylammonium Lead Iodide Perovskite: A Density Functional Analysis. *The journal of physical chemistry letters* **4**, 4213-4216, (2013).

160 Wang, C., Ecker, B. R., Wei, H., Huang, J. & Gao, Y. Environmental Surface Stability of the MAPbBr3 Single Crystal. *The Journal of Physical Chemistry C* **122**, 3513-3522, (2018).

161 Comin, R., Walters, G., Thibau, E. S., Voznyy, O., Lu, Z.-H. & Sargent, E. H. Structural, optical, and electronic studies of wide-bandgap lead halide perovskites. *Journal of Materials Chemistry C* **3**, 8839-8843, (2015).

162 Shi, D., Adinolfi, V., Comin, R., Yuan, M., Alarousu, E., Buin, A., Chen, Y., Hoogland, S., Rothenberger, A. & Katsiev, K. Low trap-state density and long carrier diffusion in organolead trihalide perovskite single crystals. *Science* **347**, 519-522, (2015).

163 Pospisil, J., Zmeskal, O., Nespurek, S., Krajcovic, J., Weiter, M. & Kovalenko, A. Density of bulk trap states of hybrid lead halide perovskite single crystals: temperature modulated space-charge-limited-currents. *Scientific Reports* **9**, 3332, (2019).

164 Saidaminov, M. I., Abdelhady, A. L., Murali, B., Alarousu, E., Burlakov, V. M., Peng, W., Dursun, I., Wang, L., He, Y. & Maculan, G. High-quality bulk hybrid perovskite single crystals within minutes by inverse temperature crystallization. *Nature Communications* **6**, (2015).

165 Wu, Z., Yao, W., London, A. E., Azoulay, J. D. & Ng, T. N. Elucidating the Detectivity Limits in Shortwave Infrared Organic Photodiodes. *Advanced Functional Materials* **28**, 1800391, (2018).

166 Stolterfoht, M., Armin, A., Philippa, B. & Neher, D. The Role of Space Charge Effects on the Competition between Recombination and Extraction in Solar Cells with Low-Mobility Photoactive Layers. *The journal of physical chemistry letters* **7**, 4716-4721, (2016).

167 Mihailetchi, V. D., Xie, H. X., de Boer, B., Koster, L. J. A. & Blom, P. W. M. Charge Transport and Photocurrent Generation in Poly(3-hexylthiophene): Methanofullerene Bulk-Heterojunction Solar Cells. *Advanced Functional Materials* **16**, 699-708, (2006).

168 Chen, B., Yang, M., Priya, S. & Zhu, K. Origin of J–V Hysteresis in Perovskite Solar Cells. *The journal of physical chemistry letters* **7**, 905-917, (2016).

169 Wei, J., Zhao, Y., Li, H., Li, G., Pan, J., Xu, D., Zhao, Q. & Yu, D. Hysteresis Analysis Based on the Ferroelectric Effect in Hybrid Perovskite Solar Cells. *The journal of physical chemistry letters* **5**, 3937-3945, (2014).

170 Tress, W., Marinova, N., Moehl, T., Zakeeruddin, S. M., Nazeeruddin, M. K. & Grätzel, M. Understanding the rate-dependent J–V hysteresis, slow time component, and aging in CH3NH3PbI3 perovskite solar cells: the role of a compensated electric field. *Energy & Environmental Science* **8**, 995-1004, (2015).

171 Bain, A. K. & Chand, P. *Ferroelectrics: Principles and Applications*. (John Wiley & Sons, 2017).

172 Li, C., Guerrero, A., Huettner, S. & Bisquert, J. Unravelling the role of vacancies in lead halide perovskite through electrical switching of photoluminescence. *Nature Communications* **9**, 5113, (2018).

173 Li, C., Guerrero, A., Zhong, Y., Gräser, A., Luna, C. A. M., Köhler, J., Bisquert, J., Hildner, R. & Huettner, S. Real-Time Observation of Iodide Ion Migration in Methylammonium Lead Halide Perovskites. *Small* **13**, 1701711, (2017).

174 Lee, J.-W., Kim, S.-G., Yang, J.-M., Yang, Y. & Park, N.-G. Verification and mitigation of ion migration in perovskite solar cells. *APL materials* **7**, 041111, (2019).

175 Yun, J. S., Seidel, J., Kim, J., Soufiani, A. M., Huang, S., Lau, J., Jeon, N. J., Seok, S. I., Green, M. A. & Ho-Baillie, A. Critical Role of Grain Boundaries for Ion Migration in Formamidinium and Methylammonium Lead Halide Perovskite Solar Cells. *Advanced Energy Materials* **6**, 1600330, (2016).

176 Mićić, O. I., Cheong, H. M., Fu, H., Zunger, A., Sprague, J. R., Mascarenhas, A. & Nozik, A. J. Size-Dependent Spectroscopy of InP Quantum Dots. *The Journal of Physical Chemistry B* **101**, 4904-4912, (1997).

177 Wehrenfennig, C., Liu, M., Snaith, H. J., Johnston, M. B. & Herz, L. M. Homogeneous Emission Line Broadening in the Organo Lead Halide Perovskite CH3NH3PbI3–xClx. *The journal of physical chemistry letters* **5**, 1300-1306, (2014).

178 Yan, Z.-Z., Jiang, Z.-H., Lu, J.-P. & Ni, Z.-H. Interfacial charge transfer in WS2 monolayer/CsPbBr3 microplate heterostructure. *Frontiers of Physics* **13**, 138115, (2018).

179 Zi-Yu, P., Jian-Long, X., Jing-Yue, Z., Xu, G. & Sui-Dong, W. Solution-Processed High-Performance Hybrid Photodetectors Enhanced by Perovskite/MoS2 Bulk Heterojunction. *Advanced Materials Interfaces* **0**, 1800505, (2018).

180 Li, H., Zheng, X., Liu, Y., Zhang, Z. & Jiang, T. Ultrafast interfacial energy transfer and interlayer excitons in the monolayer WS2/CsPbBr3 quantum dot heterostructure. *Nanoscale* **10**, 1650-1659, (2018).

181 Zhu, H., Wang, J., Gong, Z., Kim, Y. D., Hone, J. & Zhu, X. Y. Interfacial Charge Transfer Circumventing Momentum Mismatch at Two-Dimensional van der Waals Heterojunctions. *Nano Letters* **17**, 3591-3598, (2017).

182 Rigosi, A. F., Hill, H. M., Li, Y., Chernikov, A. & Heinz, T. F. Probing Interlayer Interactions in Transition Metal Dichalcogenide Heterostructures by Optical Spectroscopy: MoS2/WS2 and MoSe2/WSe2. *Nano Letters* **15**, 5033-5038, (2015).

183 Rudin, S., Reinecke, T. L. & Segall, B. Temperature-dependent exciton linewidths in semiconductors. *Physical Review B* **42**, 11218-11231, (1990).

184 Wright, A. D., Verdi, C., Milot, R. L., Eperon, G. E., Pérez-Osorio, M. A., Snaith, H. J., Giustino, F., Johnston, M. B. & Herz, L. M. Electron–phonon coupling in hybrid lead halide perovskites. *Nature Communications* **7**, 11755, (2016).

185 Lee, J., Koteles, E. S. & Vassell, M. O. Luminescence linewidths of excitons in GaAs quantum wells below 150 K. *Physical Review B* **33**, 5512-5516, (1986).

186 Dar, M. I., Jacopin, G., Meloni, S., Mattoni, A., Arora, N., Boziki, A., Zakeeruddin, S. M., Rothlisberger, U. & Grätzel, M. Origin of unusual bandgap shift and dual emission in organic-inorganic lead halide perovskites. *Science Advances* **2**, (2016).

187 Ni, L., Huynh, U., Cheminal, A., Thomas, T. H., Shivanna, R., Hinrichsen, T. F., Ahmad, S., Sadhanala, A. & Rao, A. Real-Time Observation of Exciton–Phonon Coupling Dynamics in Self-Assembled Hybrid Perovskite Quantum Wells. *ACS nano* **11**, 10834-10843, (2017).

188 Thirumal, K., Chong, W. K., Xie, W., Ganguly, R., Muduli, S. K., Sherburne, M., Asta, M., Mhaisalkar, S., Sum, T. C., Soo, H. S. & Mathews, N. Morphology-Independent Stable White-Light Emission from Self-Assembled Two-Dimensional Perovskites Driven by Strong Exciton–Phonon Coupling to the Organic Framework. *Chemistry of Materials* **29**, 3947-3953, (2017).

189 Hu, Y., Zhang, S., Miao, X., Su, L., Bai, F., Qiu, T., Liu, J. & Yuan, G. Ultrathin Cs3Bi2I9 Nanosheets as an Electronic Memory Material for Flexible Memristors. *Advanced Materials Interfaces* **4**, (2017).

190 Calado, P., Telford, A. M., Bryant, D., Li, X., Nelson, J., O'Regan, B. C. & Barnes, P. R. F. Evidence for ion migration in hybrid perovskite solar cells with minimal hysteresis. *Nature Communications* **7**, 13831, (2016).

191 Zimmermann, E., Wong, K. K., Müller, M., Hu, H., Ehrenreich, P., Kohlstädt, M., Würfel, U., Mastroianni, S., Mathiazhagan, G., Hinsch, A., Gujar, T. P., Thelakkat, M., Pfadler, T. & Schmidt-Mende, L. Characterization of perovskite solar cells: Towards a reliable measurement protocol. *APL materials* **4**, 091901, (2016).

192 Ayers, J. E., Kujofsa, T., Rago, P. & Raphael, J. *Heteroepitaxy of semiconductors: theory, growth, and characterization*. (CRC press, 2016).

193 Ball, J. M. & Petrozza, A. Defects in perovskite-halides and their effects in solar cells. *Nature Energy* **1**, 16149, (2016).

194 Liu, Z., Qiu, L., Juarez-Perez, E. J., Hawash, Z., Kim, T., Jiang, Y., Wu, Z., Raga, S. R., Ono, L. K., Liu, S. & Qi, Y. Gas-solid reaction based over one-micrometer thick stable perovskite films for efficient solar cells and modules. *Nature Communications* **9**, 3880, (2018).

195 Wang, K.-L., Wang, R., Wang, Z.-K., Li, M., Zhang, Y., Ma, H., Liao, L.-S. & Yang, Y. Tailored Phase Transformation of CsPbI2Br Films by Copper(II) Bromide for High-Performance All-Inorganic Perovskite Solar Cells. *Nano Letters* **19**, 5176-5184, (2019).

196 Wang, L., Zhou, H., Hu, J., Huang, B., Sun, M., Dong, B., Zheng, G., Huang, Y., Chen, Y., Li, L., Xu, Z., Li, N., Liu, Z., Chen, Q., Sun, L. D. & Yan, C. H. A Eu(3+)-Eu(2+) ion redox shuttle imparts operational durability to Pb-I perovskite solar cells. *Science* **363**, 265-270, (2019).

197 Zhao, Y., Tan, H., Yuan, H., Yang, Z., Fan, J. Z., Kim, J., Voznyy, O., Gong, X., Quan, L. N., Tan, C. S., Hofkens, J., Yu, D., Zhao, Q. & Sargent, E. H. Perovskite seeding growth of formamidinium-lead-iodide-based perovskites for efficient and stable solar cells. *Nature Communications* **9**, 1607, (2018).

198 Yang, D., Yang, R., Wang, K., Wu, C., Zhu, X., Feng, J., Ren, X., Fang, G., Priya, S. & Liu, S. High efficiency planar-type perovskite solar cells with negligible hysteresis using EDTA-complexed SnO2. *Nature Communications* **9**, 3239, (2018).

199 Wu, W.-Q., Yang, Z., Rudd, P. N., Shao, Y., Dai, X., Wei, H., Zhao, J., Fang, Y., Wang, Q., Liu, Y., Deng, Y., Xiao, X., Feng, Y. & Huang, J. Bilateral alkylamine for suppressing charge recombination and improving stability in blade-coated perovskite solar cells. *Science Advances* **5**, eaav8925, (2019).

200 Feng, J., Gong, C., Gao, H., Wen, W., Gong, Y., Jiang, X., Zhang, B., Wu, Y., Wu, Y., Fu, H., Jiang, L. & Zhang, X. Single-crystalline layered metal-halide perovskite nanowires for ultrasensitive photodetectors. *Nature Electronics* **1**, 404-410, (2018).

201 Kong, W., Li, W., Liu, C., Liu, H., Miao, J., Wang, W., Chen, S., Hu, M., Li, D., Amini, A., Yang, S., Wang, J., Xu, B. & Cheng, C. Organic Monomolecular Layers Enable Energy-Level Matching for Efficient Hole Transporting Layer Free Inverted Perovskite Solar Cells. *ACS nano* **13**, 1625-1634, (2019).

202 Liu, X., Cheng, Y., Liu, C., Zhang, T., Zhang, N., Zhang, S., Chen, J., Xu, Q., Ouyang, J. & Gong, H. 20.7% highly reproducible inverted planar perovskite solar cells with enhanced fill factor and eliminated hysteresis. *Energy & Environmental Science* **12**, 1622-1633, (2019).

203 Leijtens, T., Eperon, G. E., Barker, A. J., Grancini, G., Zhang, W., Ball, J. M., Kandada, A. R. S., Snaith, H. J. & Petrozza, A. Carrier trapping and recombination: the role of defect physics in enhancing the open circuit voltage of metal halide perovskite solar cells. *Energy & Environmental Science* **9**, 3472-3481, (2016).

204 Brenes, R., Guo, D., Osherov, A., Noel, N. K., Eames, C., Hutter, E. M., Pathak, S. K., Niroui, F., Friend, R. H., Islam, M. S., Snaith, H. J., Bulović, V., Savenije, T. J. & Stranks, S. D. Metal Halide Perovskite Polycrystalline Films Exhibiting Properties of Single Crystals. *Joule* **1**, 155-167, (2017).

205 Yao, W., Wu, Z., Huang, E., Huang, L., London, A. E., Liu, Z., Azoulay, J. D. & Ng, T. N. Organic Bulk Heterojunction Infrared Photodiodes for Imaging Out to 1300 nm. *ACS Applied Electronic Materials* **1**, 660-666, (2019).

206 Street, R. A., Yang, Y., Thompson, B. C. & McCulloch, I. Capacitance Spectroscopy of Light Induced Trap States in Organic Solar Cells. *The Journal of Physical Chemistry C* **120**, 22169-22178, (2016).

207 Hwang, T., Yun, A. J., Kim, J., Cho, D., Kim, S., Hong, S. & Park, B. Electronic Traps and Their Correlations to Perovskite Solar Cell Performance via Compositional and Thermal Annealing Controls. *ACS Applied Materials & Interfaces* **11**, 6907-6917, (2019).

208 Kovalenko, A., Pospisil, J., Zmeskal, O., Krajcovic, J. & Weiter, M. Ionic origin of a negative capacitance in lead halide perovskites. *physica status solidi (RRL) – Rapid Research Letters* **11**, 1600418, (2017).

209 Khan, M. T., Salado, M., Almohammedi, A., Kazim, S. & Ahmad, S. Elucidating the Impact of Charge Selective Contact in Halide Perovskite through Impedance Spectroscopy. *Advanced Materials Interfaces* **0**, 1901193, (2019).

210 Han, C., Wang, K., Zhu, X., Yu, H., Sun, X., Yang, Q. & Hu, B. Unraveling surface and bulk trap states in lead halide perovskite solar cells using impedance spectroscopy. *Journal of Physics D: Applied Physics* **51**, 095501, (2018).

211 Samiee, M., Konduri, S., Ganapathy, B., Kottokkaran, R., Abbas, H. A., Kitahara, A., Joshi, P., Zhang, L., Noack, M. & Dalal, V. Defect density and dielectric constant in perovskite solar cells. *Applied Physics Letters* **105**, 153502, (2014).

212 Ferreira, A. C., Létoublon, A., Paofai, S., Raymond, S., Ecolivet, C., Rufflé, B., Cordier, S., Katan, C., Saidaminov, M. I., Zhumekenov, A. A., Bakr, O. M., Even, J. & Bourges, P. Elastic Softness of Hybrid Lead Halide Perovskites. *Physical Review Letters* **121**, 085502, (2018).

213 Zienkiewicz, O. C., Taylor, R. L., Nithiarasu, P. & Zhu, J. *The finite element method*. Vol. 3 (McGraw-hill London, 1977).

214 Katan, C., Mohite, A. D. & Even, J. Entropy in halide perovskites. *Nature Materials* **17**, 377, (2018).

215 Matthews, J. W. & Blakeslee, A. E. Defects in epitaxial multilayers: I. Misfit dislocations. *Journal of crystal growth* **27**, 118-125, (1974).

216 People, R. & Bean, J. C. Calculation of critical layer thickness versus lattice mismatch for GexSi1−x/Si strained-layer heterostructures. *Applied Physics Letters* **47**, 322-324, (1985).

217 Kosyachenko, L. A. *Solar Cells: New Aspects and Solutions*. (BoD–Books on Demand, 2011).

218 Saidaminov, M. I., Abdelhady, A. L., Murali, B., Alarousu, E., Burlakov, V. M., Peng, W., Dursun, I., Wang, L., He, Y., Maculan, G., Goriely, A., Wu, T., Mohammed, O. F. & Bakr, O. M. High-quality bulk hybrid perovskite single crystals within minutes by inverse temperature crystallization. *Nature Communications* **6**, 7586, (2015).

219 Zhao, Y., Li, C. & Shen, L. Recent advances on organic-inorganic hybrid perovskite photodetectors with fast response. *InfoMat* **0**, (2019).

220 Haihua, Z., Yishi, W., Qing, L., Zhaoyi, Z., Yanping, L., Qinggang, G., Peng, L., Meili, L., Jiannian, Y. & Hongbing, F. A Two-Dimensional Ruddlesden–Popper Perovskite Nanowire Laser Array based on Ultrafast Light-Harvesting Quantum Wells. *Angewandte Chemie International Edition* **0**, 7748-7752, (2018).

221 Ye, F., Lin, H., Wu, H., Zhu, L., Huang, Z., Ouyang, D., Niu, G. & Choy, W. C. H. High-Quality Cuboid CH3NH3PbI3 Single Crystals for High Performance X-Ray and Photon Detectors. *Advanced Functional Materials* **0**, 1806984, (2018).

222 Ji, L., Hsu, H.-Y., Lee, J., Bard, A. J. & Yu, E. T. High performance photodetectors based on solution-processed epitaxial grown hybrid halide perovskites. *Nano Letters* **18**, 994-1000, (2018).

223 Zhang, Y., Zhou, Z., Ji, F., Li, Z., Cui, G., Gao, P., Oveisi, E., Nazeeruddin, M. K. & Pang, S. Trash into Treasure: δ-FAPbI3 Polymorph Stabilized MAPbI3 Perovskite with Power Conversion Efficiency beyond 21%. *Advanced Materials* **0**, 1707143, (2018).

224 Han, Q., Bae, S. H., Sun, P., Hsieh, Y. T., Yang, Y. M., Rim, Y. S., Zhao, H., Chen, Q., Shi, W. & Li, G. Single crystal formamidinium lead iodide (FAPbI3): Insight into the structural, optical, and electrical properties. *Advanced Materials* **28**, 2253-2258, (2016).

225 Yi, C., Luo, J., Meloni, S., Boziki, A., Ashari-Astani, N., Grätzel, C., Zakeeruddin, S. M., Röthlisberger, U. & Grätzel, M. Entropic stabilization of mixed A-cation ABX 3 metal halide perovskites for high performance perovskite solar cells. *Energy & Environmental Science* **9**, 656-662, (2016).

226 Yang, W. S., Noh, J. H., Jeon, N. J., Kim, Y. C., Ryu, S., Seo, J. & Seok, S. I. High-performance photovoltaic perovskite layers fabricated through intramolecular exchange. *Science* **348**, 1234-1237, (2015).

227 Jeon, N. J., Noh, J. H., Yang, W. S., Kim, Y. C., Ryu, S., Seo, J. & Seok, S. I. Compositional engineering of perovskite materials for high-performance solar cells. *Nature* **517**, 476-480, (2015).

228 Lee, J.-W., Dai, Z., Han, T.-H., Choi, C., Chang, S.-Y., Lee, S.-J., De Marco, N., Zhao, H., Sun, P., Huang, Y. & Yang, Y. 2D perovskite stabilized phase-pure formamidinium perovskite solar cells. *Nature Communications* **9**, 3021, (2018).

229 Yuan, S., Qian, F., Yang, S., Cai, Y., Wang, Q., Sun, J., Liu, Z. & Liu, S. NbF5: A Novel α-Phase Stabilizer for FA-Based Perovskite Solar Cells with High Efficiency. *Advanced Functional Materials* **0**, 1807850, (2019).

230 Fu, Y., Wu, T., Wang, J., Zhai, J., Shearer, M. J., Zhao, Y., Hamers, R. J., Kan, E., Deng, K. & Zhu, X.-Y. Stabilization of the metastable lead iodide perovskite phase via surface functionalization. *Nano Letters* **17**, 4405-4414, (2017).

231 Gu, L., Zhang, D., Kam, M., Zhang, Q., Poddar, S., Fu, Y., Mo, X. & Fan, Z. Significantly improved black phase stability of FAPbI3 nanowires via spatially confined vapor phase growth in nanoporous templates. *Nanoscale* **10**, 15164-15172, (2018).

232 Zhou, Y., Kwun, J., Garces, H. F., Pang, S. & Padture, N. P. Observation of phase-retention behavior of the HC (NH 2) 2 PbI 3 black perovskite polymorph upon mesoporous TiO 2 scaffolds. *Chemical Communications* **52**, 7273-7275, (2016).

233 Xu, Z., Salvador, P. & Kitchin, J. R. First-Principles Investigation of the Epitaxial Stabilization of Oxide Polymorphs: TiO2 on (Sr,Ba)TiO3. *ACS Applied Materials & Interfaces* **9**, 4106-4118, (2017).

234 Liu, B., Long, M. Q., Cai, M. Q., Hao, X. T. & Yang, J. L. Ferroelectric Polarization in CsPbI3/CsSnI3 Perovskite Heterostructure. *Journal of Physical Chemistry C* **122**, 17820-17824, (2018).

235 Li, B., Zhang, Y., Fu, L., Yu, T., Zhou, S., Zhang, L. & Yin, L. Surface passivation engineering strategy to fully-inorganic cubic CsPbI3 perovskites for high-performance solar cells. *Nat Commun* **9**, 1076, (2018).

236 Ma, S., Kim, S. H., Jeong, B., Kwon, H.-C., Yun, S.-C., Jang, G., Yang, H., Park, C., Lee, D. & Moon, J. Strain-Mediated Phase Stabilization: A New Strategy for Ultrastable α-CsPbI3 Perovskite by Nanoconfined Growth. *Small* **0**, 1900219, (2019).

237 Liu, M., Chen, Y., Tan, C. S., Quintero-Bermudez, R., Proppe, A. H., Munir, R., Tan, H., Voznyy, O., Scheffel, B., Walters, G., Kam, A. P. T., Sun, B., Choi, M. J., Hoogland, S., Amassian, A., Kelley, S. O., Garcia de Arquer, F. P. & Sargent, E. H. Lattice anchoring stabilizes solution-processed semiconductors. *Nature* **570**, 96-101, (2019).

238 Lee, J. H., Murugavel, P., Ryu, H., Lee, D., Jo, J. Y., Kim, J. W., Kim, H. J., Kim, K. H., Jo, Y., Jung, M. H., Oh, Y. H., Kim, Y. W., Yoon, J. G., Chung, J. S. & Noh, T. W. Epitaxial Stabilization of a New Multiferroic Hexagonal Phase of TbMnO3 Thin Films. *Advanced Materials* **18**, 3125-3129, (2006).

239 Vailionis, A., Siemons, W. & Koster, G. Room temperature epitaxial stabilization of a tetragonal phase in ARuO3 (A=Ca and Sr) thin films. *Applied Physics Letters* **93**, 051909, (2008).

240 Li, Y. & Yang, K. High-throughput computational design of organic–inorganic hybrid halide semiconductors beyond perovskites for optoelectronics. *Energy & Environmental Science* **12**, 2233-2243, (2019).